UTPP-32

A STUDY OF HADRONIC JET PRODUCTION IN PROTON-ANTIPROTON COLLISION AT $\sqrt{s}$=1800GEV

JUNE 1988

AKIHIRO YAMASHITA

Submitted in partial Fulfillment of the requirements
for the degree of Doctor of Science
in Doctoral program in
University of Tsukuba

UTPP–32

A STUDY OF HADRONIC JET PRODUCTION IN PROTON-ANTIPROTON COLLISION AT $\sqrt{s}$=1800GEV

JUNE 1988

AKIHIRO YAMASHITA

Submitted in partial Fulfillment of the requirements
for the degree of Doctor of Science
in Doctoral program in
University of Tsukuba

Abstract

An experimental result of the hadronic jet production in proton and antiproton collision at the center-of-mass energy ($\sqrt{s}$) of 1.8TeV is described. The jet inclusive cross section in the pseudorapidity range of $0.1<|\eta|<0.7$ is the main feature of this article.

The Tevatron collider at Fermi National Accelerator Laboratory, U.S.A., provided proton and antiproton collision at $\sqrt{s}=1.8$TeV with total integrated luminosity of $74nb^{-1}$ during the period of January through May 1987. With the CDF detector built for the experiment data were taken for an integrated luminosity of $34nb^{-1}$. The data of the integrated luminosity $24.5nb^{-1}$ were analyzed for the inclusive jet cross section.

The analysis of jet is based on the fine segmented calorimetry of the detector. The combined electromagnetic and hadronic calorimetry has approximately uniform granularity in pseudorapidity and azimuth angle. The central electromagnetic and hadron calorimeters which cover the range of pseudorapidity range $0<|\eta|<1.0$ were used for the analysis. The design, construction, test, calibration and monitoring of the calorimeters are described.

The calorimeters were tested and calibrated by cosmic rays, by high energy beam of electrons and pions and by particles produced in the actual proton-antiproton collision. The energy resolution, the linearity and the complete response map were measured in the beam line. All channels of the calorimeters were calibrated by 50GeV/c electrons or pions. The calibration constants taken in the beam line were used in the actual collision run combined with the readout of various monitoring devices. The reproducibility of the calibration was found to be 0.6% for the central electromagnetic, 1.0% for the central hadron calorimeter.

Clear shapes of clusters were observed in the η–ϕ plane of the fine segmented calorimeter in events of proton-antiproton collision. The transverse momentum Pt of the scattered parton is modified in observation by the effect of cracks between calorimeter modules, by the non-linearity of the calorimeter response for low momentum particles and by

the algorithm of cluster finding. The relation between the Pt of the observed cluster and the Pt of the scattered partons were established by use of Monte-carlo event generator inspired by the Quantum Chromo Dynamics (QCD) and the detector simulator based on the beam test. This relation was examined using the π^0/γ + jet events experimentally. The geometrical acceptance of the detector and the efficiency of the trigger system were also studied with the Monte-carlo simulation.

We accepted jets whose Pt are greater than 50GeV/c and compared their inclusive cross section with theoretical calculations by QCD. They are consistent within the systematic error. Comparison of the scaled invariant cross section of jet production with the results obtained in the low energy region shows a clear Q^2 dependence.

Acknowledgement

I would like to express my appreciation to Professor Kunitaka Kondo, who has been my advisor since I began research. His advice and guidance have been a great help to me throughout the course of this research.

Professors Koji Takikawa and Shigeyuki Miyashita are appreciated for their continuous encouragement and criticism.

My special thanks are to Professor Shoji Mikamo, Drs. Kiyoshi Yasuoka, Teruki Kamon and Miss Yukiko Kikuchi for cooperation in constructing, data taking and analysis of the central electromagnetic calorimeter.

I am grateful to Drs. Lawrence Nodulman, David Underwood, Robert Wagner and Robert Diebold for their effort of constructing and testing the central electromagnetic calorimeter.

Drs. Akira Murakami and Angela DiVirgilio are appreciated for the cosmic ray test.

I would like to thank the CDF wedge group Drs.John Cooper, Steve Hahn, Hugh H.Williams, Robert Diebold, Lawrence Nodulman, James Proudfoot, Paul Schoessow, David Underwood, Robert Wagner, A. Barry Wicklund, Keith Chadwick, Jimmy Simmons, Selchek Cihangir, Hans Jensen, Kiyoshi Yasuoka, Sergio Bertolucci,Maria Curatolo, B.Esposito, Andrea Sansoni, Versil Barnes, Art Garfinkel, Alvin Lassanen Hans Jensen Messers Marshal Miller, Steve Kuhlman, David Smith and Tom Westhusing for their cooperation in the beam line.

This experiments would have been impossible without the successful operation of the Tevatron collider by staffs. I gratefully acknowledge for their effort.

The simulation package programs for the CDF were constructed with the efforts of many people. I would like to appreciate to Drs. Yoshinobu Takaiwa, James Freeman, John Yoh and G.P.Yeh. Discussion with them made me understand many problems about the analysis.

I thank Drs. J.J.Schmidt and Marjorie Shapiro for their cooperation and suggestion in the data reduction.

I gratefully appreciate Dr.Taiji Yamanouchi for his advices.

The discussion with members of the CDF jet group was important for this analysis. I thank Dr.Jim Sieglist, Messers Steve Kuhlman , Rick St.Dennis and David Brown.

About the jet analysis, I owe much to Dr.Shinhong Kim for his advice and guidance.

Drs. Fumio Abe, Yoshio Hayashide, Messers Masayuki Shibata, Youhei Morita, Toshihiro Mimashi, Takashi Ino, Masahiko Yokoyama, Yoshiharu Seiya are appreciated for their cooperation.

The present work was carried out as a program of the Collider Detector at Fermilab (CDF) under the accord of US-Japan collaboration in high energy physics. I gratefully acknowledge the support of the U.S. Department of Energy and the Japanese Ministry of education, Science and Culture. I wish to express my special thanks to Dr. Alvin Tollestrup (CDF co-leader), Professor Roy F. Schwitters (CDF co-leader), Drs.Ken Stanfield (Head of Research division) and Leon Lederman (director) of Fermilab and Drs. Ken Kikuchi and Tetsuji Nishikawa of K.E.K.

Finally, I would like to thank my mother for her constant support. This thesis is dedicated to her.

Table of contents

Chapter1
Introduction

History of jet physics

Hadron-hadron collision at high energy has been a central subject in particle physics since early days. The transverse momentum Pt of charged particles produced in collision has been one of the key quantities to understand the nature of hadronic collision. Most particles produced in hadron-hadron collisions have relatively low transverse momentum. Averaged Pt of charged particles is, for example, <Pt> =0.35 GeV/c at $\sqrt{s}$=63GeV (Ref. [1.1]) , <Pt> = 0.432GeV/c at $\sqrt{s}$=630GeV (Ref. [1.2]) and <Pt> = 0.495GeV/c at 1800GeV (Ref. [1.3]). In 1972 , productions of very high Pt particles were first observed in proton-proton collision at the center of mass energy from 30 to 63GeV at the CERN Intersecting Storage Ring (Ref. [1.4]). The invariant cross section of a single particle (π^0) did not fall off exponentially as expected by the thermodynamic model (Ref.[1.5]), but with a form Ref.[1.6]

$$E\frac{d\sigma^3(\pi^0)}{d^3P_t} = P_t^{-(8.24\pm0.05)}\, exp\left[-(26.1\pm0.5)X_t\right],$$

where $X_t = 2P_t/\sqrt{s}$.

This behavior was interpreted in the framework of the parton model (Ref.[1.7]) as a result of elastic or quasi-elastic scattering of two point-like constituents of the incident proton (Ref.[1.8]).

Such *large Pt* phenomena were also studied in fixed target experiments at Fermilab 400GeV proton synchrotron and at CERN SPS. These measurements were expected to see the effect of hard scattering of partons, but they did not provide a definitive proof of this picture. The theory predicted the invariant cross section of scatterd particles to be

$$E\frac{d\sigma^3}{d^3P_t} = P_t^{-4} f\ (X_t\ ,\ cos\theta\ ).$$

At about the same period of time, a new non-Abelian gauge theory called Quantum Chromo-dynamics (QCD) became the standard model of the strong interactions(Ref.[1.9]). The particle jet in hadron-hadron collisions described by QCD is as follows. Large angle scattering of two high-x partons produces two partons outgoing with high-Pt's. The strong force among partons induces a final state interaction among the two high-Pt partons and other partons; this results in the production of many hadrons, a step called hadronization or fragmentation. Since this final state interaction involves mostly low momentum transfer mechanisms, the final result is the production of two highly collimated clusters of hadrons which are seen as *jets*. The four momentum of a parent parton is approximately conserved in the jet. The two jets are mostly coplaner because the incident partons have low Pt. They have a net longitudinal momentum in general, since the initial partons have different magnitudes of momentum.

In 1975, by an experiment at the SLAC electron-positron collider, SPEAR, it was found that hadrons were produced as jets of particles emanating from spin-1/2 point-like objects (Ref.[1.10]). They were interpreted as *quarks*.

Between 1973 and 1980 , many experiments were performed to find jets in hadron-hadron collisions. Following suggestions by Bjorken (Ref.[1.11]), these experiments employed calorimeters in order to trigger the events with whole energy of jets. The previous experiments had used the high Pt single particle trigger. This trigger scheme had distorted the structure of the jet. Fixed target experiments with jet trigger began at Fermilab and at CERN SPS in 1979. However, these experiments could not find a clear evidence of a high-Pt jets i.e.

two collimated clusters of hadrons produced back-to-back azimuthally as expected from the theory. They rather found events in which low Pt particles were distributed symmetrically in azimuth.

The absence of jets in hadron-hadron collisions , while clear jet structures had been found in electron-positron collisions , was interpreted as the effect of the tails of the multiple gluon Bremsstrahlung from the initial state partons (Ref.[1.12]), or as the effect of the tails of the multiplicity distributions in ordinary soft collisions (Ref.[1.13]). In either case, it was suspected that jets would never be produced in hadron-hadron collisions.

This was the status of the jet experiments before the CERN proton-antiproton collider began to operate at $\sqrt{s}$=546GeV in 1983.

The situation was dramatically changed by the results of two experiments, UA1 and UA2. They obtained a clear evidence of jets.

UA1 and UA2 identified clear evidences of hadronic jets (Ref.[1.14]) with total-absorption calorimeter of full-azimuthal coverage over wide polar angle. They detected a pattern of energy flow which indicated jets with no doubt. They measured inclusive jet cross section (Ref.[1.15]), the two jet angular distribution (Ref.[1.16]) and the three jet cross section (Ref.[1.17]). Fragmentation properties of hadronic jets have also been studied (Ref.[1.18]).

Parton-Parton Scattering

The jet production in hadronic collision is interpreted in the framework of the parton model as hard scattering among the constituents of incident hadrons. The initial state hadrons contain quarks , antiquarks and gluons , which are called partons. There are several elementary subprocesses of the parton+parton → parton +parton reaction. The lowest order

diagram in the strong interaction processes are shown in Fig.[1.1]. For each lowest order subprocess the scattering cross section can be written as

$$\frac{d\sigma}{d\cos\theta} = \frac{\pi\alpha_s^2}{2s}|M|^2,$$

where θ is the scattering angle , s is the square of the total energy in the center of mass system of two partons, α_S, the strong coupling constant, is a function of Q^2, the square of the four momentum transfer in the subprocess in QCD. In a model with five flavors, $\alpha_S(Q^2)$ is written as

$$\alpha_s^2(Q^2) = \frac{12\pi}{23\ln(Q^2/\Lambda^2)},$$

where Λ is a scale parameter. The property $\alpha_S \to 0$ for $Q^2 \to \infty$, called asymptotic freedom, allows perturbative calculations of strong processes at high Q^2.

The explicit form of $|M|^2$ is given in Table [1.1] as functions of the Mandelstam variables, s , t = - s(1-cosθ) , and u = - s(1+cosθ) (under the assumption of massless partons). These parameters are defined in the center of mass system of partons. Table[1.1] also displays numerical values of $|M|^2$ at θ=90°. One can see that gluon scattering is dominant whenever gluon density in the incident hadrons is comparable to that of the quarks.

Inclusive jet cross sections: Theory

The cross section for inclusive jet production as a function of the Pt of jet and angle of emission θ can be calculated to the leading order as a sum of convolution integrals: (Ref.[1.19])

$$\frac{d^2\sigma}{dP_t\, dcos\theta} = \frac{2\pi P_t}{sin^2\theta} \sum_{A,B} \int dx_1 dx_2 F_A(x_1, Q^2) F_B(x_2, Q^2) \delta(s+t+u) \alpha_s^2 \sum_f \frac{|M|^2_{AB\to f}}{s},$$

where F_A and F_B are structure functions describing the densities of partons A and B in the incident hadrons, and then the sum extends over all initial parton types A,B and all possible final states f.

The structure function $F(x, Q^2)$ is determined experimentally in deep inelastic lepton-nucleon scattering experiments in the lower range of Q^2. It is extrapolated to the range of the collider energy ($Q^2 \approx 10^4$ GeV^2) by solving the Altarelli-Parisi equation (Ref.[1.20]).

The main uncertainty in theory arises from Q^2 extrapolation of the structure functions. Structure functions by two groups, Duke and Owens (Ref.[1.21]). and Eichiten et al. (Ref.[1.22]), are shown in Fig.[1.2] at $Q^2 = 5$ GeV^2 and $Q^2 = 10^4$GeV^2 . They started with different parametrization of the results of deep inelastic experiments. But difference in high energy region is small especially in the region of our interest; $0.05 < x_t < 0.02$.

Another source of the theoretical uncertainty is QCD higher-order effects, such as gluon radiation from the initial and outgoing partons. An explicit calculations taking account of higher order processes dose not exist. Their effect is usually described by a multiplicative factor $K \leq 2$.

Inclusive jet cross section at $\sqrt{s}$=1800GeV

The CDF detector was built for proton and antiproton collision at $\sqrt{s}$=1800GeV. Calorimeters of the detector cover $2° < \theta < 178°$ in polar angle over full azimuth. They are fine segmented for the detection of jets. Measuring the inclusive cross section of jet production in hadron-hadron collision at such a high energy is an important subject because of the following reasons.

First, theory predicts Q^2 evolution of the structure function and α_s. Higher the center of mass energy is, the higher is the observed momentum transfer. The CDF can examine theory at the highest Q^2 region ever reached.

Next, the QCD assumes partons as point-like particles and no structure in them. If they have internal structures, inclusive jet cross section will be different from QCD prediction.

The absolute calibration and response map of the calorimeter are essential to get a reliable energy scale for jets. The relation between Pt of scattered partons and that of the observed clusters was determined with the help of QCD inspired Monte-carlo event generator and detector simulation program which is based on results of the beam tests of detectors.

In Section 2 of this paper , the properties of the detector are described. Much attention is paid for the calibration , linearity and resolution of the calorimeters. All the central calorimeter modules were tested and calibrated on the dedicated cosmic ray test stand and in the beam line.

In Section 3, data taking and analysis are described. It includes determination of relation between Pt of scattered partons and observed clusters by Monte-carlo simulation. Efficiency of the trigger system and acceptance of the detector are also investigated with the Monte-carlo simulation.

In Section 4 the result of inclusive jet cross section is described. Its systematic error and comparison with theoretical calculations are discussed. The scaled jet cross section is compared with the results of the low energy experiments and theoretical calculations.

Chapter 2
The CDF Detector

Overview

CDF detector is a general purpose detector built for proton and anti-proton collision at $\sqrt{s}$=2TeV Fermilab Tevatron (Ref.[2-1]). It is divided to forward/backward detectors and a central detector and weighs 4500 tons in total. A perspective view of the CDF detector is shown in figure [2.1]. Major components of the CDF detector are tracking detectors , calorimeters and muon chambers. A cross sectional view along the beam is shown in figure [2-2]

Protons and antiprotons collide inside the beam pipe at the center of the detector. The VTPC (Vertex Time Projection Chamber) surrounds collision point Ref.[2.2]. It determines the position of collision. CTC (Central Tracking Chamber)Ref. [2.3] measures the momentum of charged particles in the region $-1.5 < \eta < 1.5$ with strong (1.5 Tesla) magnetic field created by superconducting solenoidal magnet outside the CTC. Here, η is the pseudorapidity defined as $\eta = -\ln(\tan(\theta/2.))$. Another set of the tracking chambers called FTC are positioned in the forward/backward region.

The beam-beam counters (BBC) (Ref. [2.4]) detects particles by its scintillator counter. It makes a trigger that reports "COLLISION HAPPENED!" at first.

The energies of electromagnetic particles (electron and γ) and hadronic particles (π ,K...) are measured by calorimeters. They cover wide polar angle $2<\theta<178$ ° and a complete azimuthal angle. They are fine segmented into about 5000 "TOWERS" to measure the positions

of jets. All the CDF calorimeters are consisting of sandwiches of sensitive materials and absorbers. For different polar angle regions, we have three kinds of calorimeter i.e. central, plug and forward calorimeters. As absorber, lead is used for electromagnetic and iron is for hadron calorimeters in all regions.

The central electromagnetic (CEM) (Ref [2.5]), the central hadron (CHA) (Ref. [2.6]) and wall hadron (WHA) calorimeters cover the central region ($-1. < \eta < 1.$) . All of them are scintillator type calorimeters. The plug ($1. < \eta < 3.6$) and the forward ($3.6< \eta <4.2$) calorimeters consist of gas tube chambers.

Calorimeters are segmented with different sizes and summary of the segmentation is shown in figure [2.3] and table [2.1]. All of these calorimeters have been tested and calibrated in the beam line of Fermilab with electrons and pions. Calibration constants for energy scale have been monitored from the beam test. Monitoring devices for each calorimeters kept track through the run .

The muon chambers (Ref. [2.7]) covers central and forward region most outside of the detector. Muons created by collision or by decay of particles pass through lead and iron of calorimeter. Drift chambers of these muon counters detect their positions. One can get their momentum with solenoidal field in the central and troidal field in the forward, region.

Total number of channels from the CDF detector exceeds 60000. Local intelligent data acquisition and trigger system reduces the number of signals. It saves load for the on-line computer. Also, this system philosophy makes the number of signal cables pulled outside the detector small.

Central Calorimeter

Overview

The rapidity region $-1<\eta<1$ is covered by central calorimeters and wall calorimeters.

The central electromagnetic covers the angular region $33°<\theta<147°$ and the central hadron calorimeter covers $45°<\theta<35°$. The wall hadron calorimeter covers $30°<\theta<45°$. The central hadron and the wall hadron calorimeters have overlap in the $30°<\theta<52°$ region. In this article we call these three kinds of calorimeter as the *central calorimeter.*

The central calorimeters have a module structure. A wedge shape module covers $\Delta\phi=15°$ in azimuth and $-1<\eta<0$ or $0<\eta<1$ (40.6 ° to 90 °) in rapidity. 12 wedges are stacked together in *arch* structure. Four arches can be rolled into the central region.

A wedge has a tower geometry inside of it. One tower have approximately $\Delta\eta = 0.1$. There are 10 towers in the central electromagnetic calorimeter , 8 in the central hadron calorimeter and 6 in the endwall hadron calorimeter. Three towers of the central hadron calorimeter and the endwall hadron calorimeter overlap.

Central calorimeters employs scintillator as a sensitive material in common. Light emitted in scintillator plates is collected by wavelength shifter bars and transmitted to photomultipliers. This scheme is common at electromagnetic calorimeter of hadronic calorimeter.

The central electromagnetic calorimeter in a wedge consists of 31 layers of 5mm thick scintillator and 3mm thick lead plates. The thickness is 18 radiation lengths in total. A cross sectional view of central electromagnetic calorimeter is shown in Fig. [2.4]. The parameters are summarized in table [2.2]. A proportional wire/strip chamber which can measure precise position of electromagnetic shower is placed between 8 th layer and 9th layer. Light emitted by scintillator enters into wavelength shifter placed both side of the wedge through air gap. Green light re-emitted green light in the wavelength shifter bar travels through glue-jointed acrylic rod to the transition piece which is placed in front of a photomulitiplier.

As shown in fig [2.5] , photomultipliers are placed outside of the hadron calorimeter where the magnetic field is weak.

The central hadron calorimeter in the wedge consist of 32 layers of 2.5cm thick steel plates and 1.0 cm thick scintillator plates. It have $4.7/\sin\theta$ units of absorption length. It also

employs wavelength shifter bars. Two wavelength shifter bars lie against the long sides of the scintillator. Each shifter bar connected to s light guide of the same cross section. Light guide are combined at the azimuthal outside of the layer, and connected to transition pieces in front of photomulipliers. Photomultipliers are also placed outside of the central calorimeter. Two photomulipliers are used for one tower. There are 768 photomultipliers in total for the central hadron calorimeter. Their parameters are summarized in table [2.3].

An endwall calorimeter module has 15 layers of 5cm thick iron and 1.0cm thick acrylic scintillator plates. Total depth of a wall hadron calorimeter is 4.5 absorption length divided $\cos\theta$. Light collection scheme in the wall hadron calorimeter is the same as in the central hadron calorimeter. 576 photomultipliers are used for the endwall hadron calorimeter. Their parameters are summarized in table [2.4].

Central Electromagnetic calorimeter

Scintillator

There are many requirements to scintillator for the central electromagnetic calorimeter. High light yield is needed to reduce photostatistical fluctuation. Longer attenuation length is essential for a uniform response. Mechanical strength and uniform thickness are required for the stacking structure.

We developed a new type of scintillator for these requirements (Ref.[2.8]). It is based on molding type polystyrene doped with two fluors. Molded polystyrene have mechanical strength than excluded one. It is also easier to cut and handle.

Use of two kinds fluors makes attenuation length longer. The first fluor; b-PBD absorbs ultraviolet light which is emitted by polystyrene molecules excited by a charged particle and emits light with a wavelength of 360nm at peak. The second fluor BDP absorbs the light and

emits longer wavelength light. Longer wavelength light can be transmitted in plastics more easily . Thus longer attenuation length is obtained with two kinds of fluor. Fig.[2.6] shows the absorption and emission spectrum of these fluors and Y-7 wavelength shifters.

The concentration of these fluors was decided by an extensive study of light yield and attenuation length with ß-ray source. Finally, 1.0% b-PBD and 0.02% BDB in mass concentration was used for the scintillator. It is called SCSN-38.

The quality of the produced scintillator was tested on three aspects. The first is the light yield of small (5cm×5cm) pieces taken from every three layer of scintillator. The second is the attenuation length of 100cm×5cm strip taken from every 120 layers. Finally, thickness of every layer was measured at 130 points.

Results are summarized as follows.

Light yield deviation is 1.04%

Attenuation length is 94.7±10.1cm

Thickness is 5mm - 50.0μm ±88.9μm

Radiation damage was also measured (Ref.[2.9]) by exposing γ ray from a strong ^{60}Co source. It was examined that no major damage was observed for less than 10^3 Gy exposure.

Wavelength shifter and light collection

Before 1983 at the time of the development of the our scintillator , only one kind of wavelength shifter bar called BBQ was available in the market. Although the wavelength emitted by BBQ was well matched with the transmission spectrum of PMMA, the base material of BBQ, its sensitive region was not well matched with our scintillator. The absorption spectrum of wavelength shifter had to be matched with longer wavelength light of the new scintillator (Ref.[2.10]).

A new wavelength shifter which is sensitive to the longer wavelength was developed for the new scintillator UVA acrylic doped with 30ppm fluor . We called it Y7. Extensive studies

were performed for the properties of Y7. Y7 was found to be well matched with SCSN38 , have longer attenuation length and higher light yield than BBQ. UVA (Ultra Violet Absorb) acrylic prevent transmission of ultraviolet noise from Cherenkov radiation inside the wavelength shifter.

The wavelength shifters are laser cut with notches to from 1 in. wide fingers which are bent and gathered to glue to 24mm by 25.4 , 28.6 or 38.1 mm acrylic rod which pass through the hadron calorimeter. Quality of the laser cut optical surface was controlled by measuring the attenuation length of the sample taken every 10 cuts of the wavelength shifter. The 40 cm by 2.5 cm samples were measured their attenuation length excited by blue light from tungsten white lamp and filtered blue light filter. The attenuation length were controlled within 80±10cm.

The wavelength shifter plate at the each edge of the calorimeter sandwich collects light from the scintillator. Uniform response at each point of the wavelength shifter is needed for the uniform response of the calorimeter and linear energy response of the calorimeter. Earlier one correspond to the transverse moment of the wavelength shifter response map. And the latter one correspond to the longitudinal moment .

A thirty point wavelength shifter response map of every assembly (WLS , light guide and transition piece) was taken for the quality control. Response of a given shape of wavelength shifter is reproducible to ±2% in the transverse first moment. (transverse asymmetry corresponding to center to edge difference less than 2%) Mapping was made by micro computer controlled automatic 2-dimensional scanning machine. The excitation source for the mapping was light from a piece of SCSN38 actually used for the calorimeter , its cross section was 3cm by 0.5cm , excited by a ultra violet mercury lamp (539nm peak) . The detector at the end of the light pipe was a vacuum photodiode, made from a calorimeter phototube using the first dynode with low (50V) voltage, with electronic conversion from current to voltage for stability. Absolute light yield varies by 25% rms because of the light attenuation by UV damage to the source scintillator and instability of the mercury lamp.

With no corrections , the light output from the individual wavelength shifters varies from point to point on its collection face by as much as 45%. These are two reasons for this : first, the combination of oblique and obtuse angles between edges for a projective geometry shape give differences in collection by total internal reflection. Second, the effective attenuation length of the fingers about 80±10cm causes different transmission through fingers which vary in length from 15cm to 45cm. The thickness of the shifter material was controlled to better than ±10% (peak to peak).

We used a combination of three techniques to reduce the non-uniformity to no more than ±3%. First, the edge of the shifter farthest from the collection fingers was sanded and painted black to eliminate reflection. Second, a backing of controlled reflectivity was used to eliminate the remaining 25% variations. This backing utilized the fact that 25 % of the scintillator light passed through the 3mm shifter material and could be selectively absorbed or reflected back into the shifter to produce more green light. The backings were different for each of the ten tower shapes and consisted of black ink patterns silk screened onto reflective Alzak aluminum. In order to develop the patterns , response maps of each of 20 shifters for 15 wedges were averaged after culling defective assembles. Finally , response map can be corrected with painting black dots on fingers. On-line analysis at the mapping measurement informs where to put black paint. After the correction , mapping was made and re-correction was made if the map was not match within the standard map. Response maps of wavelength shifter before and after correction is shown in figure [2.7].

The light gathering layout is shown at figure [2.8] , with the light from the scintillator layers being redirected by the two wavelength shifters on each side up through the lightguides into the two phototubes per tower.

Strip chamber

The strip chambers determine the shower position and transverse development at the shower maximum by measurement of the charge distributions on orthogonal strips and wires. Specifications for the strip chamber are summarized in Table[2.5].

Photomultiplier

For the central electromagnetic shower calorimeter, bi-alkali 10 stage photomultiplier HAMAMATSU R580, with 38mm diameter were used. Tubes were burned in and tested against specifications in batches of 20 for about a week before installation (Ref.[2.11]). The base circuit shown in Fig[2.9] draws about 300μA at approximately 1000V giving a gain of about 10^5. The tube mounting has a soft iron outer shield 2.75in. outer diameter and 2.0 inch inner diameter and 8inch long. A standard commercial inner shield is attached inside with PVC cylinders. This shielding scheme was tested to make tube gain insensitive to axial magnetic fields of up to 200Gauss. A mounting spring loads the tube against the lightguide (air junction) and allows for twist-off removal of the tube and base, with azimuthal alignment. Photomultiplier high voltages are set and read back by a system of computer controlled DC motor driven potentiometers in series with the bases.

Photomultiplier readout saturates at about 350GeV and has a high gain (x16) readout for good pedestal systematics for minimum ionizing particles (about 300MeV equivalent). Photomultiplier current readout is provided for source calibration.

During initial operation of the assembled detector, large noise pulses were observed in the photomultipliers . These were largely confirmed to a few percent of the tubes and had average individual rates of about 0.02 Hz . But they caused a rate over the entire central electromagnetic calorimeter of 30Hz ; these pulses were also associated with noise spikes in the current measurement used for calibration. This noise was found to be caused by micro discharge between tubes and mountings, associated with particular mountings. These discharges

have been reduced by wrapping the tubes with 5 mill mylar, and in some cases, cleaning the paper wrapped on last inch of the transition pieces. Afterwards, these discharges give a total trigger rate of 1Hz.

Specifications for the photomultiplier is summarized in table [2-6].

Monitoring

Overview

After the construction of a calorimeter module, it was checked on the test stand using radioactive sources and cosmic rays. Then it was sent to NW beam line of Fermilab for the calibration by electron and pion beam at the energy of 50GeV.

In the beam line each module was exposed to beam at the center of each towers. Just before and after the beam exposure , the calorimeter was checked by movable ^{137}Cs source calibration system (Ref.[2.12]). The calibration constants for each tower were carried to the collision hall with the source calibration system. Source calibration on each module of the central calorimeter was performed every one month with the same source. The system can monitor the small effect caused by the magnetic field accurately at a level of 1%.

In addition to the source calibration system, two supplemental monitoring devices, a LED system and a Xenon flasher system, were employed for quick monitoring during the collision run.

The movable source system irradiates a layer of scintillator. Current signals are induced in the photomultipliers. A Xenon flasher injects light to the each wavelength shifter through a prism attached to the board. Green light emitted by a LED is drawn to the transition pieces by optical fiber. By each device we can monitor radiation damage , change due to aging or the magnetic fields. Furthermore the gain of photomultipliers can be measured by photo-statistics since the short term variation of LED signal is very small.

These independent monitoring systems enabled us to measure the effect of the magnetic field excited by the solenoid. Output from the source system increased while the gain of photomultiplier was not changed. We can conclude that the light yield from the scintillator was affected , but photomultipliers were not.

All the systems for each module are controlled by a control card mounted in a RABBIT (Ref.[2.13]) crate.

The movable source drive system

A ^{137}Cs 1.2×10^{8} Bq point γ source traverses the calorimeter between the eighth and ninth layer of scintillator, near the shower maximum. It is guided by two brass tubes and moves parallel to the beam direction. The drive machine was mounted on the end plate of the each wedge and was limited in its thickness to 3.8cm because of the space between module and magnetic return yoke. A DC motor drives wire at constant speed. Current induced in photomultipliers are sampled at every 0.3 seconds. The average activity for 51 source was $1.15\pm0.33\ \times10^{8}$ Bq with half life of 30.01years.

The xenon flash system

A xenon lamp pulse driven by a high voltage FET excites a scintillator rod to provide blue light to the wavelength shifters. An acrylic prism mounted on the edge of wavelength shifer introduces light through quarts fiber. Three of the fibers attached to the scintillator was connected to PIN diodes for monitoring. The outputs of PIN diodes are pre-amplified in the xenon flasher box and readout through sample and hold circuits on the calibration control card.

Xenon bulbs were selected so that they have stable and small time jitter. Typical jitter for accepted is 15ns.

The PIN diodes are relatively insensitive to temperature , an average temperature coefficient were -0.06%/°C. The ratio of any 2 PIN diode signals from a single flasher box yields an average sigma of 0.23%. The rise time of the flasher pulse is 120ns and 99% of the integrated charge is readout from the PIN diode pre-amplifier in less than 1μsec.

The LED flasher system

The light emitted by the LED flasher system is guided through two quarts optical fiber to holes of a transition piece just in front of photomultipliers.

A box for the system attached on each module contains three green light LED's, 8 fan-out fibers from each LED, two reference PIN diodes and charge-sensitive pre-amplifier for PIN's. Two of the LED's (LED0 and LED2) are monitored by PIN diodes. The third one (LED1) is monitored indirectly by PIN diodes; one photomultiplier views LED1 and LED0 and another views LED1 and LED2. Three LED's are fired successively.

The light output of the LED's is temperature sensitive , with an average temperature coefficient is -0.5%/°C. A probe monitors temperature in each box. The LED's are driven by a capacity discharge system controlled by a DAC with 13.5V at maximum. The rise and fall time is 70ns. A long tail in light output after the FET switch shut off is eliminated by a shunt resistor.

The beam test calibration

All the constructed wedge modules of the central calorimeter, 48 in the detector and 2 spare, were calibrated by 50GeV electron and π beam at the NW test beam line at Fermilab. Most modules were calibrated by electrons two times but 12 modules were exposed once because of the time limitation. In any case, source calibration by ^{137}Cs were performed immediately before and after the run , Typically, calibrations was done within a span of 2 days.

For calibration 50GeV/c electrons were injected to the center of each tower from tower 0 to 9. Because the Tower 9 has quite different geometry, the incident position was selected so that the output of photomultiplier is at maximum.

In data acquisition, on-line made event selection for calibration was done with several cuts. Position of the incident particle was determined by the strip chamber and was required to be within 1cm from the tower center in X (ϕ) direction. The momentum of a particle was measured by 2 beam chambers and it was used to scale the signal of each event to 50GeV/c. Timing information from the scintillator was used to reject events with more than two particle incident during the charge integration.

The gain of photomultiplier were adjusted to give 100,000 fC per phototube at above conditions. About 200 events were taken for a tower to give a statistical error of 0.15%.

Errors due to uncertainties in the gains of the integrated channels measuring the energy response and the current channels measuring the source response were less than 0.25% and 0.15% respectively. The major source of the error on the charge channels was the systematic uncertainty in the charge injection capacitor's value. The major source of the error on the current channels was the statistical error in the gain measurement.

These gains were measured in a test RABBIT crate with associated gating logic, using a linear fit to input pulses or currents over the dynamic range of the photomultiplier amplifier card.

Calibration measurements

Calibration constants measured at the test beam were used for converting digitized value to energy channel by channel. These constants are divided by a nominal value (such that they are near unity); hence one retains as much of the original 16-bit dynamic range of the ADC as possible.

The energy response of each channel of calorimeter is proportional to the current response for the ^{137}Cs source. The time dependent variation of each channel can be tracked by measuring current peak. Thus, for the test beam at time t_0 and a later time t:

$$\frac{Q(t)}{I(t)} = \frac{Q(t_0)}{I(t_0)}.$$

The energy gain G_e for a particular phototube (GeV/count) can be derived from the energy gain calculated in the test beam at time t_0, taking into account the peak source current measurements I (in nA) and the measured charge channel electronic gains G_Q (in fC/count):

$$G_e(t) = \frac{G_Q(t)}{G_Q(t_0)} \frac{I(t_0)}{I(t)}.$$

The source current terms contain the current channel electronic gain G_i (in nA/count) and a correction factor for the radioactive decay of the source. The dimensionless channel-to-channel variation Ge' is defined in terms of the energy gain G_e (GeV/count) and a nominal energy gain:

$$G'_e(t) = \frac{G_e(t)}{G_e(nominal)}.$$

Short term corrections from the time of the laser source calibration t_1 can be made with one of the flasher system's signals Q_f, assuming $G_Q(t) = G_Q(t_1)$:

$$G_e(t) = \frac{Q_f(t_1)}{Q_f(t)} G_e(t_1).$$

One would prefer to use a signal Q_f with as small statistical error as possible. As will be shown in the next section, this proved to be the ratio of phototube signal to PIN diode signal for the xenon flasher and the phototube signal itself for the LED flasher. In practice, the constants are not a continuous function of time, but are measured at decrease intervals: from

2-4 weeks for the source measurements, and daily for the flasher measurements. Convenient rearrangements of the values used in the above equations - $[Q(t_0)/E(t_0)]/I(t_0)$, $G_Q(t)$ and I(t) - are stored in a calibration data base, and retrieved to form values $G_e'(t)$ which are also stored in the data base for downloading to the MX front end scanners.

Performance

The distribution of the percentage difference between the results of two source runs for 956 phototubes has a mean and RMS of 0.02±0.61%.

The distribution of calorimeter response for xenon flash run is shown in Fig.[2.10a]. This peak corresponds to a particle of 20-40GeV energy. The output distribution by PIN diode is shown in Fig.[2.10b] And figure [2.10c] shows event by event response of calorimeter normalized by PIN output. It has mean and RMS 8040±160.

The response for LED corresponds to a particle of 200-300GeV. Its RMS is on the order of 0.8%.

Fig.[2.11] shows the difference between two runs at an interval of a day for xenon and LED. Output for xenon was normalized by PIN diode. Raw outputs are compared for LED.

Fig.[2.12] shows the long term (9 months) stability of calorimeter measured by sources. Most of tubes are stable but some tubes has gradual change. The primary source of these variations is change in the photomultiplier gains, either intrinsic changes in the phototubes themselves or changes in the high voltage for the tubes.

Fig.[2.13] shows the long term variations for the xenon and LED systems; variations are typically of order a few percent and the two systems generally track one another. These systems are intended primarily for short term corrections, and large shifts are carefully verified before use as corrections.

Three module were re-calibrated one month after the original calibration. Between the calibration they were transported to a storage site. Fig.[2.14] shows the percent difference

between the two measurements. The reproducibility corresponds to an error of ±0.4% and the change of 0.2% seen is just the loss expected from radioactive decay.

Though all output of the calorimeter are normalized by monitoring systems, smaller variation between channel to channel is desirable for the fast out trigger system as well as for maximizing dynamic range of ADC. Fig.[2.15] shows channel to channel gain variation with mean and RMS of 1.03±0.08%. The main source of the variation come from the reproducibility of high voltage settings and aging in two years. Fig.[2.16] is the same plot as Fig.[2.15] but for the original calibration done at the test beam. Fig.[2.16] shows the actual changes in energy response from the test beam (1984-1985) till the most recent run (May 1987)

Magnetic field effect

When the superconducting solenoid is activated, there is magnetic field in the electromagnetic field in the central electromagnetic calorimeter. It is estimated as 0.012 T in the middle of calorimeter 0.086 T at the tower 9 and 0.002-0.004 T at the position of phototubes. Phototubes are shielded by μ-metal so that the magnetic field can be ignored.
The increase response was observed by the source measurements while no change was observed by the LED monitor. The relation between source response and magnetic field in the solenoid is shown in Fig.[2.17]. The same effect was also seen at the endwall. This magnetic field effect has been seen in other organic scintillator and is well known phenomenon of these scintillator's organic chemistry (Ref.[2.14]).
This effect was taken account in the calibration automatically.

Central and Wall Hadron Calorimeter

Light collection system

Central and wall hadron calorimeters employs plastic scintillator; PMMA doped with 8% naphthalene 1% buthyl-PBD and 0.01% POPOP. The averaged size of the scintillator is 1×35×70cm3.

Light collection scheme around a scintillator layer is shown at Fig[2.18]. Wavelength shifter strips lying the each sides of the longer sides of scintillators collects light. WLS is 0.5cm×1.0cm UVA PMMA strips doped with Laser DYE#481, which has emission peak at about 490nm. The WLS are connected optically connected to UVA light guides of the same cross section. The light guide from the each layer has different length. And light in the light guide is attenuated . Different types of the neutral optical filters are inserted between WLS and light guides of each layers to reduce layer- by layer difference.

These light guide from the each layers are combined and guided to the transition pieces which are made by the same material as WLS. Transition piece converts square cross section of light guide to the circular one of Photomultipliers. Two photomultiplier on opposite sides in azimuth collect light.

Photomultipliers is chosen from the point of view of quantum efficiency, linearity up to 40mA and stability. For the central 12 stage THORN-EMI9954 was chosen. For the wall 10 stage THORN-EMI 9902 was chosen. Instability of the gain after the large current was observed . This is because of the tubes operates at the gain of 10 times lower than the design value. To minimize this instability green light is injected producing anode current 100nA between the bunch crossings. This correction make less than 1% of tubes change gain 2%.

Anode signals are converted at RABBIT readout system with 16bit full scale at 750pC. This system can read anode current and arrival time of signal with 16bit TDC of full scale 3.2μSec.

Design Constrains

The central hadron calorimeter was designed to have best possible both energy resolution and uniformity.

The central hadron calorimeter employs steel plate of 2.5cm thickness as a sampling material which is expected to have 50%/√E(GeV) resolution. From the total design total thickness of 80cm at normal incidence was the result. It contains 95% of 50GeV hadronic shower. This degrades the calorimeter resolution at the higher energy and makes the muon identification by the drift chamber behind more difficult. 2.5cm 32 layers was chosen for the better resolution at lower energy based on the prototype test result.

For the endwall calorimeter 5.0cm sapling was chosen , since for a given Et total energy to the endwall is bigger than factor √2 in average.

Special attention was paid for keep uniformity both angular and longitudinal (depth) direction.

Wavelength shifter strips placed on both longer side makes angular response of a scintillator uniform. Fig.[2.19] shows a map for a scintillator layer irradiated by Sr-90 ß source. The variation in a scintillator is smaller than 10%. The non-uniformity is further smoothed out by alternating the WLS readout in successive calorimeter layers.

A uniformity of longitudinal response i.e. equality of layer to layer of calorimeters was achieved to better than 10% by following way.

As the size of scintillator large , the light output to the outside smaller because of light attenuation inside the scintillator. Coupling with a proper attenuation length WLS strip to the scintillator make a coarse correction.

And a neutral density filter inserted between wavelength shifter and light guide. They reduce 20% of light output of each layer. The uniformity along the longitudinal direction was checked by measuring current induce by ^{137}Cs source moving longitudinally along the tower. Figure [2.20] shows the longitudinal uniformity.

Monitoring devices

To monitor a set of components of the hadron calorimeter four kind of monitoring device as follows employed.

A pulsed laser provides light through optical fibers to transition blocks in front of photomultipilers to monitor their gains.

A point like Sr-90 ß source back up the laser system by being inserted between light guide and WLS strips.

A point source of ^{137}Cs gamma ray irradiates a scintillator layer moving at a constant speed at a fixed depth of calorimeter. It induces current to the phototubes.

Finally , a line source of ^{137}Cs γ ray inserted longitudinally irradiates every layers in a tower simultaneously.

The last two systems monitor aging effect comparing their result to that of the previous systems.

The Pulsed Laser monitor

A nitrogen laser emits pulses of wavelength 320nm at cycle of 15Hz. It generates pulse at the power of approximately 0.3mJ/pulse , width a few nanoseconds and less than 5% instability.

The laser beam is divided into 6 beams and transported to calorimeters with optical fibers. At the detector , it terminated by a light distributor in which a scintillator disk (10mm thick and 70mm in diameter) is illuminated by the fiber. The scintillator disk emits light and

thirteen fibers are attached to the edge of it. The other end of the fiber is attached a transition piece in front of the phototube. One of the fiber is monitored with a reference phototube which stands in a temperature stabilized box in a counter room. The reference phototube is monitored by light from a NaI crystal excited by a ^{241}Am α-ray.

The movable point source system

A point-like 4.8×10^7 Bq ^{137}Cs γ source run in a module at constant speed under computer control. Inside a thin stainless tube is fixed in all towers of a module along the scintillator center lines. A source stay inside a lead house mounted outside of a module. This system measures the product of the response of scintillators at a single level and the gain of phototubes.

The point ß-ray source system

A point like ß ray source can be inserted into the transition block and phototube manually. Because the completion of the laser system delayed this system was used for primary stage of the calibration for the phototube gain.

The line source system

A 1.6m long , encapsured in a flexible 0.5mm stainless steel tube ^{137}Cs line shape source illuminate all scintillator in a tower at once. It can be inserted to a larger diameter stainless tube fixed inside of the module.

Calibration

All the tower and module of the central hadron calorimeters were exposed at the 50GeV π-on beam line.

At the first stage of the production , two modules were calibrated by the beam. The gain of the phototubes were set to get a gain of 2pC/GeV adjusting high voltage. The mean current Ic induced by the skin source was also recorded.

At the production of the each modules the high voltage of their phototubes were set to reproduce the proper Ic. At that time current by ^{137}Cs movable source Ics and by ^{90}Sr point source Isr were also recorded.

Then the module was send to the test beam line. At the beam line, the phototubes were supplied their high voltage set at the production line.

Before and after the calibration run by 50GeV/c pion beam, Ics and Isr were measured.

The reliability of the source calibration was checked by re-calibrating seven modules after the period of several months. Fig.[2.21] shows the pion peak of the re-calibrated module normalized by Ics. One can find the calibration constant is reliable at less than 1% deviation.

^{90}Sr point source was replaced by the laser system at the real experiment.

Once the 50 modules were tested the similarity was checked by correlating , again through Isr and Ics, the observed pion pulse heights to the average current Ic. Fig.[2.22] shows the module can be calibrated at the level of 3-4% with the source systems only.

Endwall modules calibrated relying on these results. Two modules of endwall calibrated with 50GeV π-on to provide 100pC from the tubes. The current induced by line ^{137}Cs source illuminating whole of the tower was recorded. This calibration constant was proved to 2% level of deviation at the different run.

At the collision hall, after the high voltage were set, calibration by movable ^{137}Cs source and by laser are performed to provide a reference for each photomultiplier.

Magnetic field effect

Since the endwall calorimeter is a part of the magnetic circuit, its scintillator may affect by its fringe field. At the endwall the effect of the magnetic field was seen as well as the electromagnetic calorimeter. Fig.[2.23] and Fig.[2.24] shows the difference of calibration value of tube by tube at magnetic field 0 T and 1.5T , current induced by ^{137}Cs and Laser system respectively. The Ics increased at 5% , on the other hand the laser induced pulse height changes 1%. These result means the light output from the scintillator increases by the effect of the fringe magnetic field and the photomultiplier gain did not changed when the magnetic field was activated.

Radiation damage

Attenuation length of the scintillator was measured for different dose value and the result is shown in Fig.[2.25]. It varied linearly with the absorbed dose and decreased by factor of 4 with 150Gy. The light output at the zero distance dose not change.

Cosmic ray test

Overview

As central calorimetry modules were completed, they were set up and tested on a cosmic ray test stand (Ref [2.15]).

For the electromagnetic calorimeter the principal objective of the test is to obtain precise response maps over the face of each tower in all 48 module (plus 2 spares) in order to exact uniformity correction functions for the off-line analysis. The measurements must be precise enough to achieve an overall corrected uniformity at the 1% level as required by the CDF physics goals.

For the hadron calorimeter, the calibration of several basic characteristics of the calorimeter is performed by taking advantage of the use of minimum ionizing particles.

The mapping measurement for the each electromagnetic calorimeter was competed with cosmic ray . Because the time for the beam test for each module was limited , a few module was measured their response map in detail.

In addition with making map, cosmic ray test was a important process for the quality control of the both calorimeters in the production of them.

Data were taken in June 1983 following completion of the dedicated cosmic ray test stand in the Industrial Building IV at Fermilab. Testing was continued essentially without interruption until the last module was completed in June 1985.

Test Stand

In order to minimize systematic variations from module to module and allow data taking to proceed unattended for long periods of time , a dedicated cosmic ray test stand facility was constructed. Functions provided by this test stand include triggering on isolated penetrating cosmic ray muons , precise tracking of the muon trajectories , computer based data acquisition and on-line monitoring and gain calibrations for both the read-out electronics and the calorimeter towers.

Fig.[2.26] shows two side views of the cosmic ray test stand apparatus with a calorimeter module in place. Three planes of trigger scintillators called UPPER , LOWER and SIDE are used to define the ten trigger roads which correspond to the ten projective towers of the calorimeter module. The scintillator pieces were cut to match the projected size of each tower individually , virtually eliminating any trigger from muons which cross tower boundaries. Two fold coincidences of either $U_i \times L_i$ or $S_i \times L_i$ determine the ten trigger roads where i refers to the tower number

To ensure that the energy of muons satisfying the trigger requirement is in the region of minimum ionization and reduce the effects of multiple scattering and straggling , an additional 20.3 cm thick iron absorber and included in the trigger requirement. Since the projective tower trigger roads are already established by U,S and L counters, the hardner was implemented as two large counters . The trigger counters were consisted with polystyrene based plastic scintillator viewed by photomultipliers.

Trajectories of muons are measured by three devices. At the top of the module four layers of drift chambers are installed, this is a standard CDF module. Specially made drift chambers covers the side of the detector. Though, side and bottom drift chambers have different geometry from the top chambers , the structure is the same ; $6.4 \times 2.5 cm^2$ rectangular cell , 2mm alternative offset to avoid left right ambiguity , -2.5kV at wall +3.1KV at since wire high voltage and 50/50 argon/ethane mixture of gas containing 1% ethyl alcohol. Longitudinal position along the wire is measured by charge division. Transverse resolution of 250μm on the 3.1cm drift space and longitudinal resolutions of 4.7cm on the 230cm long sense wire achieved on this test.

Trigger signal was made with coincidence signal of trigger counter U × L or S × L by NIM type electronics module. Event rate from the total system is 1.6 Hz and the trigger rate to the each counters are consistent with the expectation from the sea-level cosmic ray energy and angular distribution (Ref.[2.16]).

Signals from the calorimeter phototubes and strip chambers are read by prototype versions of the CDF front end electronics. The same data acquisition system facilitate comparisons with test beam data and collider operation.

Drift chambers and hit pattern of the triggers were read by commercial CAMAC type ADC , TDC and input register system. The system also controlled LED , Xenon flash lamp and charge injection calibration .

Total of data readout and control was performed by a VAX/730 minicomputer through CAMAC and Jorway model 411 serial branch driver. Data were stored in magnetic tapes and analyzed off-line.

Data acquisition procedure

Before beginning the extended period of dedicated cosmic ray data acquisition several ^{137}Cs source calibration runs were performed for both the EM and hadron calorimeters. The voltage across the feedback resistor in the front end photomultiplier charge integrator is proportional to the current supplied by the phototube and is available to the scanning ADC for digitalization. A source calibration run consists of moving a ^{137}Cs calibration source through a brass tube installed in the calorimeter at shower maximum and mapping the response of each phototube as a function of position of the source. The data are fit to 6th polynomial function to obtain a peak response of each phototube which is maintained as primary calibration figure. Source runs were again taken at the end of cosmic ray data taking. The calibration runs were used only as a monitor of the response of the EM phototubes and were not used to make any correction on the cosmic ray data.

Comparisons have been made of the source response difference at the beginning and the end of a cosmic ray data taking for the EM phototubes. These indicate that the response is quite stable over the typical 4-5 days period during which cosmic ray data are taken. Figure [2.27] shows the percent difference between a start and an end source responses for each phototube from 26 modules. The average difference is -0.21% and indicates that the tubes settle to a slightly higher gain during the course of cosmic ray data taking. This drift is presumably due to the fact that the final voltage adjustment on the phototubes were made just prior to taking the set source calibration runs at the beginning of a cosmic ray data taking. Thus, the gain may not have settled completely at this time. Most phototubes drift less than 1% during the cosmic ray data acquisition. ,The drift has the effect of smearing out a minimum ionizing peak slightly.

Since each mesh point in a tower is affected in an identical way and the response of each mesh point is normalized to the central response , this small drift has a negligible effect on cosmic ray response maps.

Before beginning the several day period of a dedicated cosmic ray data taking, a pedestal run was taken to provide both a final check the complete system was operating correctly and a set of initial pedestals for subtraction from the signals. During the extended data run, pedestals were updated once an hour under the computer automation by taking a sample of 200 pedestal events triggered by an external pulse generator. The pedestals generated in this way were used for on-line analysis only. As is discussed below the off-line analysis re- calculated pedestals every 250 events using data from non-trigger towers.

During cosmic ray events, data were written on a computer disk. A run consisted of 40,000 cosmic ray event triggers and took approximately 10 hours. Data taking proceeded essentially automatically with a computer handling generation of new runs and with a operator intervention only to copy event data file from a disk to tape and to check that the entire system was operating correctly. The disk cleanup was a part of an operator submitted batch jobs that copied events to magnetic tape, deleted the file from the disk providing a space for the next run, and ran the first pass off-line analysis on the copied events. Doing the off-line analysis immediately at the completion of the run had an advantage of giving us a quick feedback on the data visually in a more detailed than on-line.

The quality of data was monitored by a variety of histograms that were accumulated through the extended run period. Quantities histogrammed included pedestal subtracted pulse heights for the each EM and hadron phototubes, the several largest pulse heights from the strips and wires in the strip chamber, hit profiles of the strips and the wires , number of wires and strips hit per event, hit patterns for the muon drift chamber TDC's and ADC's relative trigger rates of each tower for cosmic rays , and words recorded per event. These histograms were checked every 10 hour as a part of operator's job.

Electromagnetic calorimeter

Front end electronics calibration

All front end electronics serving the phototubes , strip chambers and muon drift tubes proved to be quite stable over a period of months. Since the phototube pulse heights were critical measurements made at the test stand, the gains of the charge integrators and the current readout channels were routinely re-calibrated and updated in the off-line analysis every two weeks. Calibration was performed in a front end electronics test crate with the ADC scanner interfaced to an IBM PC. Known charges were injected to the amplifier by charging a 472pF capacitor with pulse from a programmable BNC 9010 pulse generator. The observed pulse heights from the charge integrator were fit to a straight line to obtain the amplifier gain. The current channel was calibrated by injecting current from a Keithley 261 picoampere source. Figures [2.28a] and [2.28b] show respectively, representative plots of channel gains as a function of time for the charge and current channels. The current channel gains shown are from two prototype amplifier boards. The final version of the electronics has a nominal current channel gain of 11 pA/ADC count and boards of this type were used during the last three months of operation of the test stand. The data of Figs.[2.28a] and [2.28b] are shown since these cards were in serve for a longer period and have more calibration data available. The stability of the newer electronics have been found to be equal to that of the prototypes. The obvious feature of the charge calibration plot is the similarity in the gain fluctuations from channel to channel. This suggests that the front end electronics is more stable than the calibration system. The absolute gain of a charge channel is uncertain to a level of as much as 2% while the absolute gain of the current channels is known to approximately 0.5 % which is quoted accuracy of the current source. Ignoring systematic variations and considering only the relative stability, the figures indicate that the gains of the charge amplifier are constant to a level of 0.76% while the current gains are stable to 0.10%.

The electronics for the muon and strip chambers did not need a periodic calibration since the gains were stable enough for the accuracy required for the tracking. The muon TDC and ADC system was only calibrated when a CAMAC module was replaced. The gains of the strip and a wire amplifier for the strip chamber were preset to within a few percent via adjustable capacitors, to 0.25fC/ADC count and 1.0fC/ADC count, respectively, and no calibration was required when replacing the electronics boards.

Data analysis

A total of 50 modules were tested at the cosmic ray test stand. Typically about 200,000 events were used for making a response map for each module. With a total of 200,000 events and a required statistical precision of 1 to 2% , it was possible to subdivide the ten towers into 650 elements of grid. The size of mesh was typically 4.4cm by 3.3cm for towers 0-4 and 4.4cm by 4.0 cm for towers 5 to 9 on the plane at the strip chamber depth.

The response was obtained from the sum of 2 tube outputs for each mesh element. The measurement of response of minimum ionizing particles is such as was typical curing normal data acquisition. Correction for the time variation of pedestals was made in the off-line analysis.

Response Maps

The definition of local coordinates in a tower is shown in Fig. [2.5], Where Z (also θ)is the coordinate along the beam direction and x (also ϕ) is the one around the beam axis in the configuration of proton-antiproton collisions. The boundaries of X and Z in a tower are-12cm<Z<12cm and -23cm <X<23cm, respectively. The mesh elements on the plane of the strip chamber are defined by dividing the strips into 65 groups in Z and wires into 10 groups in X. As stated previously, 200,000 cosmic ray events per module gives a statistical precision of

1-2% for each mesh element. The response data is normalized to the response in the central area of a tower, |X| < 8cm and |Z| < 5cm in this case. Although the pulse height distribution of muons is expressed by a convolution of 31 Landau distributions, a fit to a Gaussian function was adequate to estimate the peak value. For incident particles crossing the tower boundaries, which are mostly rejected in triggering, the response is obtained by summing the pulse heights in two adjacent towers.

Parametrization

The calorimeter response along X was expected to be symmetric from the structure of EM calorimeter. It is observed that the light attenuation curve viewed by a single phototube is not a simple exponential function. The main reasons for this seem to be due to the wave length dependence of the attenuation and light reflection at both edges of scintillators contacting with the wave length shifters. As for the edge, the light collection is different from that in the central region due to the presence of a gap between neighboring waveshifters as mentioned in section 3.1.1.

In fitting the response in X to a function, the following parametrization is chosen: P0+P1 = A cosh (X/W), where P0,P1 and the phototube pulse heights, and A and w are parameters which are functions of Z. The following parametrization is also made: P0/P1=B exp(-2X/L), where P0,P1 are the phototube pulse heights, and A and W are parameters which are functions of Z. The following parametrization is also made:

$$P0/P1 = B\exp(-2x/L),$$

where B and L are parameters which are functions of Z and L corresponds to the conventional attenuation length.

Time Variation of pedestals

Data taking runs continued for about four days in order to accumulate 200,000 events per module. A significant time variation of pedestals against the muon pulse height was observed during the run. The time variation of pedestals in the worst case amounts of 8% of the muon peak value. The correction was made in the off-line analysis by reading all the phototube in a event . Pedestals of tubes which did not associate trigger were accumulated event by event. 250 counts of pedestals were taken every 3 minuets for the re-calculation.

Results

Muon Pulse Height Distribution

A typical pulse height distribution for cosmic ray muons viewed by a single phototube is shown in Fig [2.29a,b]. Fig [2.29c] is a distribution viewed by two phototubes i.e. (p0+P1)/2. As seen in Fig [2.29], distributions have RMS width of 20-21% and 16-17% respectively.

The main contributions to the width of the peak are:

Statistical fluctuation in sampling photoelectrons,

Landau fluctuation in energy deposition in the scintillator,

Variation in path length due to different incident angles of the muons,

Position dependence of the response.

Fig.[2.30] shows the number of photoelectrons per GeV for each tube of a module obtained with LED measurements and the nominal gain calibration figure of 2pC/GeV per phototube. The average number of photoelectrons per GeV is estimated to be 115 from LED measurements for several modules, and was confirmed by the electron beam test. Thus the

fluctuation in photoelectron statistics 1/√(Number of photoelectron) is 17.0% for an EM shower energy of 0.3GeV, corresponding to the calorimeter response for a muon.

Landau fluctuation in the multi-layer traversal was calculated by a Monte-carlo simulation. The value ranges 4.5% to 9.7% depending on the tower number. These values include the effect of variation in path length which varies 1 to 6% with increasing tower number. The value 4.5% in tower is consistent with the value calculated from a simplified formula given, for example, by Amaldi (Ref. [2.17]) which gives 4.5% typically. The variation in the response due to position dependence is also estimated by a Monte-carlo calculation to be 11.5% for a single tube, 2% for (P0+P1)/2.

Thus the total contribution is expected to be about 21-23% for the case of single tube and 13-16% for the two tubes. These estimations are consistent with the observations.

The average muon peak value for all towers in the EM calorimeter was 623fC±37fC. Since the calorimeter gain was set to be 2pC/GeV/Phototube, the calorimeter response for a minimum ionizing particle was estimated to be 0.31GeV. The average and RMS value of the peak pulse height for each tower over 44 modules are tabulated in Table [2.7].

We notice here the peak value for cosmic ray muons is different from that of punch-through particles (mainly no interacting pions) of 50GeV at the beam test as shown in Fig[2.31]. The data for all the towers 0-8 of 6 modules are plotted in the figure. No significant tower dependence is found. It is seen that the test beam data are higher than the cosmic ray data by, on the average, as much as 10%. This seems to be due to the fact that when the energy of a muon and a punch - through particle increases other processes than ionization, such as bremsstrahlung , pair production and so on, take place more frequently in the calorimeter and give a higher most probable peak value.

Similarity of the response map

Study of the similarity of the response maps tower-to-tower and module to module over all modules is the main purpose of the cosmic ray test. A total of 41 modules with the data having more than 150,000 events were used for the study.

The similarity for module-to-module is defined in terms of the deviation from the average response value at each mesh point over all the modules tested. The average response is shown in Fig.[2.32]. The overall rms deviation was obtained as 1.5%, where the data of tower 9 are excluded. The value still involves a statistical uncertainty.

We define the intrinsic systematic dissimilarity as follows:

$$D_{ij}^2 = \frac{1}{N}\left[\sum_m (R_{ij}^m - R_{ij})^2 - \sum_m dR(stat.)_{ij}^{m\,2}\right],$$

Where R_{ij}^m is the normalized response in a mesh element (i,j) of module m, R_{ij} is the average response for all N modules in mesh element (i,j) , $dR(stat)_{ij}^m$ is a statistical component of the deviation of response in a mesh element (i,j) of module m.

The mean value of D and its RMS over the whole area are 0.95% and 0.47% respectively. Here no tower dependence on D's was observed. However these exists a dependence of D on the regions in a tower. Fig.[2.33] shows the distributions of D's in towers 0 -8 for four different region, i.e. the entire region, the central region (|x|<17cm, |z|<10cm), the theta edge region |x|<17cm, |z|>10cm ,and the phi edge region |x|>17cm,|z|<12cm. As is seen in Fig.[2.33] the dissimilarity obtained in the central region is 0.76%. The average and RMS values of dissimilarity for each tower are calculated with all the 41 modules and are listed in Table[2.8a] dividing into several regions.

Next,the X dependence of D was examined. The average dissimilarity along a fixed x is presented in Table[2.8b]. The average value increases as X increases. The value in the region of |x|>17cm exceeds 1% for towers 0-8.

Response map Parameters w and L

The parameters w and L were obtained for 65 points in Z defined by strip groups, where each tower consists of 6-7 groups. A typical response map in x at the Z center in a tower is shown in Fig.[2.34a], where the Solid curve is fit to Cosh(x/w) for the region |x|<17cm. The distribution of the ratios of two tube outputs in x at the Z center is shown in Fig.[2.34b], where the solid curve is fit to exp(-2x/L) for the same region above. The errors in w and L in these fittings are 1% and 5% respectively.

Figures [2.35] show the distribution of w's and L's at the Z center of each tower over 46 modules. The average values of w and L are 55.0 cm and 99.3cm respectively. Here we examine the tower to tower and module to module deviations in w's and L's obtained at the tower centers. The result is listed in Table [2.9] and indicates that the deviations from tower to tower within a module for both quantities are significantly smaller than those for module to module. This may be a consequence of the quality control in production of the calorimeter modules.

Fig. [2.36a] and [2.36b] show the Z dependence of w's and L's , in which the data points are normalized by their average values at tower centers. As is seen in the figures, the mean value of L increases as the hit position becomes closer to the tower boundary, while that of w does not show clearly such a trend within the spread of 9% RMS. It is due to the different incident angle of cosmic rays changing track length within a certain acceptance. w is more sensitive to the effect than L because the ratio of phototubes cancels above effect.

To test this point we chose a module with high statistics with uniform path length of tracks. The upper and lower muon chambers were divided into 12 subdivision and a track was required to pass the same subdivision. w was reduced by 12.3% while L was reduced only 3.5%. This shows that the value of L is reliable with low statistics.

L increases at the tower boundary. This is due to a gap of the light collection at the tower boundary.

Z dependence of L is expressed by polynomial function:

$$L = L_0 (1 + c_1 z + c_2 z^2),$$

Where L_0 is the value of L at the tower center of each tower. The fits are shown in Fig.[2.37]. The average and deviation for each tower with 46 modules are summarized at table [2.10]

Figure [2.38] shows the correlation plot between L and w using the values at the center of tower 0-8 over 46 modules. We note that a clear correlation can be seen dividing into two groups. The difference in the two groups is related to the different production batch of scintillator. the correlation in each group are w=0.6L and w=0.5L respectively.

Finally we mention the magnitude of deviation of the response reflected from the deviation of w. The average value of w is 55.0cm and the module-to-module deviation is 9.2%. The deviation of the response R in terms of that of w is expressed as follows,

$$\frac{dR}{R} = \frac{dw}{w} \frac{X}{w} \tanh\left(\frac{X}{w}\right),$$

where R =A cosh(X/w). At X=15cm and 20cm ,for example, dR/R are 0.7% and 1.25 respectively., which are consistent with the results of dissimilarity shown in table [2.8b].

Long term stability

We have studied the long term stability of the EM calorimeter by comparing the cosmic ray data for a particular module (#17) taken at an interval of 7.5months.

The following possibilities would cause the deterioration of the calorimeter response.

a) Damage to fluors in the scintillator

b) Decrease in the transparency of the scintillator base.

c) Deterioration of the light collection system which consistent of WLS and light guide.

d) Tube gain

The pulse height was measured to estimate effects (a) to (d). The measurement of the attenuation length : L was useful to estimate (b)

Following is the conclusion

The deterioration in muon pulse height is estimated to be -2.0±0.6% per year.

The deterioration in the attenuation length :L is -2.7cm±2.9 per year.

Comparison with Beam test

For the mapping purpose in the beam test , 5 modules were scanned precisely with 50GeV electrons. The response at each point was measured with a statistical error of less than 0.5%. The mesh size was chosen to be 1cm by 1cm, while the impact point separation and the beam size were 4cm and 2.5cm diameter.

The similarity for each mesh was examined in the same manner as that for the cosmic ray data. The overall rms deviation in dissimilarity is found to be 0.8%. The deviation in the central area: |x|<20cm and |z|<10cm: is 0.6%.

Summary

The similarity of response maps is measured to be within 1% for the central region :|X|<17cm |z|<10cm: and 1.2% on average for the outer region.

The parametrization of the correction function for the response maps in X and Z was performed

The correction parameters for the mapping from the cosmic ray test is combined with those from the electron beam test in order to achieve an even producibility for all modules. The

resultant correction function is capable of obtaining reproducibility with an deviation 1.1% except for the region of phi edges.

The long term stability of the calorimeter response is tested with cosmic rays. Possible deterioration is estimated to be 2.0% ±0.6 per year.

Hadron calorimeter

Preparation and monitoring of phototube

The high voltage of the hadron calorimeter phototubes was determined in the following way.

First of all, the light output from each scintillation plane was made equal, by irradiating each plane with a ^{137}Cs source and by inserting neutral density filters between each wavelength shifter-UVA PMMA strip transition. This adjustment was done in the production line before mounting the wedge module on the cosmic ray test stand.

Let us define h(ij) the light collection efficiency of the i-th tower of the j-th wedge. The signal charge q(i,j) is related to the phototube gain g(i,j) and to the light yield S(i) generated in a tower by the relation:

$$q(i,j) = S(i) \times h(i,j) \times g(i,j)$$

q(i,j) was made j- independent by adjusting the gain. Since the light guides are independently equalized there may be small g(i,j) differences event between two phototubes viewing the same tower.

This adjustment was performed by running a ^{137}Cs γ -source along a fixed path on both longitudinal sides of each tower and by changing the high voltage until the same current was

reached for all phototubes. A reference gain was chosen for all phototubes such that a 50GeV/c pion would give a charge of 100pC.

To monitor the phototube gain at any time two independent ways are provided: a ^{90}Sr ß-source can be located in a reproducible position on the light guide in front of the photocathode; a ^{137}Cs source can be driven through different towers at a fixed calorimeter depth.

Results

Muon Pulse Height distribution

Figure [2.39] shows a typical muon pulse height distribution obtained in the cosmic ray stand, integrated over the full polar and azimuthal acceptance of tower. In order to ensure that muon trajectory is fully contained, we require the pulse height in each adjacent tower to be less than 1.5 time the width of the pedestal fluctuation. We fit the muon pulse height distribution with a Gaussian and find the peak value to be close to the most probable value of the distribution. The phototube gain has been normalized to the reference gain. The ADC gain has been measured separately.

Fig [2.40] shows the distribution of the muon peak values for a sample of 12 wedge modules. Measured values are corrected for different tower thickness. Table [2.11] shows the average and standard deviation of the muon peaks distribution for all towers 0 to 3. We conclude that the calorimeter equalization and phototube high voltage setting are established with an accuracy better than 6%. The last column in Table [2.11] shows the test beam result which is in a good agreement with cosmic ray data.

We compared the cosmic ray muon data with 50GeV pion data for a sample of 5 wedge modules. table [2.12] shows the averages and the widths of the pion peak distributions for

towers 0 to 3. The 50GeV pion and cosmic ray muon responses are found to be proportional within a few%. The last column in table [2.12] express the muon sigma in GeV.

Number of photoelectrons

Using the three planes of tracking chambers, we selected muons passing through the tower center within ±2cm. The width of the pulse height distribution is contributed by statistical fluctuations of the number of photoelectrons (N_{pe}) and by fluctuations of signal itself. To get rid of this last effect we derived the number of photoelectrons from the widths of the log(R/L) distributions, as well as from the width of the (R+L) ans (R-L) distributions. If we assume the response of two calorimeter sides to be equal, the number of photoelectrons is related to those distributions in the following way:

$$N_{pe}(1) = \frac{2}{\sigma^2 ln\,(R/L)},$$

$$N_{pe}(2) = \frac{2\mu^2\,(R+L)/2}{\sigma^2(R-L)},$$

where σ and μ indicate the RMS and the mean of the distribution. Table [2.13] shows the results for towers 0 to 4.

From the Monte-carlo simulation we expect Npe(1)<Npe(2) and the true photoelectron number to be close to the average of Npe(1) and Npe(2). Table[2.13] confirms the systematic expected difference between two methods of calculation.

Since the equivalent mean energy released from a muon in tower 0 is 1.8±0.3GeV (see table[2.14]), the produced number of photoelectrons/GeV is 11±3 when observed by a single phototube. The value should be considered as a lower limit because the long term period of data taking (about 11 hours) caused an increase of the RMS.

Attenuation Length of Scintillator.

The light attenuation length in the calorimeter was measured by selecting muons passing at a distance of ±11.5cm from the calorimeter Z-axis, in the region 4cm wide along the same axis, on the plane separating hadron and EM sectors.

For those tracks the attenuation length L is connected to the ratio of the phototube pulse heights as L=23/|log(R/L)|, where R and L are the mean of the pulse height distribution as seen by each phototube. Table [2.14] gives the attenuation length calculated b for towers 0 to 3. The average attenuation length is 120±10cm.

Uniformity check

The calorimeter response uniformity as a function of the muon position was also studied.

Using the track chamber information, a tower is divided into three equal regions along Z and into three different X regions, namely -30cm≤X≤-20cm and 30cm≤X≤20cm. The nine mesh elements are defined on the middle Y plane of the calorimeter.

Fig.[2.41] shows a typical distribution of the average pulse heights of single phototubes for cosmic ray muons entering different Z regions with X between -5cm and +5cm. Figure[2.42] shows the distribution of the average sum of the response of the phototubes for all X and Z regions, From the full width at half maximum of the distribution we estimate a response uniformity better than 2.8%.

Conclusion

We measured some properties of the central hadron calorimeter by using cosmic ray muons.

Response uniformity is found to be better than 3%. The photoelectron yield in a tower is measured to be about 20photoelectrons/GeV by comparing with test beam results. The average attenuation length of scintillator is obtained to be120±10cm.

The test provided prompt control of the production quality.

Summary

The mapping measurements for the central electromagnetic calorimeter were performed with cosmic ray muons. The correspondence between cosmic ray and beam test results indicates that the mapping with cosmic ray muons is quite useful for a large number of calorimeter modules, except for the edge regions of the module.

The cosmic ray test is also capable of deducing some of the basic characteristics of hadron calorimeter to be consistent with those from the beam test.

Beam test

NW beam line

A schematic view of NW beam line at Fermilab where the beam test was done shown in Fig.[2.43].

800GeV/c proton beam hits an aluminum target to crate secondary particles mostly pions.

To get electron beam a sweeper magnet was turned on and an convertor made of lead was inserted . Neutral pions created in the aluminum target decays into photons immediately. Photons can survive in the magnetic field while charged particles were swept out. Photons were converted into electrons in the lead sheet.

On the other hand, pion beam can be got by turning off sweeper and removing the lead sheet. Neutral particles included in the pion beam went out from the beam line at the dipole bending magnet NW4. The other lead sheet NW6 absorbed electrons at the order of 10^{-2}

Momentum of each particle in the beam were measured by two beam chambers located either side of a dipole bending magnet called NW9E which bends particle at fixed angle of 28.587mrad.

Momentum spread for the electron beam of 50GeV/c is shown in Fig.[2.44]

The systematic error due to mismeasurement of the electron beam momentum was ±0.3% independent to the beam momentum. Source of this error were the error in the magnetic field measurements and the error in the beam chamber alignment.

Particles reach to the central module on a rotating table.It was designed to place up to two stacked wedges and endwall modules. It can rotate around a virtual collision point over full azimuthal and polar angle for the central module. It was driven by oil pressure equipments controlled by the on-line computer. The polar and azimuthal angles are measured by rotary encoders with 16bit precision for 360 degree read by the on-line computer. A 1/16" copper sheet with 2.5" thickness aluminum plate was placed in 7.5" front of the wedges to simulate the CDF superconducting solenoid. It has radiation length of 0.11 (copper) and 0.71 (aluminum).

The primary trigger signal were made by NIM logic using hodoscope signal at the beam line. The CDF prototype front end electronics sitting on the wedge scans signal and digitizes. CAMAC based system was used for interface between the front-end electronics and the on-line computer. The CAMAC interface system also control and monitor calibration system and rotation table.

A VAX-11/730 computer was employed for the on-line computer. Data were recorded on 6250bpi tapes. The on-line program called RUNCONTROL executes CAMAC interface , display histograms based on YHIST , manage data with YBOS and allows user to define , clear and display histograms. The last feature ease user to debug the system.

Electromagnetic calorimeter

Linearity

Energy response of the electromagnetic calorimeter were measured at the energy of 10, 15, 25, 37.5, 50 and 70GeV. Some cut with beam position as follows were applied for the analysis.

Z position : the center of the gravity of induced charge on the strip by electromagnetic shower. It was limited to ±2cm from the center of the tower.

Difference of Z position: Z position measured by the strip chamber and one reconstructed by the beam chambers at the depth of the strip chamber. If the difference was large, the particle was scattered in front of the camber. It was limited to ±0.7cm from the center value. The center value was not zero but about 1.5cm since the error of the wedge position measured by the rotary encoders.

X position: measured by the strip chamber. It was limited to ±1.6cm. The difference X limit and Z limit comes from the fact that the beam profile was not circular but an oval.

*Difference between X position:*measured by the strip chamber and the beam chambers. The limit was set to ±1.6cm.

2.5 sigma cut for Gaussian fit.

The output of the calorimeter is defined as sum of two photomultipliers of the each electromagnetic calorimeter. It was scaled to momentum of the incident particle measured by the beam chambers. Output from the hadron calorimeter was not used for this measurement.

Typical energy response is shown at Figs.[2.45] for each energy. Linearity of each energy is summarized in Figures [2.46a] - [2.46f] for towers 0 to 5. These value are scaled to the value at 50GeV since the calibration constants are based on the value at the 50GeV.

The scaled low energy response at the lower energy is smaller than 1 at the level of a few percent. An EGS type Monte-carlo electromagnetic shower simulation (Ref.[2.18]) was performed to explain the effect. The simulation took account the geometry of the test i.e. the solenoid simulator , aluminum bottom plate , scintillator and lead stack , strip chamber, WLS response map and Birks's law of dE/dx and light output of scintillator (Ref.[2.19]). The simulation was performed at the geometry of tower 3. In comparison to the real data the simulation did not match with it. -1.2±0.3% non- linearity at 10 GeV can be explained from the effects above, but maximum over 4% non-linearity cannot be explained.

Energy Resolution

The energy resolution of each tower is defined as sigma/mean of the gaussian fit on the distribution of sum of photomultiplier output scaled by incident particle momentum event by event. These are analyzed with the same cut as the linearity measurement except the 2.5 sigma cut. Energy resolution for the each tower for each energy are summarized at table [2.15].

As shown in Fig.[2.47] the energy resolution value increase with the tower number. This is caused by the thickness of the lead sheet viewed from the incident angle increases at the rate of 1./√sin(theta). Empirical relation predicts energy resolution of a sampling calorimeter (Ref.[2.20]) as

$$\frac{\sigma}{E} = R\sqrt{\frac{t\ (X_0)}{E\ (GeV)}},$$

where t is thickness of a radiator layer expressed in radiation length. In our case t=0.57 at the azimuthal angle = 90°. R is an empirical constant 14.8%. Thus the expected value for the central electromagnetic calorimeter is 11.2%/√sin(theta)

The resolution becomes much worse at the higher energy 50 GeV and 70GeV. This is because the electromagnetic shower leakage to the hadron calorimeter. As shown in Fig.[2.48] : scatter plot of energy deposit to EM vs hadron for 50GeV/c electron: energy leakage to the hadron calorimeter cannot be ignored at 50GeV. We tried two method to get a better resolution.

Cut the event in which energy deposit to hadron calorimeter greater than 2 GeV.

or

Add output of hadron calorimeter with a factor: a

Out =EM +a × HAD.

a is defined to minimize the sigma of Out.

The analysis was performed for the 50GeV electron to the each tower. Results is shown in table [2.16]. The 2GeV hadron cut have a better energy resolution but not 100% efficiency.

Response Map

5 modules were scanned by 50GeV electron beam to investigate their response maps. The turntable moved 4cm when the number of event was filled at the level of statistical error less than 1%. The diameter of the beam was 2.5cm at this measurement. Position of the incident electrons were measured by the strip chamber placed between 8th and 9th layer of the stack and its position resolution was 2mm.

The coordinate we use at this measurement is as same as for the cosmic ray test as shown in Fig.[2.5] The coordinate was defined on a strip chamber plane in cm. For the convenience we add the other coordinate system for each tower. We use z' for each tower system

instead of z of global coordinate. A wedge plane was divided into 1cm by 1cm cell. The measurement of the position is based on this cell.

Figure [2.49] shows a typical response map of a tower scanned by electron beam.

Sum of phototube response as a function of x

Most part of the tower except at the edge part the x-dependence of the sum of phototube response can be written as

$$S(x,z') = s(0,z')\cosh\left(\frac{x}{w(z')}\right).$$

Light attenuation in a scintillator can be described as exp(-x/L) if the reflection at the end of the scintillator can be ignored. But a fairly amount of light are reflected at the end of the scintillator. Thus the light output viewed at a edge of a scintillator can be written as; exp(-x/L) + k exp(-(length of scintillator - x)/L) where k is a reflection factor. It can be rewritten as exp(-x/L) + k' exp(x/L). It is rather a complex form.

We can write sum of light output from the both edge of scintillator as cosh form. The reflection factor is absorbed in the normalization factor S. And w=L.

Fig. [2.50] shows the typical response at the z'-center of a tower. The dashed line shows the fit by cosh curve , where w = 44.2cm.

We must point out the ratio of the both tube is a complex form mathematically but seems a straight line on semi-log plot it is shown at Fig.[2.51]. But the attenuation length taken from the fit of ratio plot cannot explain behavior of phototube output sum. (dot-dashed line in Fig.[2.50]).

And attenuation length viewed by a tube also cannot explain it. (dotted line in Fig.[2.50])

Shower leakage

The response due to the lateral profile of an electromagnetic shower into a non-active area can be written as a form of:

$$f(z') = \frac{\alpha}{1+\beta e^{-\gamma z'}},$$

if the lateral distribution of a shower can be written by a single exponential curve.

The geometrical configuration of the gap between wedge modules is shown in Fig.[2.52]. The beam test result and the fit by the above formulation is shown in Fig.[2.53]. The micro-structure at the gap of the modules; one can see wavelength shifter area and iron skin in it; was ignored.

Overall response map

The overall response map for a calorimeter is expressed by a form.

$$S(x,z') = F1 \times F2(z') \times F3(z') \times F4(x,z') \times F5(z'),$$

where

$$F1 = p_1,$$

$$F2 = \frac{1}{1+ p_2 \exp(p_3 |z'|)},$$

$$F3 = 1+ p_4 z' + p_5 z'^2,$$

$$F4 = \cosh\left(\frac{x}{w(z')}\right)(1+ p_8 z' + p_9 z'^2), \text{ with } w(0) = p_6 \times p_7$$

for $w(z')$

$$F5 = \frac{1}{1+p_{10} \exp[|x|(p_{11}+p_{12}|z'|)]}.$$

The parameter p_1 is an effective normalization factor and the value is close to 1.00

F2 fits the effect of leakage at z tower boundary.

F3 represents the non-uniformity in z' due to asymmetric function.

F4 express the light attenuation in scintillators.

F5 fits the effect of leakage at crack between the modules.

The parameters for each towers are summarized at table [2.17]. Typical fit results along z and x direction are shown in Fig.[2.54]. and Fig.[2.55] The fit for overall area is shown at Fig.[2.56].

Non Uniformity

The non-uniformity of the response is defined as the fractional difference of the response in each cell from the overall average. Figure [2.57] shows the distribution of the deviations in non-uniformity for all cells. The main peak is mainly consisting of the contributions from the central area. On the other hand, the higher side is from the region around z-tower boundaries and x-cracks. The non-uniformity in the overall area is 3.9% in RMS. The non-uniformity at z - boundaries and x- cracks increases typically to 5% and 7% respectively. The non- uniformity of tower 9 is about twice as large as that of other towers.

Similarity

We have observed similar characteristics in the raw response maps module -to - module and tower to tower.

The similarity for each tower cell is defined as the percentage deviation the response in each cell with respect to the average obtained from the 5 modules.

The distribution of overall deviations in similarity is shown in Fig.[2.58] The RMS deviation of the distribution is 0.8%. The similarity varies from 0.7 to 0.9% depending on the tower number. At the tower boundaries the similarity increases to 1.0%. The similarity at x-cracks ($|x| \geq 20$cm) is larger, being 1.8%.

The small RMS deviation in the similarity for all modules insures that a single response correction function can be used for all the 48 modules.

Reproducibility

The percentage deviation of responses from the average response function over 5 modules $\langle s(x,z') \rangle_5$ is denoted reproducibility. The reproducibility for the average response maps is 1.1% over the central region of $|x|<20$cm and $|z|<234$cm (84% of the entire region), and 1.5% over the entire region. The reproducibility ranges from 1,2% to 1.4% for towers 1-5 and 7. and 1.5-2% for the other towers. A histogram with dashed line in Fig.[2.59] is the distribution of deviations in reproducibility over the entire region. Solid line represents the entire region.

It should be noted that the reproducibility with respect to the simple response function form cosh(x/w) over the entire region is 2.4%. The distribution of the deviations of reproducibility in this case is shown in Fig.[2.60].

Errors associated with data reduction

The number of events accumulated in each cell varied from several to 100. The precision of the magnitude of light response at each cell is estimated to be 0.2 to 2.0 %, taking

into account the energy resolution of 2.0% at 50GeV. For mapping studies, a cut was applied to the cells with statistical errors larger than 1%.

The systematic error in making response naps was estimated from the comparison of the results of two different electron calibration runs made for 21 modules. The comparison indicates that the systematic error in making response maps is 0.36±0.13%.

We estimate the sources of systematic errors. The time variation of temperature during the measurement would affect to the gain variation of phototubes by 0.14%. The instability of high voltages might result in 0.12% error for gain of phototubes. As for the momentum tagging system, the uncertainty of magnetic fields was 0.2% and the uncertainty in determining the particle hit position was 0.1%. We may neglect the errors associated with electronic. The overall systematic error is estimated to be 0.3%. which is consistent with that obtained from the comparison of two different electron calibration runs.

Summary

5 module was measured their response map by 50GeV electron.

Overall non-uniformity of the raw data was 3.9% and the similarity was 0.8%.

Response function was expressed by 12 parameters. Overall reproducibility by the function is 1.7% for the entire region and 1.35 for the main region ($|x| \leq 20$cm and $|z|<234$cm; 84% of the entire region).

The inverse of the function was written on the database. At the analysis the output from towers are corrected with the function according to the incident point of the particle.

Hadron calorimeter

Linearity

The energy range of 10 to 150GeV pion beams were injected to the center of tower 4 of the calorimeter to measure the linearity and response of the calorimeter. Events were required as the primary interaction occurred at the hadron calorimeter i.e. no energy deposit greater than minimum bias in electromagnetic calorimeter was recorded. The peaks to each energy are shown in Fig.[2.61].

The shower leakage to the back expected at high energy and non-linearity at the low energy (Ref.[2.21]) cannot be visible at this plot.

In the actual collider run in 1987 , low energy response of hadron calorimeter was investigated by low momentum and isolated hadrons. The central tracking chamber has a momentum resolution of $\delta Pt/Pt = 0.3\%$ Pt thus it can measure momenta accurately at the range lower than 10GeV where the beam test could not covered.

The result is shown in Fig.[2.62]. It include not only data of collider run but also beam test results. The non-linearity less than 10GeV is significant.

The principle of the hadron calorimeter ; inelastic interactions of incident or secondary particles and nuclei of absorber; requires incident hadron momentum greater than 5GeV/c. Thus a particle its momentum less than 10GeV is out of range for hadron calorimetry. The low energy data is essential to measure jet energy because a jet includes low energy particles.

Energy resolution

Figs.[2.63] and [2.64] shows the pulse height distributions of central tower 1 and endwall tower 10 for 50GeV pion beam. The events are also selected as no energy deposit in EM calorimeter.

Fig.[2.65] shows the pulse height sum of hadron and electromagnetic calorimeters of tower 1. The particle included this figure interact both in electromagnetic calorimeter and hadron calorimeter.

The energy dependence of energy resolution of tower 1 to 5 of central calorimeter and of tower 10 of the endwall calorimeter is shown in Fig.[2.66] Energy resolution is defined as sigma/peak ratio and the events out of two sigma from the peak were rejected. And energy deposit in electromagnetic calorimeter at the level of minimum ionizing particle was required. The resolutions of towers 1 ,5 and 10 is on straight lines as a function of $1/\sqrt{E}$. For tower 1 and 5 the energy resolution is approximately expressed $70\%/\sqrt{E(GeV)}$. And the resolution increases when the sampling become thick. As energy increases the contribution from leakage is predominant: for instance, beyond 50GeV, the energy resolution in tower 5, which has a factor 1.4 coarser sampling but is a factor 1.4 longer, is better than in tower 1.

Time response

The time resolution of the sum of the photomultipliers of a central hadron calorimeter tower, measured with the pion beam and with cosmic rays, was found to be 1.5ns. The time dependence upon the pion position in a tower was also measured and found to be less than 0.5ns. The time dependence as a function of pulse height was also measured and to be corrected.

Response Map

A module was exposed pion beam for map measurement. At this measurement two modules were stacked. The other module that was not exposed was also read its output because the lateral size of a hadron shower is so large that the leakage to adjacent tower is not negligible.

Figure [2.67] shows a result of z-scan at x center of the tower. There is no z dependence except 10%dip at the tower boundaries since there are no scintillator but WLS there.

The shower leakage into polar adjacent tower is shown at Fig.[2.68] as a function of polar angle. It increases monotonically from 5% at 90° to 12% at 30°. The leakage into azimuthal adjacent tower was negligible.

The response as a function of x was examined. Fig.[2.69] shows ln(L/R) behavior as a function of x. The attenuation length from that graph was 164cm. The position resolution dependence to x is shown in Fig.[2.70].

Calorimeter response at azimuthal boundary of the module was investigated by pi and electron beam.

Fig.[2.71] shows a result of x scan by pion beam at z' center of a tower. One point on the graph corresponds to a beam size (~2cm at this measurement). No dip of the averaged response but large resolution was found at the module boundary. It indicates the existence of a combination of hot spot and dead area at the tower boundary.

The same scan was also performed by electron beam. A result with 50GeV beam is shown in Fig.[2.72]. Two large peak was observed. They are corresponds to light guide area. The mostly energy linear behavior (Fig.[2.73]) was caused by Cherenkov light in light guide caused by high energy electrons. The same effect can be seen by pion beam.

To prevent the hot spot , a radiator was put in front of the crack. It makes electromagnetic shower in it and scattered shower particles do not enter into light guide straightly. The effect of it is shown at Fig.[2.73] for different radiation length.

10 radiation length of ^{238}U crack fillers were placed at the crack area. In addition it cut by left/right ratio was applied to reject hot-spot output at off-line analysis. The energy resolution at crack area was found to be

$$\sigma(e) = 0.04 + 0.33\sqrt{E}$$

with the cut $0.6\text{-}3\sigma < L/R < 1/(0.6\text{-}3\sigma)$.

Tracking system

The VTPC (Vertex Time Projection Chamber) covers seven unit of rapidity and handle 30-35 charged particle tracks. The chamber provide r-z information using TDC data from sense wire signals. Information on the phi of tracks is obtained from cathode pad signals on a subset of chambers read out by a FADC (Flash Analog to Digital Convertor) system.

The main purpose of the VTPC in the analysis of jet is providing z-vertex determination. The colliding point of proton and antiproton in the Tevatron spreads in a gaussian distribution with a sigma of 35cm. The primary vertex position information is essential to calculate transverse energy deposited in each calorimeter cell in event by event.

The VTPC was constructed as low mass (short radiation length) since a photon interacting in the detector may create secondary charged particle and they fake other tracking detector. The VTPC was consistent of eight octagonal modules . A view of a module is shown at Fig.[2.74]. Each module has a central high voltage grid that divides it into two 15.25cm long drift regions. The length of drift space was designed as to have drift time less than 3.5μsecond at the drift velocity in the gas is 46μm/ns (argon-ethane 50/50 at 1 atm and E=320V/m). The electrons drift away from the center grid until they pass through a cathode grid and enter one of the two proportional chamber end caps. Each endcaps is divided into octants, with 24 sense wires and 24 cathode pads. The arrival times of electrons at sense wires were measured by Time to Digital Convertor to give a event picture in the r-z plane.

The vertex point was determined from the information of r-z plane. Essentially the observed tracks in r-z plane is a straight line except very low Pt particles since the axial magnetic field. The z- position resolution for a track near the sense wire is about 200μm , while the resolution for the longest drift time is 550μm. The impact parameter b of tracks with the primary vertex is defined by the following:

$$b = (z - z_{vertex}) \sin\theta.$$

Figure [2.75] shows a histogram of impact parameter of reconstructed wire tracks for a sample of events taken with a minimum trigger bias. The RMS distribution is about 0.3cm.

Data Acquisition System

Front-end electronics

The CDF detector has a total of approximately 100,000 channels of signals. The calorimetry requires a very large dynamic range from ,at least, minimum ionizing particle to a few hundred GeV in accuracy less than 1% in every energy region. A special crate based analog front-end system called RABBIT system was developed to deal with this problem. The RABBIT system consists of 129 crates mounted on the detector which service all of the calorimeter about 60,000 channels of 100,000 total. The signal from drift chambers are pulled out from the collision hall and brought to the counting room.

The front-end of RABBIT system is based on two sampling voltage level scheme. It samples a voltage that was converted from the charge output of calorimeter and hold it by integral circuit before a collision. Then after collision another voltage is sampled and hold . Then output of a calorimeter channel is defined as a difference of level of voltage. Sampling two level of voltage has advantages to avoid pile-up effect and common-mode noises. The timings of sampling and holding are based on the bunched structure of the beam. The Tevatron has three bunches of protons and antiprotons. Thus interactions occur at relatively well defined windows in time, separated by 7μsec.

Digitizing was performed in each crate by 16bit full scale ADC.

RABBIT crates are controlled and read out their output by fast intelligent scanner called MX's. It is a custom made computer designed to scanning data from RABBIT , subtract pedestal and multiply factor to convert digital value to charge very fast. The pedestal value and factors are loaded database on on-line computer MX's also provide threshold value , if the signal larger

than it RABBIT decide to start analog-to-digital conversion . MX's are interfaced to on-line computer through FASTBUT data acquisition system.

Trigger system

The CDF on-line triggering system were designed to take events every collision and decide to write events on magnetic tapes. It have up to four kind of triggers. In 1987 run events were triggered with unbiased , jet oriented calorimeter Et , large Pt electron oriented calorimeter Et and muons. For the jet analysis events triggered by calorimeter Et were used.

Both hadron and electromagnetic calorimeter towers are summed into trigger towers with a pseudo rapidity of $\Delta\eta = 0.2$ and width in phi of $\Delta\phi = 15°$. Thus the entire detector is divide into 42 (in η) and 24 (in ϕ) trigger towers.

Output from the all phototubes are brought to trigger system setting in the counter room by 60m combined twisted pair cables. All the gas calorimeter pad signals are summed at the detector into the trigger towers. The signals are analog DC levels (0-100GeV in Et is 0-1 volts) from the before and after sampling of beam crossings.

In the trigger system the signals are summed over four phototubes i.e. left and right tubes of two towers. The summed signal are weighted by sinθ by an analog *weight and sum* circuit to represent the transverse energy Et. The voltage stay on these trigger cables until a Level 1 decision is made: if the Level 1 requirement is not satisfied in a given crossing, a reset signal is automatically issued in time for the next beam crossing. No dead time is introduced by events which do not pass level 1.

The Level 1 calorimeter triggers require that the sum of Et for all calorimeter towers which are individually over a lower threshold (typically 1GeV) be greater than a higher threshold (typically 30-40GeV). The threshold for the Et sum was varied according to luminosity of each run. The threshold are programmable.

Chapter 3
Data analysis

Luminosity

The rate of events is determined by the product of luminosity;L and cross section; σ as,

$$dN/dt = L\sigma.$$

Thus, if we have dN events of jets at a range of Pt < Pt < Pt +dPt at a given integrated luminosity $L = \int Ldt$ the differential cross section is given by

$$d\sigma/dP_t = dN/L.$$

In the CDF collider run , L of each run was measured with *assumed* inelastic cross section σ (inelastic) and number of events that hit west and east beam beam counters (BBC) simultaneously.

$$L = N \text{ (hit W·E BBC) } / \sigma \text{ (inelastic) } \times \varepsilon \text{ (acceptance of BBC)}$$

Number of hit to BBC was counted by a scalar in every run. The value of σ (inelastic) × ε (acceptance of BBC) was estimated as follows.

Total cross section of the proton and antiproton collision at $\sqrt{s}$=1800GeV can be extracted from the low energy data. Recent paper predicts $\log^2 s$ behavior of the total cross section. According to Block and Cahn (Ref.[3.1]), a smaller value is arrived by extrapolating from the lower energy data and assuming that the cross section is asymptotically constant at very high energies but locally proportional to $\log^2 s$, while the larger value results from assuming the cross section to continue to evolve proportionally to $\log^2 s$. The former assumption predicts 74mb, while the latter 80 mb at $\sqrt{s}$=1800GeV. Thus the total cross section can be assumed as

$$\sigma_{tot} = 77 \pm 6 \text{ mb.}$$

The ratio of the total and the elastic cross sections was measured by UA4 group at $\sqrt{s}$=546GeV (Ref.[3.2]) as

$$\sigma_{elastic}/\sigma_{tot} = 0.215 \pm 0.005.$$

This value varies very slowly with $\sqrt{s}$, hence we assume

$$\sigma_{elastic}/\sigma_{tot} = 0.229 \pm 0.01,$$

at $\sqrt{s}$=1800GeV.

Thus

$$\sigma_{elastic} = 17.6 \pm 1.6 \text{ mb,}$$
$$\sigma_{inelastic} = \sigma_{elastic} \cdot \sigma_{tot} = 59.4 \pm 4.7 \text{ mb.}$$

The inelastic cross section can be broken up into three components; the hard core cross section, σ_o, the single diffractive cross section σ_{sd} and the double diffractive σ_{dd}. We calculate σ_{sd} and σ_{dd} based on a result of UA5 group (Ref.[3.3]).

σ_{sd} =15.0 ±5.0mb,

σ_{dd} = 4.2 ±1.0mb.

And we obtain

$$\sigma_o = \sigma_{inelastic} - \sigma_{dd} - \sigma_{sd} = 40.2 \pm 6.9 \text{ mb}.$$

Finally, acceptance of the BBC for each process was calculated by a Monte-carlo simulation and $\sigma_{BBC} = \sigma(\text{inelastic}) \times \varepsilon$ (acceptance of BBC) is obtained as

$$\sigma_{BBC} = 0.134\,\sigma_{sd} + 0.618\,\sigma_{dd} + 0.942\,\sigma_o = 42.5 \pm 6.0 \text{mb}.$$

Data set

A total Et trigger was determined by the sum of the transverse energy Et over the trigger towers with Et > 1GeV. Event were triggered in the case of the either of the following quantities were greater than the threshold, ΣCEM, ΣCEM+ΣCHA, ΣCHA, ΣPEM or ΣFEM . The thresholds for total Et sum were set to 20,30,40 or 45GeV depending on the luminosity. The integrated luminosities of the runs for this analysis were 0.165 , 12.0 , 6.80 and 4.74nb^{-1} corresponding to the threshold values of 20,30,40 and 45 GeV respectively. The trigger conditions are summarized in table [3-1].

An electron trigger was formed using the sum of of Et's deposited in the central electromagnetic calorimeter, selecting only those towers that had Et above 5 to 12GeV. The total Et threshold was set to 7 to 15GeV depending on the luminosity.

A high Pt muon trigger was made by a track processor associated with the central and forward muon chambers.

A minimum bias trigger was formed from the coincidence between the west and the east beam-beam counters. This coincidence was also required for the three modes of calorimetric trigger mentioned above.

The data logging rate was kept to about 1Hz and the number of jet events per tape was about 300. The total number of raw data tapes amounted to about 500.

Definition of a Jet

Clustering algorithm

As shown in Figure [3-1] , one can find clear shapes of clusters on the η–ϕ plane. Thus we did not define jet with a statistical value like *planarity* as used for fixed target experiments and at the ISR. At Tevatron energy jet can be defined as a cluster on a calorimeter η–ϕ plane.

A clustering algorithm JETCLU was used in the present analysis. In this algorithm we call towers with Et above 1.0 GeV as seed towers and those with Et above 0.1 GeV as candidate towers.

After the seeds and candidate towers have been found, preclusters are formed. Preclusters are by definition a chain of adjacent towers with a continuously decreasing tower Et. Clustering is performed with the preclusters with Et above 2 GeV. A fixed cone in $\eta - \phi$ space of radius 1.0 is formed around the precluster centroid calculated with the Et weight. Candidate towers inside this cone are merged into the cluster. A new centroid is calculated from

this new set of towers, and again all candidate towers inside the cone are merged in. The process of recomputing a centroid and finding new or deleting old towers is iterated until the tower list remains unchanged. For the overlapping clusters, if the overlap Et is larger than 0.5 times the Et of the smaller cluster, the two clusters are merged. Otherwise, the overlapping towers are divided into the two clusters.

Geometrical region

We analyzed only jets in the pseudorapidity range $0.1 < |\eta| < 0.7$ to avoid jets with energy lost in the cracks of the detector at 90 degree (central arch and arch) and 30degree (plug and central).

The z - coordinate of collision points were obtained by the VTPC and the pseudorapidity of the each calorimeter tower was corrected with the position of vertex for each event. The z-vertex point spreads to 35cm in R.M.S. as seen in Fig.[3-2]. Events with the absolute position of its vertex exceed 50cm were rejected , because the incident angles of these particles are different from the angle taken at the beam calibration.

We call the pseudorapidity without z - vertex correction as the *detector pseudorapidity* η_D. The detector pseudorapidity $0.1<|\eta_D|<0.7$ was also required for jets to avoid energy loss in the 90 and 30 degree cracks.

Pt of Jet

Et of a jet is defined as $Et = \Sigma E_i \sin\theta_i$. Here E_i means energy deposited in each tower included in a jet and $\sin\theta_i$ is a polar angle of the i-th tower center.

Pt of a jet is distinguished from Et , defined as $P_t = \sqrt{E_t^2 - m_{jet}^2}$: m_{jet} is an invariant mass of a jet calculated assuming a tower included in a jet as a massless particle. The Pt of jet and cluster are compared in this section.

Noise Filter

In the actual experiment , signals originated from the other sources can be merged in the real signal of proton and antiproton collisions. They are taken as *noises* . To suppress them we made a set of cuts to the calorimeter signals.

Cosmic ray and main ring noise suppression

Cosmic rays can make cascade showers inside a calorimeter. They deposit large energy in a calorimeter. This kind of noise is common in collider experiments.

The main ring was running during the collider run to provide antiprotons to the accumulator. High energy particle splash which came from the collision of proton and gas molecules or proton and the beam-pipe made noise to the calorimeter especially on the top of the detector.

Though these noises have different sources , we applied the same noise suppression in off-line analysis. These noises have common features, they are

1) not synchronized with the proton-antiproton collision
2) mostly hadronic .

Fig. [3-3] shows electromagnetic energy fraction in a cluster. There is a large peak around zero which mean abnormal hadron-rich clusters.

We requite by using hadron TDC for the hadron signal to be in the 35ns window within the 700ns gate of the beam crossing.We can reduce these noises by factor of 20. One can see its effect in the figure . The peak has been vanished.

In addition to the cut , we cut hadron-rich clusters by applying (Electromagnetic energy / Total Energy) > 0.1, and avoided noise entering within 35ns window. This cut also drop 1 ± 0.5 % of normal clusters. Acceptance correction described in the following section take s it account.

Single PMT suppression

Large spike noises from the photomultipliers of the central electromagnetic calorimeter were observed. They constituted large signal so that the events were triggered and data were written onto the tape. They were caused by discharge between cathode of photomultiplier and the material that wrap phototubes. We could eliminate these signals in the off-line analysis. We ignored such a tower in which one phototube had output greater than 2GeV while the opposite one had smaller than 0.1 GeV.

Energy and Acceptance/Energy Resolution correction for jet

The inclusive parton cross section has been calculated in the framework of perturbative QCD with tree diagrams. We have to know Pt of scattered partons from the Et of observed cluster to compare the theoretical calculation cross section with the experimental result .

We applied corrections to cluster cross section to compare them with theoretical predicted cross section.

To obtain a relationship between Pt of a parton and Pt of the corresponding cluster, we tried two independent methods. One is Monte-carlo and the other is the study of π^0 / γ +jet events.

Monte-carlo simulation take account all physics processes that occur to a scattered parton until it is observed as cluster(s). Thus one can correlate Pt of a parton with Pt of the cluster.

In addition to the Monte-carlo simulation , a study of Et balance in the π^0/ γ +jet events supports the Pt correction factor for jets, because we know the response of the electromagnetic calorimeter better.

We must also take account of the efficiency of on-line trigger system for events.

General form of the correction can be written as

$$P_t^{corrected} = F\,(P_t^{cluster}\,,\,\eta)\,,$$

$$\left[\frac{d\,N^{corr.}}{d\,P_t^{corr.}}\right]_{P_t = P_t^0} = \frac{1}{\varepsilon(P_t^0)}\,\frac{1}{A\,(P_t^0,\,\eta)}\,\frac{dN}{dP_t}\,,$$

where Pt of clusters are corrected as a function of Pt and its eta position.

Number of the cluster is corrected with the acceptance and the trigger efficiency.

These correction factors were calculated by comparing partons in the Monte-carlo event generator and Clusters observed in the event simulation program.

Definition for a parton

Here we have to define a *parton* in Monte-carlo event generator.

In the QCD hard parton parton collisions, contributions from the higher order processes cannot be ignored. Partons scattered in the lowest order QCD process radiate other

gluons and the gluons make other partons. This is the next-order process and called a parton shower. The probability of this process should be calculated with the proper QCD diagram including higher order radiation. However, this calculation is far more difficult than for the lowest order calculation. This parton shower processes is added by the leading log approximation (LLA) in the Monte-carlo simulation we used.

A radiated parton may produce another distinct jet if it has a large transverse momentum to the parent parton or it may fragment into particles which cannot be distinguished from a jet of the parent parton. We combine partons in R<0.7 cone drawn from the parent parton and call it as a parton cluster[1]. In the following, we will call a parton cluster produced in the Monte-carlo event generator simply as a *parton*.

Correction of jet Pt.

Pt of scattered partons is not exactly equal to Et of the observed clusters by following reasons.

Crack of the calorimeter and leakage

[1]**Special feature of ISAJET about the enrgy momentum conservation.**
The sum of energy of fragmented particles is not equal to the energy of the parent parton in ISAJET event generator program. This is because in the program the energy and momentum are conserved in the event as a whole. Thus it is reasonable to define the parton momentum by the sum of momentum of final fragmented particles, and not by the momentum of the parton itself.

2% of the area of the central electromagnetic, and 4% of the central hadron calorimeters are the dead region , because of the support structure. A central calorimeter module contains non- active regions of light guides and skins of the wedge structure at every 15 degree of the azimuthal angle.

The hadron calorimeter does not have enough absorption length to contain full of hadronic showers. Thus a fraction of hadronic shower leaks from the hadron calorimeter . This effect should be corrected statistically by a proper hadronic shower simulation.

Clustering performance

The clustering algorithm we use may miss energy deposition because some fragmented particle may go far away from the center of the cluster. Clustering performance to the cluster energy has been examined by a Monte-carlo simulation.

Non-linearity of calorimeter

As shown in section [2], the non-linearity of hadron calorimeter for low momentum particles has been observed in the collision data using the central tracking chamber.

Dominant amount of energy of jet is generally carried by low energy particles. Fig. [3.4] shows PdN/dP of particles in a jet. One can see 55% of 100GeV Et jet energy are carried by particles with momentum less than 5 GeV/c for which calorimeter response is less than 70%.

Thus the non-linearity effect affects the energy measurement of jet.

Magnetic field

Low energy charged particles are bent by the magnetic field inside the solenoid. They can escape from the cluster because of bending.

Neutrino and muon

Neutrino and muons are produced by weak decay of hadrons. They carry a fraction of the jet energy . We lose their energy, because their energy cannot be measured by a calorimeter.

The "underlying" particles

We call particles fragmented from those partons which do not contribute hard scattering as "underlying" particles. These particles are scattered independently from the hard jet and overlap them in the jet cluster region. Namely the cluster algorithm includes them in a jet.

Jet momentum correction by Monte-Carlo simulation

A Monte-carlo study was done to get a relation between Pt (Et) of the scattered hard partons with that of the observed clusters. It generates particles according to theoretical calculation. Two kinds of Monte-carlo particle generators have been used for our calculation. One is called ISAJET (Ref.[3.4]) and the other is LUND (Ref.[3.5]). The CDF detector simulation program simulates detector response for generated particles. Calorimeter responses are based on the parametrization of the results of the beam test.

The correction factor thus obtained inherits the ambiguity from the Monte-carlo. To check these results independently, π^0/γ + jet events were examined by assuming Et balance.

A relation of the Pt of a cluster and that of a parton was obtained by following steps.

Two jet events were generated with ISAJET 5.20 and simulated with the CDF detector simulation (Ref.[3.6]) program. We generated partons which have Pt from 30 ± 2.5 GeV/c to 100 ±2.5 GeV/c by 10GeV/c step and from 125±5 GeV/c to 250±5GeV/c by 25 GeV/c step in the range of $|\eta|<1$. 500 partons were selected in each Pt range.

The clustering algorithm was applied to these events. A cluster was assumed to originate from a parton, in the event generation, which is the nearest to the cluster in η–ϕ plane.

The ratio of Pt of the parton to the Pt of the corresponding cluster was accumulated. The distributions were fitted to Gaussian forms each Pt points. Typical distribution of the ratio is shown in Fig.[3-5].

The product of the ratio and mean value of parton Pt i.e. cluster Pt plotted against the mean value of the parton Pt in Fig. [3-6].

A straight line fit to the plot of Pt^{Parton} vs $Pt^{Cluster}$ in 30 GeV/c < Pt^{Parton} < 250 GeV/c gives

$$Pt^{Parton}(GeV/c) = 1.100\pm0.001 Pt^{Cluster}(GeV/c) + 5.2\pm0.1\ GeV/c$$

$$\chi^2/DOF = 23.3$$

Next we divided the Pt region into two parts and applied a straight line fit or quadrature function fit to each region. The function and the region were selected to minimize the reduced χ^2. The reduced χ^2 of each fit in each region and the fit parameters are shown in table [3.2]. We obtained the best fit by dividing the data set into two, one set is 30 GeV/c < Pt^{Parton} < 100 GeV/c and the other is 125 GeV/c < Pt^{Parton} < 250 GeV/c , and by fitting each of them to a

straight line. Two fit lines cross at the point of $Pt^{Cluster}$ = 84.5GeV/c (Pt^{Parton} = 100 GeV/c) . The straight line fits give

$Pt^{Parton}(GeV/c) = 1.148\pm0.003 Pt^{Cluster}(GeV/c) + 3.2\pm0.1\ GeV/c$

$\chi^2/DOF=14.2$ for $30\ GeV/c < Pt^{Parton} < 100\ GeV/c$

$Pt^{Parton}(GeV/c) = 1.064\pm0.004\ Pt^{cluster}(GeV/c) + 10.3\pm0.6 GeV/c$

$\chi^2/DOF= 2.2$ for $125\ GeV/c < Pt^{Parton} < 250\ GeV/c$

The inconsistency of the fit parameters in the two regions were caused by the non-linearity of the calorimeter response. This effect will be explained later.

We divide 30 GeV/c < Pt^{Parton} < 250 GeV/c region into two. Straight line fits or quadrature function fits were applied to each region. The function and the region were selected to minimize the reduced χ^2 ; χ^2/(degree of freedom).

In table [3-2] the reduced χ^2 of each fit on each region are shown. For the smallest χ^2/DOF, we divide data set into two, one set is 30 GeV/c < Pt^{Parton} < 100 GeV/c and the other is 125 GeV/c < Pt^{Parton} < 250 GeV/c. The fit parameters have been shown in above. Two fit lines cross at the point of $Pt^{cluster}$ = 84.5GeV which corresponds to Pt^{Parton} = 100.3 GeV/c. The data points and the best fit are shown in Fig.[3-6].

Fit with LUND type generation

The above procedure was also performed with PYTHIA4.60/LUND. The best fit for a plot of the parton Pt versus the cluster Pt was

$Pt^{Parton}(GeV/c) = 1.098\pm0.005\ Pt^{cluster}(GeV/c) + 5.5\pm0.3\ GeV/c$

$\chi^2/DOF= 3.3$ for $Pt^{Parton} < 125 GeV/c$

$Pt^{Parton}(GeV/c) = 1.008\pm0.005\ Pt^{cluster}(GeV/c) + 19.1\pm10.0 GeV/c$

$\chi^2/DOF= 2.7$ for $Pt^{Parton} > 125 GeV/c$

Two fit lines cross at the point of $Pt^{Cluster}$ = 151.1GeV/c (Pt^{Parton} = 171.4 GeV/c).

These lines are compared with the result from ISAJET in Fig.[3-7]. As seen in this figure, there is no difference which is greater than the jet energy resolution (~100%/√Et (GeV)) at any point less than 250GeV/c. Thus we conclude that we choose parameter from the ISAJET simulation.

Decomposition of Jet energy correction

Following special simulations were performed to decompose into elements which contribute to distortion of parton Pt. All of these simulations were based on the only particles which come from a hard scattered parton.

DATA SET 1(magnetic field + cracks)

Simulation was done without non-linearity of the calorimeter and analysis by window clustering algorithm with large radius(R=3). We see the effect of the detector crack and the leakage from the calorimeter. The result is free from the performance of the clustering algorithm. The magnetic field of 1.5T was applied in the simulation.

The straight line fit gives

$Pt^{Parton}(GeV/c) = 1.072\pm0.003\ Pt^{cluster}(GeV/c) + 2.0\pm0.1 GeV/c$

$\chi^2/DOF= 2.9$ (for $25 < Pt^{parton} < 100 GeV/c$)

$Pt^{Parton}(GeV/c) = 1.069\pm0.002\ Pt^{cluster}(GeV/c) + 2.3\pm0.1 GeV/c$

χ^2 /DOF= 2.0 (for $25<Pt^{parton}<250 GeV/c$)

DATA SET 2 (magnetic field + cracks + non-linearity)

Data were produced assuming, non - linearity and were analyzed by window clustering algorithm with large radius (=3.) We can see the effect of the non-linearity comparing with the result with at for set 1. The magnetic field was applied in the simulation.

The result is

$Pt^{Parton}(GeV/c) = 1.170\pm0.003\ Pt^{cluster}(GeV/c) + 4.6\pm0.2 GeV/c$

χ^2 /DOF= 15.0 (for $25<Pt^{parton}<100 GeV/c$)

$Pt^{Parton}(GeV/c) = 1.119\pm0.001\ Pt^{cluster}(GeV/c) + 6.4\pm0.1 GeV/c$

χ^2 /DOF= 40.8 (for $25<Pt^{parton}<250 GeV/c$)

One can see the different fitting parameters of each Pt region and large χ^2 , comparing data set 1. The difference from straight lines was clearly caused by the non linearity of the calorimeter.

DATA SET 3 (magnetic field + cracks + non-linearity + clustering)

Data were produced assuming non-linearity, and were analyzed by the standard clustering algorithm (JETCLU). We can see the performance of the clustering algorithm. This is the correction factor without the underlying events. The magnetic field was applied in the simulation.

The result is

$Pt^{Parton}(GeV/c) = 1.170\pm0.003\ Pt^{cluster}(GeV/c) + 4.8\pm0.2 GeV/c$

χ^2 /DOF= 17.5 (for $25<Pt^{parton}<100 GeV/c$)

$Pt^{Parton}(GeV/c) = 1.120\pm0.001\ Pt^{cluster}(GeV/c) + 6.4\pm0.1 GeV/c$

χ^2 /DOF= 39.1 (for $25<Pt^{parton}<250 GeV/c$)

DATA SET 4 (cracks + non-linearity + clustering)

The difference in conditions to those of data set 3 is that no magnetic field was applied to see the effect of the magnetic field to see the effect of the magnetic field.

No change was found greater than 1% in each energy range. We can conclude the magnetic field does not affect the jet Pt correction above the 1% level.

Summarizing these result for Pt^{parton} < 100 GeV/c,

$Pt^{Parton}(GeV/c) = 1.072\pm0.003\ Pt^{cluster}(GeV/c) + 2.0\pm0.1 GeV/c$

for magnetic field + crack

$Pt^{Parton}(GeV/c) = 1.170\pm0.003\ Pt^{cluster}(GeV/c) + 4.6\pm0.2 GeV/c$

for magnetic field + crack + non-linearity

$Pt^{Parton}(GeV/c) = 1.170\pm0.003\ Pt^{cluster}(GeV/c) + 4.8\pm0.2 GeV/c$

for magnetic field + crack + non-linearity + clustering

$Pt^{Parton}(GeV/c) = 1.148\pm0.003 Pt^{cluster}\ (GeV/c) + 3.2\pm0.1\ GeV/c$

for magnetic field + crack + non-linearity + clustering + underlying events

The effects of the underlying events were calculated by comparing the result of data set 3 and of simulation including not only hard scatterd particles but all the particles..

π^0 / γ event

As an indirect but sensible check of the relation of Pt of the cluster to Pt of the parton as obtained above , we studied the transverse energy balance in observed π^0 / γ + Jet events.

A prompt photon events are predicted by QCD. A photon instead of a gluon can be radiated at the lowest order QCD process. In these events, a high transverse momentum photon is observed with a jet in the opposite side of transverse plane balancing their Pt. Energy of the high energy photon can be measured by the electromagnetic calorimeter precisely and it can be a *Pt measure* for the jet in the opposite side.

In the standard QCD jet events , a scattered parton sometimes fragment into a very few number of hadrons . For example a high energy π^0 can carry most of the energy of the parton. In this case, one can not distinguish such a event from a prompt γ event unless the separation of a single γ from π^0 is well established.

The cross section for the prompt γ events are estimated to be smaller than that for the two jet events by an order of four. This difference comes from the difference of coupling constants of strong and electromagnetic constants , lower mean charge of partons inside proton (antiproton) and lower density of quarks than that of gluons which are dominant source of parton-parton scattering in this Pt region. The UA2 reported (ref. [3.7]) the cross section of these events to be 10^{-4} of the two jet events. The cross section for the π^0 events were greater than that for the prompt γ events by a factor of 6 at Pt = 20GeV/c.

Although the study of π^0 / γ + Jet events cannot establish the calibration constant by itself because of the low statistics , it is useful to check the calibration constant determined from the Monte–carlo study.

The data were extracted from the data summary tapes which were produced for electron finding. The data summary tapes contain events triggered by electron trigger and the jet trigger. They require a electromagnetic cluster of which the ratio of hadronic to electromagnetic was less than 0.1. Clusters which had no associated tracks were passed if they had Et greater than 15GeV. In total 5.9×10^4 events were contained in 134 reels of the data summary tapes.

The electron trigger of level 1 required at least one electromagnetic trigger tower has Et deposit greater than 12 - 15GeV. These threshold values were varied with the luminosity to keep a constant rate of the data taking. An electromagnetic cluster in the electron data summary tape was defined as one tower and two adjacent tower in rapidity. It is different from the jet algorithm.

The track reconstruction was performed only in the area azimuthally close to a cluster by 15° with the central tracking chamber (CTC).

The π^0 / γ + Jet events were selected on the basis of the following requirements:

a). There is at least one cluster which have $Et^{uncorrected}$>15GeV or $Et^{corrected}$ >15GeV, Et(hadron)/Et(electromagnetic) < 0.05 and isolation <0.1 in the central calorimeter region.

Not only Et which was corrected by the map of the central electromagnetic calorimeter, but also uncorrected Et was included this data set.

Isolation is defined as the ratio of the Et of the electromagnetic cluster to the sum of remained Et around the electromagnetic cluster in R<0.7 region.

$$Isolation \equiv \frac{\sum_{R<0.7} E_t \; - \; E_t^{electromagnetic\ cluster}}{E_t^{electromagnetic\ cluster}} .$$

The number of events was reduced to 3112 events by cuts described above.

b).There are two clusters with Et above 10GeV in the range range $0<|\eta|<1$ including a electromagnetic cluster and no other clusters with Et above 10GeV for $0<|\eta|<4.2$.

c). The azimuthal angle difference between the two clusters is in the range between 160 and 200 degrees (Back to back).

The number of events was reduced to 183 events by cuts described above.

d). No track pointed to the electromagnetic cluster.

The number of events was reduced to 110 events by cuts described above.

Hereafter, the Et of the electromagnetic cluster is corrected by the response map of the central electromagnetic cluster.

The distribution of difference of azimuthal angle between electromagnetic and non-electromagnetic clusters is shown in Fig.[3-8]. The ratio of Et of electromagnetic cluster to the Et defined by the jet algorithm is shown in Fig.[3-9].

The Pt distribution of the π^0 / γ cluster is thus identified shown in Fig. [3–10] together with PYTHIA4.60/LUND simulation results for the direct photon process. It shows that 50% of these events come from the direct photon process. The remaining events come from the two jet process.

Pt of the π^0 / γ cluster Pt is plotted against the Pt of the other cluster (away jet) in fig.[3.11a].

Fitting was applied at electromagnetic cluster Et (corrected by response map) greater than 15 GeV. Five events were rejected because these events had clusters uncorrected

We binned Pt of π^0 / γ clusters in every 3.5 GeV and for each Pt bin fitted Pt distribution of the away jet to a Gausslan form for each bins. The mean value and R.M.S. of each distribution were also calculated. The value of sigma of the Gaussian fit and the R.M.S. of the distribution were compared. We took the smaller one for the distribution of the each bin. The energy resolutions of the away jets were found to be approximately 100%/$\sqrt{}$Pt(GeV/c). For bins which contained only one event, this error value was applied.

The Pt of the π^0 / γ , the mean Pt of the away jet and its error, the energy resolution of the away jets and number of events are shown in table [3–3]. The mean value of Pt of the away jet and its error are shown as a function of Pt of π^0 / γ clusters in Fig. [3–11b]. A straight line fit gives

$$Pt^{\gamma}\ (GeV/c) = 1.16 \pm 0.11\ Pt^{cluster} + 3.0 \pm 2.4\ GeV/c$$

Two lines are also shown corresponding to equations (1) (ISAJET fit) and (2) (LUND fit). These are compared with the data points in Fig.[3–11b] for ISAJET and LUND. The deviation of the two lines from the data points can be used as a measure of the uncertainty in this equation for energy correction.

Reduced $\chi 2$ of the deviation of the two lines from the data points are

$\chi 2$/DOF =0.83 for ISAJET

$\chi 2$/DOF =1.05 for LUND

where DOF =9.

The jet energy correction is consistent with the data points for π^0 / γ + jet events within statistical errors.

Correction for acceptance and energy resolution

Hardware trigger efficiency

During the CDF data taking, four kind of trigger conditions were mainly applied –they are named *Low* , *medium* ,*high* and *Burn*. The hardware trigger called Level 1 which makes decision based only on the sum of transverse energy, ΣEt, of each calorimeter cell was used. The threshold values were chosen to keep data taking rate to ~1Hz at every accelerator luminosity condition. The threshold conditions are summarized in Table [3–1] .

ΣEt's of the central electromagnetic , central hadron , wall hadron plug electromagnetic and forward electromagnetic calorimeters were used for triggers. The plug and forward hadron calorimeters were not used because of their noises. To correct their absence from the trigger system , threshold for the electromagnetic calorimeter in these region were adjusted to have equal trigger rate to the central region.

The trigger efficiency ε_t (Pt, η) was estimated using the CDF detector and trigger simulation program. It is defined by

$$\varepsilon_t(P_t, \eta) = n_1(P_t, \eta) / n_0(P_t, \eta),$$

where n_0 (Pt, η) is the number of all generated events in which the leading jet has a transverse momentum *Pt* at a pseudorapidity η , and n_1 (Pt, η) is the number of events which passed the hardware trigger conditions described in chapter 2. The trigger efficiency ε_t (Pt, η) was averaged over $0.1 < |\eta| < 0.7$ to obtain ε_t (Pt). The trigger efficiency ε_t (Pt) is plotted as a function of leading jet Pt for the hardware trigger thresholds of 20, 30, 40 and 45 GeV in Fig.[3–12]. In the offline analysis, we applied a leading jet Pt threshold of 50 GeV/c with a trigger efficiency larger than 99.5 %. This trigger efficiency is consistent with that obtained from comparison of the inclusive jet cross sections for different hardware trigger thresholds [3-8].

The simulation program is consistent with the experiment in that the Et of trigger system is not corrected by the z position of vertex, but it does not include additional fluctuations caused by the trigger system; noise and inaccuracy of the threshold of the *weight and sum* module. These effect are negligibly small because we accept in analysis only events whose trigger efficiency are greater than 99.5%. Other larger sources contribute to the error of inclusive jet cross section.

Geometrical and software cut acceptance

Though the CDF detector covers most part of 4π radian surrounding the collision point , we accept jets limited in position on the detector, $0.1<|\eta_D|<0.7$, to avoid effects of cracks and boundaries. The geometrical acceptance was calculated by simulation since all the jets centered in $0.1<|\eta|<0.7$ cannot be detected.

We also cut events by the electromagnetic fraction and z- position of vertex.

Calorimeter energy resolution affects the jet cross section. The observed Pt of a cluster sometimes may be higher than the real Pt of the jet because of the calorimeter resolution. This *leakage from lower Pt jets* makes the cross section at higher Pt larger. The inclusive jet cross section generally falls down very steeply , thus the small amount of leakage from lower Pt region gives substantial change to the cross section at higher energy.

These effects to the cross section were investigated with a Monte-carlo simulation.

The correction factor $\varepsilon(Pt, \eta)$ for geometrical acceptance, analysis cut acceptance and energy resolution was estimated by

$$\varepsilon(P_t, \eta) = N_2(P_t, \eta) / N_1(P_t, \eta),$$

where $N_1(Pt, \eta)$ is the number of partons with a transverse momentum Pt at a pseudorapidity h and $N_2(Pt, \eta)$ is the number of jets with a transverse momentum Pt at a

pseudorapidity h which passed the EM fraction cut , the z vertex cut and the detector pseudorapidity η_D cut .

Lund-type Monte-carlo events were generated to obtain the correction. In the real analysis ε was calculated in a 20 GeV Pt range. To get an acceptance correction factor at a given Pt range events which have lower Pt must be generated, because of the *leakage from lower Pt jets* has to be estimated. We take the energy resolution of jets as $\sigma E = 100\%/\sqrt{E(GeV)}$ which is approximately equal to the resolution of central hadron calorimeter. The leakage of events with every within 2 standard deviation were taken into account.

The correction factor is shown for various Pt's as a function of η in Fig.[3-13] and the correction factor after integrated over the η range $0.1 < |\eta| < 0.7$, $\int \varepsilon (Pt, \eta) d\eta$ is shown as a function of Pt in Fig.[3-14]. It is fitted to a quadratic function and used for calculation of the inclusive jet production cross section. It is 0.87 almost independently of Pt for the Pt's above 50 GeV/c. The contribution to this correction factor, $\int \varepsilon (Pt, \eta) d\eta$, are resolved as follows:

EM fraction cut	-1 % ± 0.5 %
z vertex cut	-14 % ± 2 %
geometrical acceptance	-12 % ± 4 %
energy resolution	14 % ± 7 %

The systematic error in $\int \varepsilon (Pt, \eta) d\eta$ is estimated to be 10 % by adding the above errors in quadrature.

Chapter 4
Results and Comparison with Theoretical Calculation

Inclusive jet cross section

The inclusive jet cross section is calculated by

$$\frac{1}{1.2}\int_{0.1<|\eta|<0.7} \frac{d\sigma}{dp_t\, d\eta} d\eta = \frac{1}{1.2\Delta p_t} \sum_{0.1<|\eta|<0.7} \sum_{p_t^0=p_t-\Delta p_t/2}^{p_t^0=p_t+\Delta p_t/2} \frac{N(p_t^0,\eta)}{\int Ldt} \frac{1}{\varepsilon(p_t^0,\eta)}$$

where $N(p_t^0, \eta)$ is the number of jets with transverse momentum p_t^0 at a pseudorapidity η. $\int L\, dt$ is the integrated luminosity, and 23.6±3.5 nb^{-1} for the jet events. This inclusive cross section is shown in Fig.[4-1] and tabulated in Table [4-1].

Systematic error

The systematic error of the inclusive jet cross section is caused by two sources, one is formed by the error of jet energy correction, the other is formed by efficiency ; trigger efficiency , geometrical acceptance , efficiency of cuts in analysis and.effect of energy resolution of calorimetry.

Jet energy scale

Each tower of the calorimeter has a systematic error caused by the absolute calibration and non-uniformity of mapping. These effects were not taken into account in the Monte-carlo simulation except for the crack response.

The absolute calibration value is reliable within 1% level as mentioned in the previous section. Jet particle spreads over 5-6 towers in average. The error in the absolute energy calibration for a jet is reduced to $1\%/\sqrt{5}$-$\sqrt{6}$ since the calibration constant fluctuates from tower to tower independently.

A parton fragments into a number of particles over 10 in average. The effect of non-uniformity of calorimeter is also reduced with $1/\sqrt{N_{particle}}$ in a jet . An uncertainty from the two sources is estimated to be smaller than 1% in total.

The error due to the Monte-carlo simulation is estimated by dividing source of correction and estimate their errors individually.

The correction due to crack of the calorimeter was 7% at 50GeV and 4% at 200GeV. We put 50% error of this.

Non-linearity of the calorimeter causes error of 15% at 50GeV and 5% at 200GeV. 50% error was assumed.

The clustering algorithm detects close to 100% energy. Thus error was ignored.

The error of generation algorithm and underlying events is determined by comparing the result of ISAJET and LUND. We conclude 4% at 50GeV and 0.7% at 200GeV.

Finally these errors were summed quadratically. The results of each energy is tableau in table[4-2].

The uncertainty in the jet energy scale is a major contribution to the systematic error in the inclusive jet production cross section. Energy scale itself is about uncertain by 8.4% at Pt = 50GeV/c and 3.4% at Pt = 250GeV/c . The jet cross section falls very steeply with jet Pt. Thus the error in the cross section become 44 % at Pt = 50 GeV/c and 28 % at Pt = 250

GeV/c. The derivative of EHLQ theoretical calculation was used for energy scale to cross section conversion.

Trigger efficiency

To obtain the jet inclusive cross section, we took leading cluster whose energy is grater than 50GeV where the efficiency of the hardware trigger is greater than 99.5% . The error of the efficiency is estimated to be smaller than 100% of inefficiency; 0.5% .

In Fig.[4-2] the inclusive cross sections of jet from various trigger scheme are shown. One can see all of the cross section above 50GeV are same within cross section. The trigger effect is seen below 50GeV comparing each scheme.

Geometrical acceptance , analysis cut and energy resolution

These are discussed in the previous section.

The sources of the systematic error are summarized in Table [4-2].

Comparison with Theoretical Calculation

Curves shown in Fig.4-1 are given by EHLQ based on QCD calculations using different structure functions, EHLQ set1, with $Q^2 = (2Pt)^2$, $Q^2 = Pt$ or $Q^2 = (Pt/2)^2$.

Predictions with other structure functions are shown in Fig.[4-3] (Ref.[4.2]). As seen in this figure , selecting Q^2 scale is more essential than which structure function is used. The curves with the same definition of Q^2 are consistent each other within 10%.Changing the Q^2

definition from $Q^2 = (2Pt)^2$ to $Q^2 = (Pt/2)^2$ enhances the prediction curves by a factor of 2.

Theoretical calculations based on QCD were found to be consistent with the CDF inclusive jet cross section within the systematic error. The UA1 and UA2 results (Ref.[4-3]) are also shown together with a QCD prediction curve by a structure function of EHLQ set 1 with $Q^2 = Pt^2$ in this figure.

Scaled jet cross section

The scaled jet cross section related as

$$P_t^4 E \frac{d^3\sigma}{dp^3} = \frac{P_t^3}{2\pi} \frac{d\sigma}{dP_t d\eta},$$

is plotted against xt=2 Pt/√s in figure [4-4] together with QCD predictions. This quantity is independent of √s in the simple parton model for the reaction exchanging vector particles. This scaling law is generally not strict, since the quantity also depends on Q^2 of the reaction.

Chapter 5
Conclusion

Detector

The CDF detector was successfully constructed. The CDF central calorimeter system was tested and calibrated with cosmic rays and with the high energy beam in the Fermilab NW beam line.

All the calorimeter channels were calibrated with the 50GeV/c pion or electron beam. Various monitoring systems kept calibration constant of each channel of the calorimeter from the beam test to the collider run within 1% reliability for the central hadron calorimeter and 0.6% reliability for the central electromagnetic calorimeter.

The performance of the calorimeter was examined on the cosmic ray test stand , in the beam line and with the collider run.

The energy resolution for the central electromagnetic calorimeter is $\sigma/E = 14\%/\sqrt{E(GeV)}$ and for hadron $70\%/\sqrt{E(GeV)}$ approximately.

The linearity and response maps of the calorimeters were measured with better accuracy than energy resolution.

Jet physics

Proton and antiproton collision at $\sqrt{s}$=1800GeV was observed with the CDF detector. Events were triggered by sum of transverse momentum measured by calorimeter. Events worth of the integrated luminosity of 23.6±3.5nb^{-1} of events were analyzed for the jet study.

We analyzed jet events in the η region $0.1<|\eta|<0.7$ and Pt >50GeV. The Pt of jet was corrected by a function which was obtained by Monte-carlo event generators and the detector simulator based on the beam test results. The function was examined experimentally by π^0 / γ + Jet events.

Acceptance of detector and inefficiencies of the triggering system and software cut were also examined by the Monte-carlo simulation.

The invariant cross section was compared with QCD calculation. They were consistent within the systematic error.

Scaled invariant cross section compared with lower energy results indicates a breaking of the scaling. The scaling violation is consistent with QCD theory.

Appendix: The CDF collaboration

F.Abe[p], D.Amidei[e], G.Apollinari[k], G.Ascoli[g], M.Atac[d], P.Auchincloss[n], A.R.Baden[f], A. Barbaro-Galtieri[i], V.E.Barnes[l], E.Barsotti[d], F.Bedeschi[k], S.Belforte[k], G.Bellettini[k], J.Bellinger[q], J.Bensinger[b], A.Beretvas[n], P.Berge[d], S.Bertolucci[e], S.Bhadra[g], M.Binkley[d], R.Blair[a], C.Blocker[b], J.Bofill[d], A.W.Booth[d], G.Brandenburg[f], A.Brenner[d], D.Brown[f], A.Byon[l], K.L.Byrum[q], M.Campbell[c], R.Carey[f], W.Carithers[i], D.Carlsmith[q], J.T.Carroll[d], R.Cashmore[1], F.Cervelli[k], K.Chadwick[i,d], T.Chapin[m], G.Chiarelli[k], W.Chinowsky[i], S.Cihangir[o], D.Cline[q], D.Connor[j], M. Contreras[b], J.Cooper[d], M.Cordelli[e], M.Curatolo[e], C.Day[d], R.DelFabbro[k], M.Dell'Orso[k], L.DeMortier[b], T.Devlin[n], D.DiBitonto[o], R.Diebold[a], F.Dittus[d], A.DiVirgilio[k], R.Downing[g], G. Drake[d], T.Droege[d], M.Eaton[f], J.E.Elias[d], R.Ely[i], S.Errede[g], B.Esposito[e], A.Feldman[f], B.Flaugher[n], E.Focardi[k], G.W.Foster[d], M.Franklin[f,g], J.Freeman[d], H.Frisch[c], Y.Fukui[h], S.Galeotti[k], I.Gaines[d], A.F.Garfinkel[l], P.Giannetti[k], N.Giokaris[m], P.Giromini[e], L.Gladney[j], M.Gold[i], K.Goulianos[m], J.Grimson[d], C.Grosso-Pilcher[c], C.Haber[i], S.R.Hahn[j], R.Handler[q], D.Hanssen[d], R.M.Harris[i], J.Hauser[c], Y.Hayashide[p], T.Hessing[o], R.Hollebeek[j], L.Holloway[g], P.Hu[n], B.Hubbard[i], P.Hurst[g], J.Huth[d], M.Ito[p], J.Jaske[q], H.Jensen[d], R.P.Johnson[d], U.Joshi[n], R.W.Kadel[d], T.Kamon[o], S.Kanda[p], I.Karliner[g], H.Kautzky[d], K.Kazlauskis[n], E.Kearns[f], R.Kephart[d], P.Kesten[b], H.Keutelian[g], Y.Kikuchi[p], S.Kim[p], L.Kirsch[b], S.Kobayashi[2], K.Kondo[p], U.Kruse[g], S.E.Kuhlmann[l], A.T.Laasanen[l], W.Li[a], T.Liss[c], N.Lockyer[j], F.Marchetto[o], R.Markeloff[q], L.A. Markosky[q], M.Masuzawa[p], P.McIntyre[o], A.Menzione[k], T.Meyer[o], S.Mikamo[h], M.Miller[j], T.Mimashi[p], S.Miscetti[e], M.Mishina[h], S.Miyashita[p], H.Miyata[p], N.Mondal[q], S.Mori[p], Y.Morita[p], A.Mukherjee[d], A.Murakami[2], Y.Muraki[3], C.Nelson[d], C.Newman-Holmes[d], L.Nodulman[a], J.O'Meara[d], G.Ott[q], T.Ozaki[p], S.Palanque[4], R.Paoletti[k], A.Para[d], D.Passuello[k], J.Patrick[d], R.Perchonok[d], T.J.Phillips[f], H.Piekarz[b], R.Plunkett[m], L.Pondrom[q], J.Proudfoot[a], G.Punzi[k], D.Quarrie[d], K.Ragan[j], G.Redlinger[c], R.Rezmer[a], J.Rhoades[q], L.Ristori[k], T.Rohaly[j], A.Roodman[c], H.Sanders[c], A.Sansoni[e], R.Sard[g], V.Scarpine[g], P.Schlabach[g], E.E.Schmidt[d], P.Schoessow[a], M.H.Schub[l], R.Schwitters[f], A.Scribano[k], S.Segler[d], M.Sekiguchi[p], P.Sestini[k], M.Shapiro[f], M.Sheaff[q], M.Shibata[p], M.Shochet[c], J.Siegrist[i], V.Simaitis[g], J.K.Simmons[l], P.Sinervo[j], M.Sivertz[5], J.Skarha[q], D.A.Smith[g], F.Snider[c], L.Spencer[b], R.St.Denis[f], A.Stefanini[k], Y.Takaiwa[p], K.Takikawa[p], S.Tarem[b], D.Theriot[d], J.Ting[c], A.Tollestrup[d], G.Tonelli[k], W.Trischuk[f], Y.Tsay[c], K.Turner[d], F.Ukegawa[p], D.Underwood[a], C.vanIngen[d], R.VanBerg[j], R.Vidal[d], R.G.Wagner[a], R.L.Wagner[d], J.Walsh[j], T.Watts[n], R.Webb[o], T.Westhusing[g], S.White[m], V.White[d], A.Wicklund[a], H.H.Williams[j], T.Winch[q], R.Yamada[d], T.Yamanouchi[d], A.Yamashita[p], K.Yasuoka[p], G.P.Yeh[d], J.Yoh[d], F.Zetti[k]

CDF Member Institutions

[a] Argonne National Laboratory- [b] Brandeis University- [c] University of Chicago
[d] Fermi National Accelerator Laboratory- [e] INFN, Laboratori Nazionali di Frascati, Italy
[f] Harvard University- [g] University of Illinois- [h] KEK, Japan
[i] Lawrence Berkeley Laboratory- [j] University of Pennsylvania
[k] INFN, University and Scuola Normale Superiore of Pisa, Italy- [l] Purdue University
[m] Rockefeller University- [n] Rutgers University- [o] Texas A&M University
[p] University of Tsukuba, Japan- [q] University of Wisconsin

Visitors

[1] Oxford University, England- [2] Saga University, Japan
[3] ICRR, Tokyo University, Japan- [4] CEN, Saclay, France-
[5] Haverford College, Haverford, PA.

References

1. Chapter 1

1.1. British-Scandinabian collab., B.Alper et al., Nucl. Phys. **B100** (1975) 237.

1.2. G.Arnison et al., Phys.Lett.B **121** (1983) 209.
M.Banner et al., Phys.Lett.B **118** (1982) 322.

1.3. F.Abe et al., to be submitted to Phys.Rev.Lett.

1.4. For a review , P.Darriulat, Ann.Rev.Nucl.Part.Sci. **30** (1980)159.

1.5. R.Hagedron in Cargese Lectures in Physics Vol.6(Gorden and Breach, New York, 1973) 643.

1.6. F.W.Busser et al., Phys.Lett. **46B** (1973) 471.

1.7. R.P.Feynmann, Phys Rev.Lett. **23** (1969) 1415.

1.8. S.M.Berman, J.D.Bjorken and J.B.Kogut. Phys.Rev.D **4** (1971) 3388.

1.9. F.Wilczek, Ann.Rev.Nucl.Part.Sci. **30** (1980) 159.

1.10. P.Soding,G.Wolf, Ann.Rev.Nucl.Part.Sci. **31** (1981) 231.

1.11. J.D.Bjorken, Phys.Rev.D**8** (1973) 4098.

1.12. R.D.Field,G.C.Fox,R.L.Kelly Phys.Lett.B **119** (1982) 439.

1.13. R.Singer,T.Fields,W.Seolve, Phys.Rev.D.**25** (1982) 2451.

1.14. M.Banner et al., Phys.Lett. **118B** (1982) 203.
G.Arnison et al., Phys.Lett. **123B** (1982) 115.

1.15. G.Arnison et al., Phys.Lett. **132B** (1983) 214.
G.Arnison et al., Phys.Lett. **172B** (1986) 461.
P.Bagania et al., Phys.Lett. **138B** (1984) 430.
P.Bagania et al., Phys.Lett. **160B** (1985) 349.

1.16. G.Arnison et al., Phys.Lett. **136B** (1983) 294.
G.Arnison et al., Phys.Lett. **177B** (1986) 244.
P.Bagania et al., Phys.Lett. **144B** (1984) 283.

1.17. P.Bagania et al., Z.Phys. C **20** (1983) 117.
J.Appel et al., Z.Phys. C **30** (1986) 341.
G.Arnison et al., Phys.Lett. **158B** (1985) 494.

1.18. G.Arnison et al., Phys.Lett. **132B** (1983) 223.
G.Arnison et al., Phys.Lett. **147B** (1984) 222.
P.Bagania et al., Phys.Lett. **144B** (1984) 291.

1.19. R.Horgan, M.Jacob. Nucl.Phys.B **179** (1981)441.

1.20. G.Altarelli and G.Parisi, Nucl.Phys. **B216**(1977) 298.

1.21. D.W.Duke and J.F. Owens, Phys. Rev. **D30** (1984) 49.

1.22. E.Eichten , I.Hinchliffe , K.Lane and C.Quigg, Rev Mod. Phys. ,**56** (1984) 579. And Errata,**Fermilab-PUB-86/75-T** (1986)

2. Chapter 2

2.1. F.Abe *et al.*, The Collider Detector at Fermilab, submitted to Nucl. Instrum. Methods A.

2.2. F.Snider *et al.*, The CDF Vertex Time Projection Chamber System, submitted to

Nucl. Instrum. Methods A.

2.3. F.Bedeschi *et al.*, Design and construction of the CDF central tracking chamber, submitted to Nucl. Instrum. Methods A.

2.4. H.Frisch *et al.*, **CDF-note250** (1984) unpublished.

2.5. L.Balka *et al.*, The CDF central electromagnetic calorimeter , submitted to Nucl. Instrum. Methods A.

2.6. S.Bertolucci *et al.*,The CDF central and endwall hadron calorimeter, submitted to Nucl. Instrum. Methods A.

2.7. G.Ascoli *et al.*, CDF central muon detector, submitted to Nucl. Instrum. Methods A.

2.8. T.Kamon *et al.*, Nucl. Instrum. Methods **213** (1983) 261.

2.9. Y.Kikuchi Master thesis , University of Tsukuba (1985).

2.10. T.Kamon ibid.

2.11. T.Devlin *et al.*, Phototube testing for CDF, submitted to Nucl. Instrum. Methods A.

2.12. S.R.Hahn *et al.*, Calibration systems for the CDF central electromagnetic calorimeter, submitted to Nucl. Instrum. Methods A.

2.13. G.Drake *et al* ., IEEE Trans.Nucl SCI **33** (1986) 92.

G.Drake *et al* ., IEEE Trans.Nucl SCI **33** (1986) 893.

G.Drake *et al* ., Front end electronics: the RABBIT system submitted to Nucl. Instrum. Methods A.

2.14. C.Swenberg and N.E.Geactinov in, **Organic Molecular Photophysics** J.Birks, ed. (J.Wiley and Sons, New York, 1973) vol.1

S.Bertolucci *et al.*, Nucl. Instrum. Methods A **254** (1987) 561.

2.15. R.G.Wagner *et al.*, Cosmic ray test of the CDF central calorimeters submitted to Nucl. Instrum. Methods A.

2.16. P.J.Green *et al.*, Phys. Rev. **D20** (1978) 1598.

2.17. U.Amaldi, Physica Scripta, **23** (1981) 409.

2.18. Electromagnetic shower simulation in GHEISHA program by H.Fesefeldst , The shower simulation of hadronic showers **PITHA85/02.**

2.19. J.B.Birks, **Scintillation counters** , Pergamon-Press London (1953).

2.20. S.L.Stone et al., Nucl. Instrum. Methods **151** (1978) 387.

2.21. M.J.Corden *et al.*, Nucl. Instrum. Methods A. **238** (1985) 273; Physica Scripta 25 (1982)5; Physica Scripta **25** (1982) 11.

3. Chapter 3

3.1. M.M.Block and R.N.Cahn, Phys.Lett.,**188b**, 143 (1987).

3.2. M.Bozzo et al., Phys Lett., **147B**, 392 (1984).

3.3. G.J.Alner wt al., Z.Phys. C, **32**, 153 (1986).

3.4. F.E.Paige and S.D. Protoppopescu , **Proceedings of the UCLA workshop on SSC physics** (1986) 213.

3.5. H.U.Bengtsson and G.Ingelman, Computer Phys. Comm. 34 (1985) 251.

T.Sjostrand, Phys. Lett. **157B**, (1985) 321.

H.U.Bengtsson and T.Sjostrand , "PYTHIA 4.70" , **Proceedings of the 1986 Snowmass DPF Summer Study** (1986) 311.

3.6. J.Freeman and M.Eaton, **Description of CDF calorimetry simulation**

(May 1985) (unpublished)

Bertani and DelFabbro, **CDFnote-No.102** (unpublished)

Y.Hayashide, T.Kamon and J.Freeman, **CDFnote-No.287** (unpublished)

4. Chapter 4

4.1. Eichten et al., ibid.

4.2. Duke et al., Ibid.

4.3. G.Arnison et al., Phys.Lett. **132B** (1983) 214.

G.Arnison et al., Phys.Lett. **172B** (1986) 461.

P.Bagania et al., Phys.Lett. **138B** (1984) 430.

Table Captions

1. Chapter 1

1.1. Matrix elements for parton+parton → parton+parton scattering. s, t and u are the Mandelstam variables in the center of mass system of partons. q' denotes a different flavour from q.

2. Chapter 2

2.1. A summary of the calorimeter properties by system.

2.2. Central electromagnetic calorimeter (CEM) summary

2.3. Parameters of the central hadron calorimeter (CHA).

2.4. Parameters of the endwall hadron calorimeter.

2.5. Specifications for central electromagnetic strip chamber.

2.6. Specifications for Central electromagnetic photomultiplier.

2.7. Average and widths of cosmic ray muon peaks in the CEM.

2.8. (a); Deviations in dissimilarity. (b);Deviations in dissimilarity along x. (CEM)

2.9. Average values and deviations of w and L. (CEM)

2.10. Parameters in Z dependence of L. (CEM)

2.11. Averages and widths of cosmic ray muon peaks (sample of 12 hadron calorimeter modules, towers 0 to 3). Last column shows average muon peaks measured with the test beam (sample of 50 hadron calorimeters)

2.12. Average cosmic ray muon and 50GeV pion peaks of CHA. Last column gives the averages of the ratios between cosmic ray muon

and pion peaks.

2.13. Total number of photoelectrons of CHA as measured from L/R and from (R-L) distributions, and their average.

2.14. Estimated scintillator attenuation length on the plane separating the EM and hadron sectors

2.15. Typical linearity and energy resolution of each tower of a CEM. Output is normalized by 50GeV data of each tower. Resolution : σ/E: is producted by $\sqrt{E(GeV)}$.

2.16. Energy resolution of tower 0 to 5 of a CEM with various cut at 50GeV. Resolution : σ/E: is producted by $\sqrt{E(GeV)}$. Position cut only , CEM + (optimized factor)*CHA and cut if deposit in CHA greater than 2GeV.

2.17. Parameters in the response function for towers 0 to 9 of CEM.

3. Chapter 3

3.1. Summary of trigger conditions. Left number of "/" is one trigger tower threshold and right number is threshold for sum of each detector. Unit is GeV. Trigger was made by these "OR"ed signal.

3.2. Fit quality for jet energy correction for various divided Pt region. ISAJET generation was used.

3.3. Summary of isolated $\pi 0$/gamma + jet events. Away jet error was obtained by gaussian fit sigma or RMS of distribution (smaller one).

4. Chapter 4

4.1. Inclusive jet cross section.

4.2. Systematic errors in inclusive jet cross section.

Figure Captions

1. Chapter 1

1.1. First-order diagrams for hard parton scattering. Gluons: curly line, quarks:straight lines.

1.2. (a)Parton distribution at $Q^2=5(GeV/c)^2$, calculated in Soft gluon" version (Λ=200MeV) of Ref.[1.21]: valence quark distribution $x(u_v(x)+d_v(x))$ (solid line), gluon distribution xG(x) (dashed line) and sea quark distribution q(x) (dotted-dash line).

(b)Parton distribution at $Q^2=5(GeV/c)^2$, calculated with Set 1 of Ref.[1.22]. Line assignments are the same as (a).

(c)Parton distribution at $Q^2=5(GeV/c)^2$, calculated with Set 2 of Ref.[1.21]. Line assignments are the same as (a).

(d)Parton distribution at $Q^2=10^4(GeV/c)^2$, calculated in "Soft gluon" version (Λ=200MeV) of Ref.[1.21]. Line assignments are the same as (a).

(e)Parton distribution at $Q^2=10^4(GeV/c)^2$, calculated with set 1 of Ref.[1.22]. Line assignments are the same as (a).

(f)Parton distribution at $Q^2=10^4(GeV/c)^2$, calculated with Set 2 Ref.[1.22]. Line assignments are the same as (a).

2. Chapter 2

2.1. A perspective view of the CDF detector showing the central detector and the forward and backward detectors.

2.2. A cut-away view through the forward half of CDF. The detector is forward-backward symmetric about the interaction point.

2.3. Hadron calorimeter towers in one of eight identical η–ϕ quadrants ($\Delta\phi$ = 90°, η>0). The heavy lines indiacte module or chamber boundaries. The EM calorimeters have complete ϕ-coverage.

2.4. A cross sectional view of a module of the central electromagnetic calorimeter. Viewed along the beam direction.

2.5. A perspective and cross sectional view of a module of the central electromagnetic calorimeter. The coordinate system is used generally in this thesis.

2.6. Absorption and emission spectrum of phosphor used for the scintillator (buthyl-PBD and BDB) and wavelength shifter (Y-7). Curves drawn lower are absorption, upper is emission spectra.

2.7. Typical response map of a wavelength shofter (tower 4). (a) is uncorrected one. With backing plate, the response map is corrected as (b)

2.8. An schematic view of light collection and equipments for calibration system of the central electromagnetic calorimeter (tower 1).

2.9. A circuit of the photomultipiler base for the central electromagnetic calorimeter.

2.10. Typical distributions of results from xenon flash runs. (a) Distribution of raw phototube signals (in ADC counts) seen during xenon flash runs. (b) Distribution of PIN diode signals (in ADC counts) seen during xenon flash runs. (c) Distribution of ratios of raw phototube signals to PIN diode signals (in dimensionless units) for xenon flash runs.

2.11. Comparisons of two xenon flash and LED runs separated by about a day. For the xenon flash, the ratio of raw phototube signal to PIN diode signals was compared; while for the LED's the raw phototube signal was used.

2.12. Some typical long-term variations in source response over a period of about nine months. For 95% of the phototubes, the variation in response was flat (a); in a small number of cases, the response fell (b) or rose (c) or an abrupt change was seen (d)

2.13. Some typical long-term variations in xenon flash and LED response over a period of about three months.

2.14. Calibration reproducibility. The differense in beam to Cs137 source ratio for each tube is plotted for successive calibration procedures, about 5 weeks apart, for three modules. The deviation of the centroid from zero corresponds accurately to the

source decay.

2.15. Calibration uniformity. A recent distribution (May1987) of channel - to -channel energy response gain variations for all CEM calorimeter channels (a) demonstrates good uniformity in energy response. A distribution of the same quantity is also shown as measured from the test beam calibration (b).

2.16. Percentage difference between the collision run (May 1987) calibration and the original test beam calibration for the energy response.

2.17. Percent change in Cs137 source response as a function of the CDF superconducting solenoid field (nominal field 1s 1.5T=15kG)

2.18. Two WLS strips collect light from each scintillator layer of the central hadron calorimeter (CHA). In the air gap between WLS and light guide, filters are inserted to insure the light output equalization for different layers of the same tower.

2.19. A response map of a scintillitor for CHA read by WLS positioned at q = constant as shown in Fig.[2.18]. The displayed values are the sum of PM1 and PM2

2.20. Response of an Endwall tower, when irradiated by the *skin source*. Peaks correspnd to the passage of the source in front of one layer of the tower. Coupling scintillators to light guides, selected according to their attenuation length, is not sufficient to get uniformities of better than 15% ; (a). The result in (b) is achieved by inserting filters in the air gap between WLS and light guides.

2.21. Percentage difference between corresponding pion peaks of seven re - calibrated modules. The peak values are normalized to the reference I_{CS137} currents.

2.22. Percentage difference between the Ic currents of each p.m. and the mean value of the ic's corresponding to towers with the same towers with the same number. On each P.M. the Ic's were scaled, via I_{CS137} , to give a pion calibration of 2pc/GeV.

2.23. Distribution of percentage differences of I_{CS137} currents in the endwall tubes, when measured in the presence no magnetic field and with the superconducting solenoid at 1.5T, representing combined scintillator, WLS amd p.m. response changes.

2.24. Percentage differences of the charges produced by the endwall p.m.'s exposed to light from the laser system, when measured with the magnetic field "on" (1.5T) and "off".

2.25. Change of the attenuation length of ascintillator for the CHA exposed to increasing radiation doses.

2.26. Schematics of the setup of the cosmic ray test stand.

2.27. Difference between the average Cs137 source calibration current at the beginning of cosmic ray data taking and at the end. The average is histogrammed for each tube individually in 26

different modules. The mean difference is -0.21% and the standard deviation of the distribution is 0.62%.

2.28. (a) ; Calibrated charge integrator gains as a function of date of calibration for three channels on three different boards. The data between June 1984 and December 1984 have been re - scaled by a factor of 0.979 to correct for a charge in the voltage calibration of the BNC 9010 pulse generator. The boards were prototype versions of the final front end electronics. The nominal gain of the charge channels was unchanged between the prototype and final versions. (b); Calibrated current amplifier gains as a function date of calibration for two channels on two different prototype front end electronics boards. The final electronics design used a nominal gain of 11pA/ADC count and has a stability similar to that implied by the data in this figure.

2.29. (a) ; Typical pulse hight distribution of cosmic ray muons viewed by a left tube in an CEM tower. (b) ; Typical pulse hight distribution of cosmic ray muons viewed by a right tube in an CEM tower. (a) ; Typical pulse hight distribution of cosmic ray muons viewed bysum of two tubes in an CEM tower.

2.30. Number of photoelectrons per GeV for each phototube in a module from LED measurements.

2.31. A scatter plot of pulse heights of cosmic ray muons and 50GeV punch - through particles.

2.32. The average response along Z for each fixed X over 41 modules.

(a);x=15.3cm and (b);x=2.2cm.

2.33. Dissimilarity distributions in towers 0-8 , for four different modules.

2.34. (a);Typical response map in X at the Z-center in a tower and fit to cosh(x/w). (b); The distribution of the ratios of two tube outputs in X at the z- center in a tower and fit to exp(-x/L)

2.35. Distributions of w's and L's measured at tower centers.

2.36. Dependences of w and L on Z, where the values w and L are normalized by the average value over tower centers for each module.

2.37. Polynomial fits of z dependence of L for each tower using 46 modules. The data are averaged L/L(mean) over 46modules.

2.38. Correlation plot of L and w using the values at the tower centers of towers 0-9 over 46 modules.

2.39. Typical pulse height distribution for cosmic ray muons as seen by one phototube of CHA.

2.40. Distribution of muon peak pulse heights in CHA.

2.41. Distribution of muon peaks seen by each phototube at x=0 for differentz-values.

2.42. Distribution of muon peaks in a tower for all 9 x , z regions defined in the text.

2.43. A schematic view of the NW beam line at Fermilab.

2.44. Momentum distribution of electrons nominal 50GeV/c in the NW beam line.

2.45. Pulse height distribution of output of a CEM tower for electrons 15 , 25 , 50 and 75GeV/c.

2.46. (a)-(f); linearity of each tower of CEM measured by electron.

2.47. A scatter plot of CEM output (x) vs CHA (y) for 50GeV/c electron.

2.48. Energy resolution of tower 0 - 5 of CEM. Results of Z-cut only , EM + (optimized factor)*hadron and hadron deposit greater than 2GeV events cut are seen.

2.49. Typical response map of a CEM tower measured by 50GeV/c electrons. Each mesh is 1cm by 1cm.

2.50. Plot of sums of the left and right tube outputs as a function of x. Dashed, dot - dashed and dotted curves represent cosh (x/w) with w=44.2cm (the beast for w), 82.6cm(best for p) and 86.6cm (beast for L) respectively.

2.51. Plot of ratios of the left and right tube outputs as a function of x fitted to exp(-2x/L).

2.52. Schematics of ϕ-crack region.

2.53. Typical response map at ϕ-crack. A solid curve is a fit function.

2.54. Typical z-dependence of the response at x=0; (a) tower1, (b)tower 0 and (c) tower 9. Data from the cosmic ray test are also plotted for comparison.

2.55. Typical x-dependence of the response at tower centers ; (a) tower1, (b)tower 0 and (c) tower 9. Data from the cosmic ray test are also plotted for comparison.

2.56. A response founction for a tower.

2.57. Distribution of the deviations in nob - uniformity.

2.58. Distributions of the deviations in similarity.

2.59. Distributions of the deviations in local reproducibility (solid line) and global reproducibility (dashed line).

2.60. Distributions of the deviations in reproducibility with respect to a simple response function $p_1\cosh(x/p_6)$

2.61. Linearity plot of tower 5 of CHA for pion energies ranging from 10 to 150GeV.

2.62. Linearity of CHA. Data point lower than 10GeV/c were taken at the collider run with CTC. Data above 10GeV/c are the beam test data.

2.63. Pulse height distribution for 50GeV pions in tower 1 of CHA. Only pions which are minimum ionization particle in the CEM are plotted.

2.64. Pulse height distribution for 50GeV pions in tower 10 of wall hadron calorimeter. Selection for pions are the same as Fig.[2.63]

2.65. Pulse height distribution for 50GeV pions in tower 1 of CHA. Pions interacting in the CEM are included and pulse height is the sum of CEM and CHA.

2.66. Energy resolusion as function of pion energy for towers 1, 5 and 10.

2.67. $\theta(\eta)$ response of the calorimeter. The ratio between the measured and the incident energies is shown for different beam positions expressed as function of η . The beam was centered in ϕ.

2.68. Fraction of the total energy deposited in neighboring towers as function of the tower number. Beam was hitting the tower centers.

2.69. The logarithm of the ratio of the left (L) and right (R) p.m. pulse heights in a tower as function of the distance of the particle from the tower center. The dimentions refer to a scintillator located at a longitudinal depth close to the shower maximum.

2.70. Position resolution as function of the distance from tower center for different pion energies.

2.71. ϕ response to a 50GeV pion beam sweeping the facing towers of two stacked modules. The beam was aimed at the tower center in θ and had a radius ~2cm.

2.72. Fine ϕ scan of the interface region between two modules. Each point is the average of the energy in a 1mm bin.

2.73. Observed hot spot pulse height as function of the electron energy and for different thickness of the crack radiator. Response is linear as function of energy and is reduced by a factor ~10 by 10 radiation lengths of absorbing material.

2.74. An isometric view of two VTPC modules. They are rotated in f by 11.3° with respect to each other.

2.75. Distribution of impact parameters for all tracks. The sigma of the distribution is 0.3cm.

3. Chapter 3

3.1. A typical event of two jet project onto $\eta - \phi$ plane of calorimeter.

3.2. Distribution of collision point of events of which the leding cluster Et>70GeV.

3.3. Distribution of fraction of EM calorimeter deposit in total energy deposit of a jet Et>10GeV. Dashed line is before TOF cut. Solid line is after TOF cut.

3.4. Integral of fraction of particle momentum fragmented from 100GeV/c Pt jets. For example particles that have less than 20GeV momenta carry 75% of total jet momentum.

3.5. Typical distribution of Pt(observed cluster) / Pt (jet). Both values are defined in the chapter. This distribution were accumulated in the range of 120GeV/c <Pt(jet)<130GeV/c. 500 events were generated by ISAJET and simulated by the standard CDF detector simulation package.

3.6. Relation of cluster Pt (GeV/c) and corresponding parton pt generated by ISAJET and cluser was observed in the result of CDF detector simulation. Two straight curves are applied for the best fit. Dashed line express a result of LUND generation.

3.7. The phi difference between an isolated electromagnetic cluster

and an away jet. A cut was applied as phi<160°.

3.8. The ratio distribution of Et of electromagnetic cluster and of the away jet.

3.9. The Pt distribution of a π^0/γ + jet events. This distribution was compared with the curve obtained using the simulation data to make sure the source of these events. QCD γ shows the Pt distribution of a gamma in the isolated γ + jet events which come from direct photon events generated by PYTHIA/LUND generation.

3.10. (a); The scatter plot of Pt of away jet versus Pt of the isolated π^0/γ + jet events. (b);Plot of the away jet pt in the isolated π^0/γ + jet events. The best fit is shown by a solid straight line. The energy correction curves from ISAJET and LUND are shown by a dotted lineand dashed line respectively.

3.11. The level 1 trigger efficiency as a function of leading jet Pt.

3.12. Typical shape of geometrical acceptance, analysis cut and energy resolution as a function of h in the Pt range between 120 and 140GeV/c.

3.13. The correction factor for geometrical acceptance, analysis cut and energy resolution as a function of jet Pt after integrating over rapidity. The error bar shows the statistical error of the Monte-Carlo simulation.

4. Chapter 4

4.1. Inclusive jet cross section in 1.8TeV proton and antiproton collisions with the statistical error only. UA1 and UA2 data are shown together. RApidity range of CDF is $0.1<|\eta|<0.7$ and UA1 and UA2 is $0<|\eta|<0.7$. Dashed and solid line show the QCD theoretical prediction with a structure function of EHLQ set 1 $Q^2=pt^2/4$, $Q^2=Pt^2$ and $Q^2=Pt^2\times4$ respectively.

4.2. Inclusive jet cross section for various trigger condition run. (a)comparing low and medium trigger run. (b)medium,high and burn run. One can see the trigger effect around 40 to 50GeV and no systematic difference between these runs above 50GeV.

4.3. Inclusive jet cross section by QCD precdiction with various structure function.

4.4. Scaled jet cross section in 1.8TeV proton and antiproton collisions. UA2 data are shown together. Dashed and Solid curves show the QCD theoretical prediction curves at $\sqrt{s}$=630GeV and 1800GeV with a structure function of EHLQ set 1 ($Q^2=Pt^2$), respectively.

Table [1. 1]

Subprocess	$\lvert M \rvert^2$	$\lvert M \rvert^2$ at $\theta = 90°$
$qq' \to qq'$ $q\bar{q}' \to q\bar{q}'$	$\frac{4}{9}\frac{s+u}{t^2}$	2.22
$qq \to qq$	$\frac{4}{9}\left[\frac{s^2+u^2}{t^2}+\frac{s^2+t^2}{u^2}\right]-\frac{8}{27}\frac{s^2}{ut}$	3.26
$qq \to \bar{q}'\bar{q}'$	$\frac{4}{9}\frac{t^2+u^2}{s^2}$	0.22
$q\bar{q} \to q\bar{q}$	$\frac{4}{9}\left[\frac{s^2+u^2}{t^2}+\frac{t^2+u^2}{s^2}\right]-\frac{8}{27}\frac{u^2}{st}$	2.59
$q\bar{q} \to gg$	$\frac{32}{27}\frac{u^2+t^2}{ut}-\frac{8}{3}\frac{u^2+t^2}{s^2}$	1.04
$gg \to q\bar{q}$	$\frac{1}{6}\frac{u^2+t^2}{ut}-\frac{3}{8}\frac{u^2+t^2}{s^2}$	0.15
$qg \to qg$ $\bar{q}g \to \bar{q}g$	$-\frac{4}{9}\frac{u^2+s^2}{us}+\frac{u^2+s^2}{t^2}$	6.11
$gg \to gg$	$\frac{9}{2}\left[3-\frac{ut}{s^2}-\frac{us}{t^2}-\frac{st}{u^2}\right]$	30.38

Table [2. 1]

Summary of Calorimeter Properties

	Central		Endwall	Endplug		Forward	
	EM	Hadron	Hadron	EM	Hadron	EM	Hadron
$\lvert\eta\rvert$-coverage	0-1.1	0-0.9	0.7-1.3	1.1-2.4	1.3-2.4	2.2-4.2	2.3-4.2
Tower size, $\Delta\eta \times \Delta\phi$	~0.1×15°	~0.1×15°	~0.1×15°	0.09×5°	0.09×5°	0.1×5°	0.1×5°
Longitudinal samples in tower	1°	1	1	3	1	2	1
Active medium	polystyrene scintillator	acrylic scintillator	acrylic scintillator	Proportional tube chambers with cathode pad read			
Scintillator thickness or proportional tube size	0.5 cm	1.0 cm	1.0 cm	0.7×0.7 cm^2	1.4×0.8 cm^2	1.0×0.7 cm^2	1.5×1.0 cm^2
Number of layers	31	32	15	34	20	30	27
Absorber	Pb	Fe	Fe	Pb	Fe	94%Pb, 6% Sb	Fe
Absorber thickness	0.32 cm	2.5 cm	5.1 cm	0.27 cm	5.1 cm	0.48 cm	5.1 cm
Typical phototube or wire high voltage	-1100V	-1500V	-1100V	+1700V	+2120V	+1900V	+2200
Typical phototube or wire gain	1.2×10^5	6×10^5	10^6	2×10^3	2×10^4	5×10^3	10^4
Typical tower signal	.4pC/GeV	.4pC/GeV	.4pC/GeV	+1.25pC/GeV	+1.3pC/GeV	+2pC/GeV	+0.7pC/$\sqrt{\text{GeV}}$
Energy resolution (σ/E) at 50 GeV	2%	11%	14%	4%	20%	4%	20%
Typical position resolution at 50 GeV	0.2×0.2 cm^2*	10×5 cm^2	10×5 cm^2	0.2×0.2 cm^2	2×2 cm^2	0.2×0.2 cm^2	3×3 cm^2
Characteristic width of azimuthal boundary region	3.5 cm	4.1 cm	3.8 cm, 8.9 cm alternating	0.9 cm	0.8 cm	0.7 cm; 3.2 cm**	1.3 cm 3.2 cm

*An imbedded proportional tube chamber at shower maximum gives some additional information. The quoted position resolution is measured with this chamber.
**The first number is for the vertical boundary, the second for the horizontal.

Table [2. 2]

Central Electromagnetic Calorimeter Summary.

Modules	
12/arch + 2 spare	50
Length	98 in.
Width	15° in ϕ (17.9 in. at 68÷ in. from beamline)
Depth (including base plate)	13.6 in.
Weight	2 metric tons
Towers	
10/module	478
Length	$\Delta\eta$ 0.11 ($\frac{1}{2}$ of width)
Thickness (see Table 2)	18 X_0, 1 L_{abs} (÷coil etc.)
Layers	20–30 lead 21–31 scintillator 1 strip chamber
Lead	$\frac{1}{8}$ in. aluminum clad
Scintillator	5 mm SCSN-38 polystyrene
Wavelength shifter	3 mm Y7 UVA acrylic
Photomultiplier tubes (956 channels)	Hamamatsu R580 ($1\frac{1}{2}$ in.)
Chambers (see Table 4)	
Depth	5.9 X_0 (including coil)
Wire channels (64/module)	3072
Strip channels (128/module)	6130
Angular coverage	
θ	about 39°–141°
ϕ	complete
Pseudorapidity	about ±1.1
Performance (high = 30÷ GeV)	
pe/GeV	100÷/tube
Energy resolution σ/E (GeV)	$13.5\%/\sqrt{E}$
Position resolution (high)	±2 mm
Strip/wire PH correlation	8–10%
Wire PH resolution (high)	±25%
Hadron rejection (at 50 GeV) without strip chamber information	$2\text{–}3 \times 10^{-3}$

Table [2. 3]

Parameters of the Central hadron Calorimeter

Modules

Number of modules	48
Length	2.5 m
Width (in ϕ direction)	1.33 m.
Weight per module	12,000 kg.

Towers

Total number (8/module)	384
Length ($\Delta\phi = 15^0$)	0.56 to 0.91 m.
Width ($\Delta\eta = 0.11$)	0.28 to 0.45 m
Total depth (hadron calorimeter alone)	4.7 Λ_{abs}

Layers

Number	32
Steel thickness	2.5 cm
Scintillator thickness	1.0 cm
Scintillator type	PMMA doped with 8% Naphtalene 1% Butyl-PBD and .01% POPOP
Wave shifters	UVA PMMA doped with 30 mg/l Laser dye #481
Number of phototubes	768

Table [2. 4]

Parameters of the End Wall hadron Calorimeter

Modules

Number of modules	48
Approximate dimensions	0.8 X 1.0 X 1.1 m^3
Weight per module	7,000 kg.

Towers

Total number (6/module)	288
Length ($\Delta\phi = 15^0$)	0.35 to 0.78 m.
Width ($\Delta\eta = 0.11$)	0.25 to 0.40 m
Total depth (hadron calorimeter alone)	4.5 Λ_{abs}

Layers

Number	15
Steel thickness	5 cm
Scintillator thickness	1.0 cm
Scintillator type	PMMA doped with 8% Naphtalene 1% Butyl-PBD and .01% POPOP
Wave shifters	UVA PMMA doped with 30 mg/l Laser dye #481
Number of phototubes	576

Table [2. 5]

Central Electromagnetic Strip Chamber Characteristics. 121.2 cm from the 90° edge of the module corresponds to the boundary between the fifth and sixth scintillator towers.

CHAMBER SPECIFICS

Perpendicular distance to beamline		**184 cm**
Wire channels (64)		
Extrusion		**3 piece aluminum**
	cell	**0.250 in. deep by 0.239 in.**
	wall	**0.047 in. (16.4%)**
Wire		**0.002 in. Au plated W**
Readout		**RABBIT**
	Split	**121.2 cm from 90° edge**
	Canging	**pairs except edges (1.453 cm)**
	Blocking capacitor	**200 pF**
Strip channels (128)		
Section 1		**6.2–121.2 cm from 90° edge**
	strips	**69 x 1.67 cm**
Section 2		**121.2–239.6 cm from 90° edge**
	strips	**59 x 2.01 cm**
Total thickness		**0.75 in.**
		0.069 radiation lengths
		0.022 absorption lengths
High voltage		**1420 V**
Feedin		**separate by logical channel**
Cable		**stripped RG–174**
Protection		**1 MΩ on board**
Gas		**95%/5% Ar/CO_2**
Flow		**parallel**

Table [2. 6]

Salient photomultiplier tube specifications.

PHOTOMULTIPLIER SPECIFICATIONS (1.5 in. dia.)

1. High voltage for current gain of 4. $\times 10^5$ less than 1700 V. Total range of required high voltage within 300 V.
2. Bialkali or Multialkali: quantum efficiency for Y7 spectrum greater than 8% (all tubes).
3. No tube dark current above 5 nA for gain of 4. $\times 10^5$.
4. Linearity within 1% up to output pulses of 1200 pC.
5. Gain stability after burnin within 1% for 100 hours for anode currents up to 2 μA, within 2% for 1000 hours at 50 nA.
6. Gain change between 50 nA and 2 μA within 5%, between 5 nA and 500 nA within 1.5%.
7. Recovery to within 2% of nominal gain within 1 msec after a full scale pulse (1200 pC).
8. Gain dependence on temperature within 0.5% per °C.
9. Expected useful lifetime within specifications greater than 50000 hours.

Table [2. 7]

Tower	0	1	2	3	4	5
Average	595.31	599.20	616.02	603.71	602.81	609.99
Width	26.15	24.29	25.56	28.64	31.97	27.78

Tower	6	7	8	9	
Average	655.29	651.02	657.21	624.79	
Width	28.89	26.79	27.33	28.65	(unit: fC)

Table [2. 8]

(a)

Tower	All Area	Central Area	Theta-edge	Phi-edge	(*)
0	0.84 +/- 0.39	0.71 +/- 0.18	0.60 +/- 0.31	1.46 +/- 0.20	0.93
1	0.98 +/- 0.40	0.80 +/- 0.25	0.98 +/- 0.30	1.46 +/- 0.42	0.82
2	0.79 +/- 0.37	0.64 +/- 0.24	0.71 +/- 0.33	1.30 +/- 0.25	0.78
3	0.86 +/- 0.36	0.68 +/- 0.26	1.04 +/- 0.30	1.20 +/- 0.31	0.69
4	1.13 +/- 0.42	0.96 +/- 0.26	1.15 +/- 0.48	1.54 +/- 0.38	0.72
5	1.13 +/- 0.35	1.00 +/- 0.24	1.02 +/- 0.32	1.55 +/- 0.27	0.89
6	1.00 +/- 0.68	0.62 +/- 0.27	0.99 +/- 0.41	1.78 +/- 0.83	0.69
7	0.91 +/- 0.48	0.71 +/- 0.22	0.73 +/- 0.36	1.54 +/- 0.51	0.66
8	0.94 +/- 0.61	0.71 +/- 0.28	0.76 +/- 0.36	1.76 +/- 0.77	0.88
9	2.14 +/- 0.77	1.20 +/- 0.42	2.13 +/- 0.69	2.76 +/- 0.62	0.80
0-8	0.95 +/- 0.47	0.76 +/- 0.28 (Average=1.20 +/- 0.55)	0.87 +/- 0.46	1.48 +/- 0.44	0.79

(*) Dissimilarity from electron data for the whole area. For tower 9, the data for Z > 10 cm are removed in estimating dissimilarity.

(b)

Median X (cm)	Wire Group Number	Dissimilarity (%) Cosmic Ray Data Towers 0-8	Tower 9	Beam Test Towers 0-9
0.0	5, 6	0.39 +/- 0.60	1.86 +/- 0.52	0.38 %
6.5	4, 7	0.66 +/- 0.32	1.79 +/- 0.75	-
10.9	3, 8	0.77 +/- 0.32	2.16 +/- 0.90	-
15.3	2, 9	0.93 +/- 0.27	2.18 +/- 0.55	-
19.6	1,10	1.48 +/- 0.44	2.76 +/- 0.62	1.77 %

Table [2. 9]

	Average (cm)	Tower-to-tower deviation (%)	Module-to-module deviation (%)
w	55.0	5.6	9.2
L	99.3	3.3	9.0

(1) The errors for w and L are typically 6 % and 2 %.

Table [2.10]

Tower	L_0 (cm)	C_1 (x 10**-3)	C_2 (x 10**-3)
0	100.9 +/- 8.1	7.18 +/- 5.76	1.44 +/- 0.71
1	101.2 +/- 8.7	0.19 +/- 4.84	1.19 +/- 0.37
2	97.9 +/- 8.5	0.42 +/- 3.86	0.94 +/- 0.38
3	98.0 +/- 9.3	3.74 +/- 3.52	1.25 +/- 0.43
4	98.2 +/- 8.9	1.79 +/- 3.39	1.15 +/- 0.48
5	96.7 +/- 8.9	4.17 +/- 6.23	1.32 +/- 0.53
6	96.7 +/- 8.7	1.58 +/- 4.25	1.11 +/- 0.68
7	98.2 +/- 8.8	-0.03 +/- 4.12	1.20 +/- 0.53
8	99.9 +/- 7.9	0.90 +/- 3.81	1.26 +/- 0.63
9	85.9 +/- 6.3	-3.24 +/- 4.09	2.17 +/- 0.79

Table [2.11]

Tower	peak(pC)	HWFM(pC)	(%)	peak(pc)(testbeam)
0	4.26	0.22	5.2	4.3
1	4.29	0.30	7.1	4.4
2	4.51	0.24	5.4	4.5
3	4.90	0.27	5.4	4.9

Table [2.12]

tower	π(pc)width(%)	μ(pC)width(%)	50GeV*μ/π
0	115.2 6.7	4.28 3.5	1.85
1	118.9 3.1	4.30 3.7	1.81
2	121.1 2.8	4.53 2.6	1.86
3	122.6 7.0	4.77 4.4	1.99

Table [2.13]

tower	Npe (1)	Npe(2)	Average
0	16.1±0.5	20.±1	18.0
1	18.7	21.	19.8
2	17.3	22.	19.6
3	20.3	28.	24.2
4	21.2	28.	24.6

Table [2.14]

Tower	L(cm)
0	119
1	107
2	123
3	133

Table [2.15]

TOWER	ENERGY(GeV)	MEAN/ENERGY	ERROR	MEAN(%)-1	RESOLUTION (%/SQRT(E GeV))
0	10.000	0.96719E+00	0.22701E-02	-3.281	12.398
0	15.000	0.97636E+00	0.17636E-02	-2.364	15.580
0	25.000	0.97261E+00	0.12509E-02	-2.739	15.870
0	37.500	0.98483E+00	0.10589E-02	-1.517	18.295
0	50.000	0.10000E+01	0.89250E-03	0.000	15.037
0	75.000	0.10067E+01	0.12555E-02	0.667	18.582
1	10.000	0.98957E+00	0.26276E-02	-1.043	12.899
1	15.000	0.99204E+00	0.13867E-02	-0.796	12.799
1	25.000	0.98179E+00	0.10553E-02	-1.821	12.524
1	37.500	0.99895E+00	0.83688E-03	-0.105	14.842
1	50.000	0.10000E+01	0.59727E-03	0.000	14.102
1	75.000	0.10078E+01	0.94403E-03	0.778	16.842
2	10.000	0.98176E+00	0.23100E-02	-3.824	11.893
2	15.000	0.96617E+00	0.15774E-02	-3.383	14.869
2	25.000	0.97498E+00	0.89432E-03	-2.504	12.485
2	37.500	0.99386E+00	0.90601E-03	-0.615	16.122
2	50.000	0.10000E+01	0.61168E-03	0.000	14.227
2	75.000	0.10024E+01	0.91217E-03	0.244	17.048
3	10.000	0.94134E+00	0.39098E-02	-5.866	19.832
3	15.000	0.96604E+00	0.14520E-02	-3.396	13.490
3	25.000	0.97368E+00	0.11270E-02	-2.632	14.105
3	37.500	0.99099E+00	0.85616E-03	-0.901	14.917
3	50.000	0.10000E+01	0.61203E-03	0.000	14.477
3	75.000	0.10037E+01	0.70556E-03	0.372	13.156
4	10.000	0.10012E+01	0.24038E-02	0.124	11.438
4	15.000	0.97560E+00	0.15380E-02	-2.440	13.530
4	25.000	0.97624E+00	0.10591E-02	-2.376	14.433
4	37.500	0.99501E+00	0.90834E-03	-0.499	14.706
4	50.000	0.10000E+01	0.53134E-03	0.000	15.537
4	75.000	0.10131E+01	0.10367E-02	1.314	18.118
5	10.000	0.10068E+01	0.53346E-02	0.677	22.103
5	15.000	0.98759E+00	0.17400E-02	-1.241	14.150
5	25.000	0.97779E+00	0.13885E-02	-2.221	15.860
5	37.500	0.99281E+00	0.10391E-02	-0.719	16.100
5	50.000	0.10000E+01	0.64593E-03	0.000	14.866
5	75.000	0.99770E+00	0.10193E-02	-0.230	17.088
6	10.000	0.00000E+00	0.00000E+00	-100.000	0.000
6	15.000	0.00000E+00	0.00000E+00	-100.000	0.000
6	25.000	0.00000E+00	0.00000E+00	-100.000	0.000
6	37.500	0.98873E+00	0.12527E-02	-1.127	15.633
6	50.000	0.10000E+01	0.10425E-02	0.000	17.019
6	75.000	0.10171E+01	0.10165E-02	1.710	21.569
7	10.000	0.00000E+00	0.00000E+00	-100.000	0.000
7	15.000	0.00000E+00	0.00000E+00	-100.000	0.000
7	25.000	0.00000E+00	0.00000E+00	-100.000	0.000
7	37.500	0.98890E+00	0.14448E-02	-1.110	16.179
7	50.000	0.10000E+01	0.14546E-02	0.000	19.352
7	75.000	0.10061E+01	0.89936E-03	0.607	17.856
8	10.000	0.92752E+00	0.25082E-02	-7.248	12.713
8	15.000	0.95709E+00	0.18609E-02	-4.291	16.737
8	25.000	0.97401E+00	0.16020E-02	-2.599	19.092
8	37.500	0.99350E+00	0.11135E-02	-0.650	18.595
8	50.000	0.10000E+01	0.89401E-03	0.000	17.701
8	75.000	0.10137E+01	0.68525E-03	1.370	19.310
9	10.000	0.89729E+00	0.16428E-01	-10.271	50.472
9	15.000	0.93287E+00	0.20538E-02	-6.713	22.672
9	25.000	0.95878E+00	0.36070E-02	-4.122	37.290
9	37.500	0.97806E+00	0.19845E-02	-2.194	29.509
9	50.000	0.10000E+01	0.11244E-02	0.000	28.799
9	75.000	0.10036E+01	0.12437E-02	0.357	34.495

Table [2.16]

Tower	Z cut only	EM + f*HAD	HAD>2GeV cut
0	0.184	0.156	0.148
1	0.141	0.141	0.134
2	0.163	0.141	0.134
3	0.163	0.148	0.120
4	0.170	0.163	0.148
5	0.156	0.156	0.141

Table [2.17]

PARAMETERS IN RESPONSE FUNCTION S(X,Z')

Parameter	Tower 0	Tower 1	Tower 2	Tower 3	Tower 4
p_1	1.00±0.001	1.00±0.001	0.998±0.001	1.00±0.001	0.999±0.001
p_2 ($\times 10^{-5}$)	1.71±0.77	3.43±3.40	0.106±0.124	9.36±7.50	14.6±21.5
p_3	-0.790±0.020	0.587±0.087	0.923±0.100	0.496±0.068	0.425±0.128
p_4 ($\times 10^{-3}$)	1.83±1.17	-0.832±0.087	-0.941±0.099	-0.357±0.090	-0.529±0.107
p_5 ($\times 10^{-4}$)	-5.52±0.04	0.00	0.00	0.00	0.00
p_6	44.7±0.4	48.5±0.5	47.7±0.5	45.7±0.4	41.6±0.3
p_7	1.00	1.00	1.00	1.00	1.00
p_8 ($\times 10^{-2}$)	1.170±0.08	0.146±0.059	0.196±0.062	0.586±0.054	1.140±0.064
p_9 ($\times 10^{-3}$)	0.721 ($\times 10^{-8}$)	0.349±0.066	0.097±0.067	0.722±0.062	1.69±0.07
p_{10}	3.08±.11$\times 10^{-26}$	3.06±.09$\times 10^{-26}$	4.25±3.59$\times 10^{-19}$	1.39±.03$\times 10^{-18}$	5.72±.22$\times 10^{-13}$
p_{11}	2.491±.001	2.490±.001	1.782±.036	1.737±.001	1.196±.002
p_{12} ($\times 10^{-3}$)	-1.68±0.21	-0.164±0.093	-1.28±0.13	0.876±0.067	-0.374±0.122

Parameter	Tower 5	Tower 6	Tower 7	Tower 8	Tower 9
p_1	0.998±0.001	0.999±0.001	1.00±0.002	1.00±0.01	1.00±0.001
p_2 ($\times 10^{-5}$)	3.15±0.58	33.9±27.5	114±117	45.8±40.1	589±7.8
p_3	0.539±0.008	0.406±0.072	0.287±0.094	0.364±0.077	0.350±0.0003
p_4 ($\times 10^{-3}$)	-0.369±0.123	-1.17±0.13	-1.16±0.16	-0.555±0.115	-4.66±0.26
p_5 ($\times 10^{-7}$)	0.00	0.00	0.00	0.00	-3.01±2.33
p_6	43.0±0.3	48.2±0.5	46.0±0.5	49.9±0.5	50.9±0.9
p_7	1.00	1.00	1.00	1.00	1.00
p_8 ($\times 10^{-2}$)	1.13±0.06	0.645±0.07	-0.431±0.07	0.956±0.08	-10.6±0.6
p_9 ($\times 10^{-3}$)	1.17±0.07	0.125±0.08	1.69 ($\times 10^{-10}$)	0.054±0.09	12.5±1.0
p_{10} ($\times 10^{-13}$)	5.72±.25	5.72±.22	5.72±3.04	5.71±2.89	5.66±2.76
p_{11}	1.199±.002	1.190±.002	1.212±.023	1.212±.022	1.212±.021
p_{12} ($\times 10^{-3}$)	-0.145±0.124	0.396±0.149	-0.123±0.121	-0.502±0.168	6.46±0.28

Note: Values of p_{10} and p_{11} are replaced to 3.96$\times 10^{-4}$ and 0.384 for $|x| \geq 23.5$ cm, respectively.

Table [3.1]

Trigger name	Et tower threshold (GeV)/ΣEt(GeV)					∫L (nb-1)
	CEM	CHA	CEM+CHA	PEM	FEM	
Low	1/10	1/10	1/10	1/10	1/10	0.165
Medium	1/30	1/30	1/30	1/30	1/30	12.54
High	1/40	1/40	1/40	1/40	1/40	6.76
Burn	1/45	1/45	1/45	1/45	1/45	4.74

Table [3.2] Summary of fit

	χ^2 /DOF straight line	χ^2 /DOF quadrature
30 <P_t^{parton} <60GeV/c	26.7	32.4
70 <P_t^{parton} <250GeV/c	3.23	3.12
30 <P_t^{parton} <70GeV/c	18.9	27.0
80 <P_t^{parton} <250GeV/c	2.2	2.5
30 <P_t^{parton} <80GeV/c	15.9	20.9
90 <P_t^{parton} <250GeV/c	2.3	2.4
30 <P_t^{parton} <90GeV/c	14.2	17.2
100 <P_t^{parton} <250GeV/c	2.6	3.0
30 <P_t^{parton} <100GeV/c	14.2	14.3
125 <P_t^{parton} <250GeV/c	2.2	2.7
30 <P_t^{parton} <125GeV/c	16.8	10.3
150 <P_t^{parton} <250GeV/c	3.2	2.7

Table [3.3] Summary of Isolated π^0/γ + jet events

π^0/γ Pt (GeV/c)	Away jet Pt (GeV /c)	σ(Pt) (GeV /c)	$\sigma/\sqrt{Pt}$	Number of events
16.7	13.8	3.8	1.02	54
19.9	16.4	4.1	1.01	17
23.7	18.0	1.2	0.28	14
26.9	15.7	5.6	1.41	7
30.5	26	6.5	1.27	3
34.2	26	5.1	1.00	5
37.8	22	8	1.71	2
45.0	34	5.8		1
47.3	30	5.5		1
53.8	46	6.8		1
70.4	74	8.6		1

Table [4.1] Inclusive jet cross section

a	b	c	d	e	f	g	h	i	j
40	45	5.7	3154	1.08	52.0	20.34	±0.36	±8.4	±8.4
45	50	5.7	1824	1.08	57.7	11.83	±0.28	±4.6	±4.6
50	55	5.7	1111	1.09	63.4	7.24	±0.22	±2.7	±2.7
55	60	5.7	670	1.09	69.2	4.38	±0.17	±1.6	±1.6
60	65	5.7	406	1.10	74.9	2.67	±0.13	±1.0	±1.0
65	70	5.7	237	1.10	80.7	1.57	±0.10	±0.63	±0.64
70	75	5.7	192	1.11	86.4	1.28	±0.092	±0.44	±0.45
75	80	5.7	109	1.11	92.1	0.727	±0.070	±0.29	±0.30
80	85	5.7	62	1.12	97.9	0.416	±0.053	±0.20	±0.20
85	90	5.3	49	1.12	103.4	0.356	±0.051	±0.15	±0.16
90	95	5.3	42	1.13	108.7	0.306	±0.047	±0.11	±0.12
95	100	5.3	26	1.13	114.0	0.190	±0.037	±0.080	±0.088
100	105	5.3	22	1.13	119.4	0.161	±0.034	±0.062	±0.071
105	110	5.3	15	1.14	124.7	0.110	±0.029	±0.045	±0.054
110	120	10.6	16	1.14	132.3	0.059	±0.015	±0.029	±0.033
120	130	10.6	13	1.15	142.7	0.048	±0.013	±0.018	±0.023
130	140	10.6	13	1.16	153.7	0.049	±0.014	±0.013	±0.019
140	160	21.3	14	1.17	169.5	0.026	±0.0071	±0.0065	±0.0096
160	180	21.3	7	1.18	190.0	0.013	+0.0072 -0.0049	±0.0030	+0.0078 -0.0058
180	200	21.3	3	1.19	211.6	0.0058	+0.0056 -0.0031	±0.0013	+0.0058 -0.0034
200	240	42.6	2	1.20	236.4	0.0019	+0.0026 -0.0012	±0.0005	+0.0026 -0.0013

a) Lower bound of bin for the raw data filling.

b) Upper bound of bin for the raw data filling.

c) Corrected bin width.(GeV/c)

d) Number of jets in bins.

e) Correction factor due to the acceptance.

f) Corrected Pt for the bin (GeV/c)

g) Inclusive jet cross section. (nb/(GeV/c))

h) Statistical errors of g).

i) Systematic errors of g)

j) Quadratic sum of h) and i).

Table [4.2] Systematic Errors in Inclusive Jet Cross Section

Jet energy uncertainly

Pt(GeV/c)	error by fragmenta-correction	error by geometrical correction	error by non-linear correction	sum of error (%) correction to	sum of correction Pt (GeV/c)	effect to the cross-section (%)
50	0.011	0.037	0.075	0.084	4.20	44
75	0.007	0.035	0.055	0.066	4.92	37
100	0.012	0.020	0.055	0.060	5.96	36
150	0.005	0.024	0.047	0.053	7.95	36
200	0.005	0.022	0.037	0.043	8.52	32
250	0.007	0.022	0.025	0.034	8.39	28

Trigger efficiency uncertainty

<0.5%

Uncertainty of corrections for analysis cut, geometrical acceptance and energy resolution

EM fraction cut	0.5%
z vertex cut	2%
geometrical acceptance	7%
energy resolution	7%
Quadratic sum of above items	10%

Uncertainty of luminosity measurement

15%

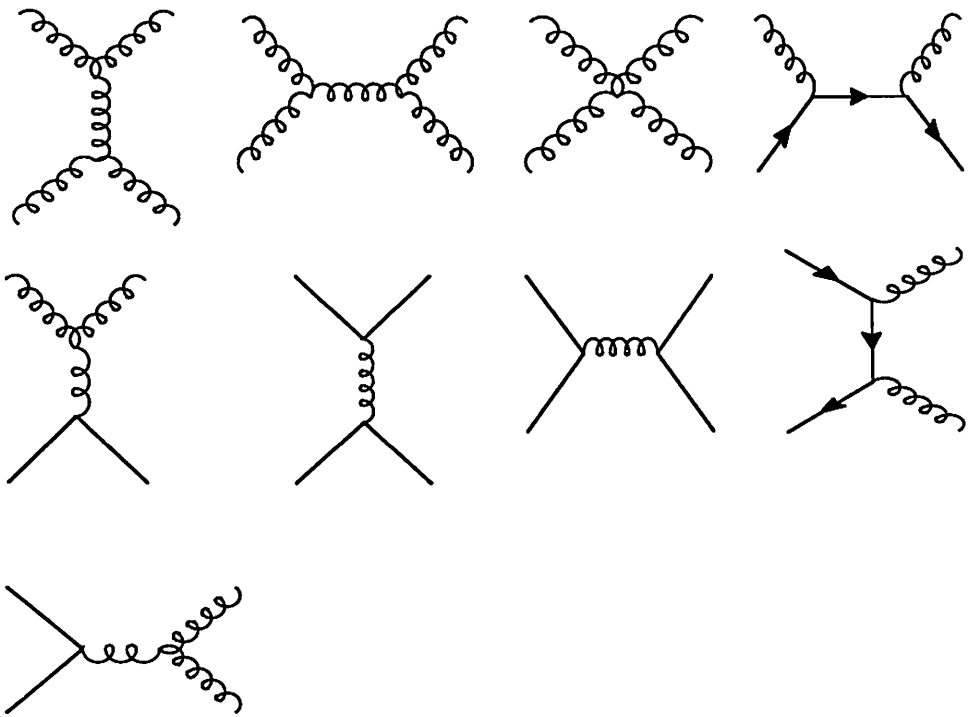

Fig.[1. 1]

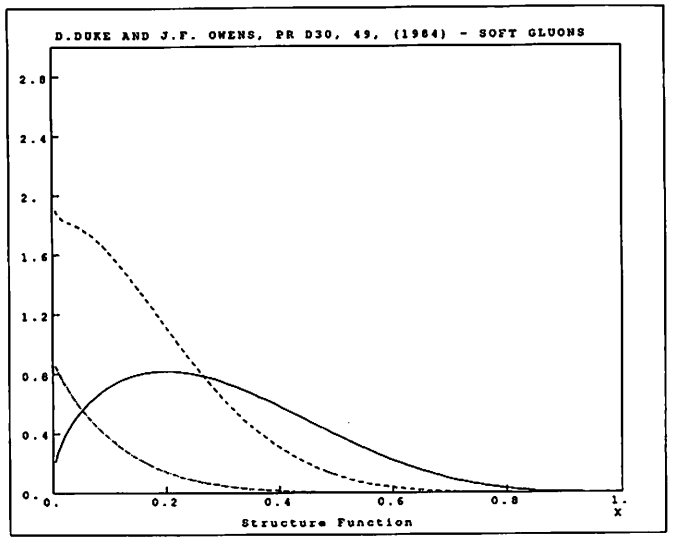

Fig.[1.2a]

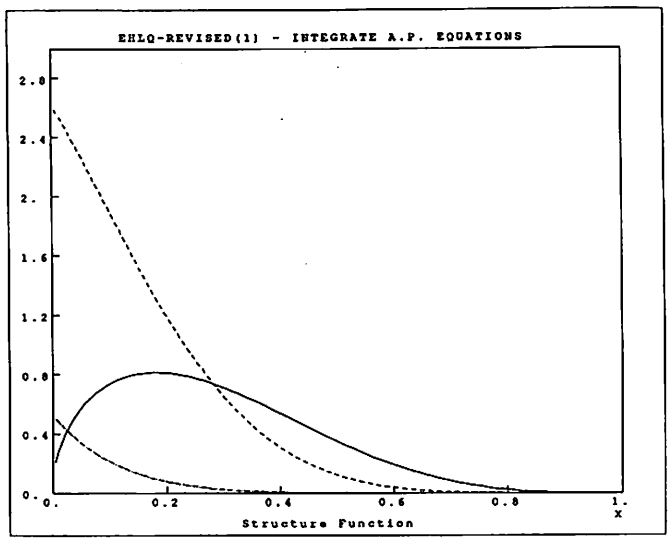

Fig.[1.2b]

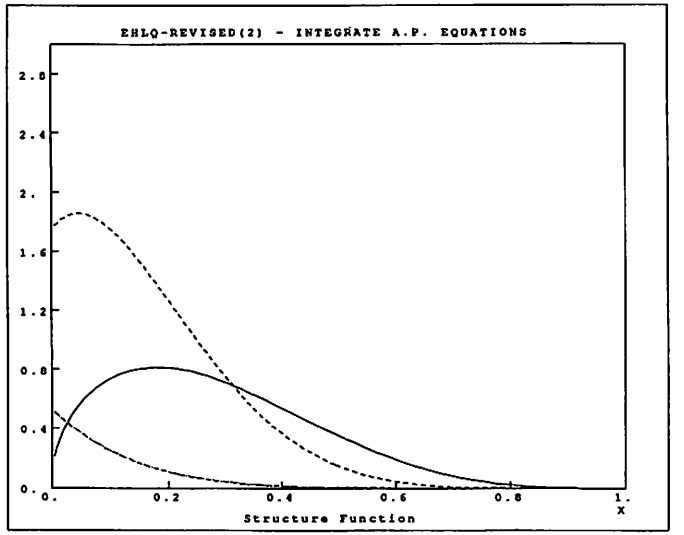

Fig.[1.2c]

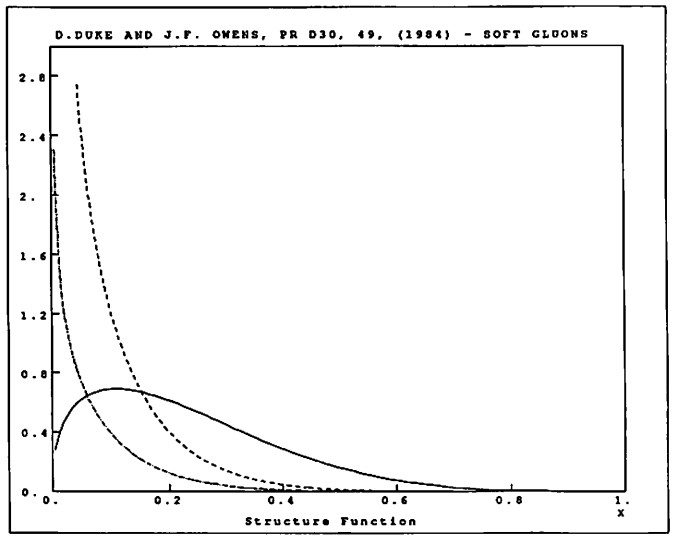

Fig.[1.2d]

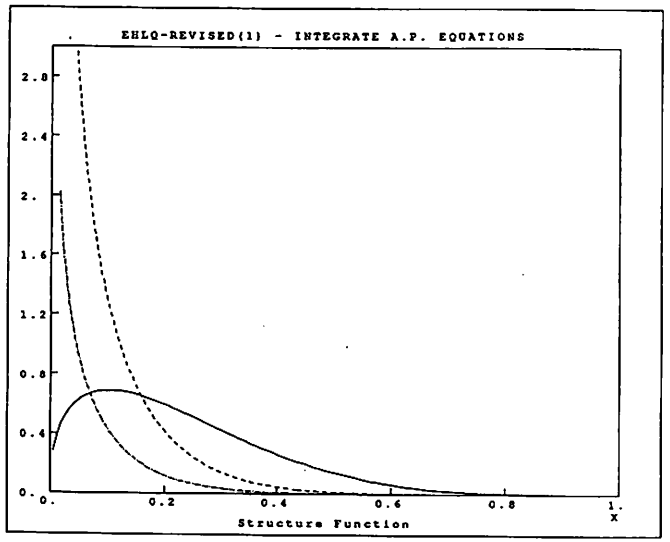

Fig.[1.2e]

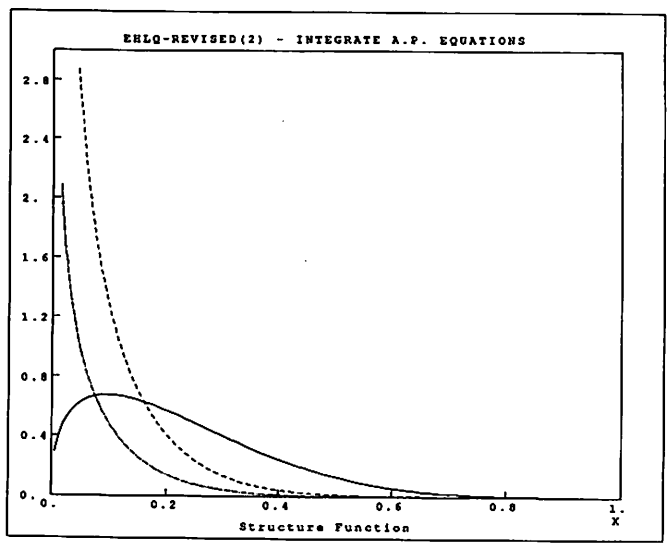

Fig.[1.2f]

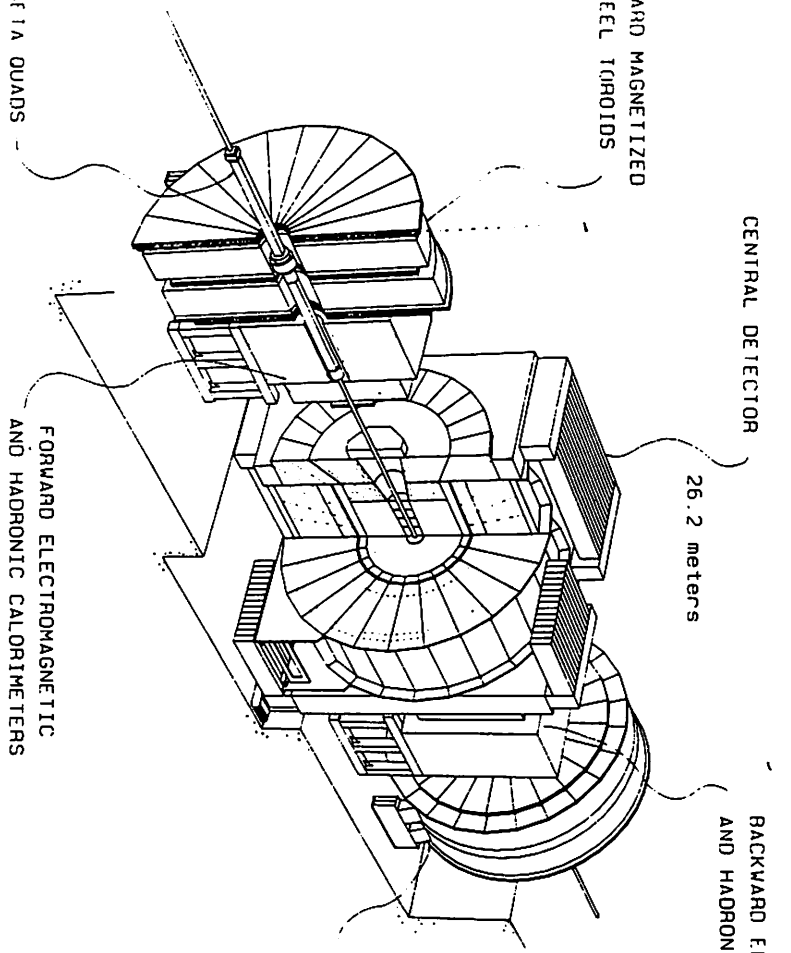

Fig.[2. 1]

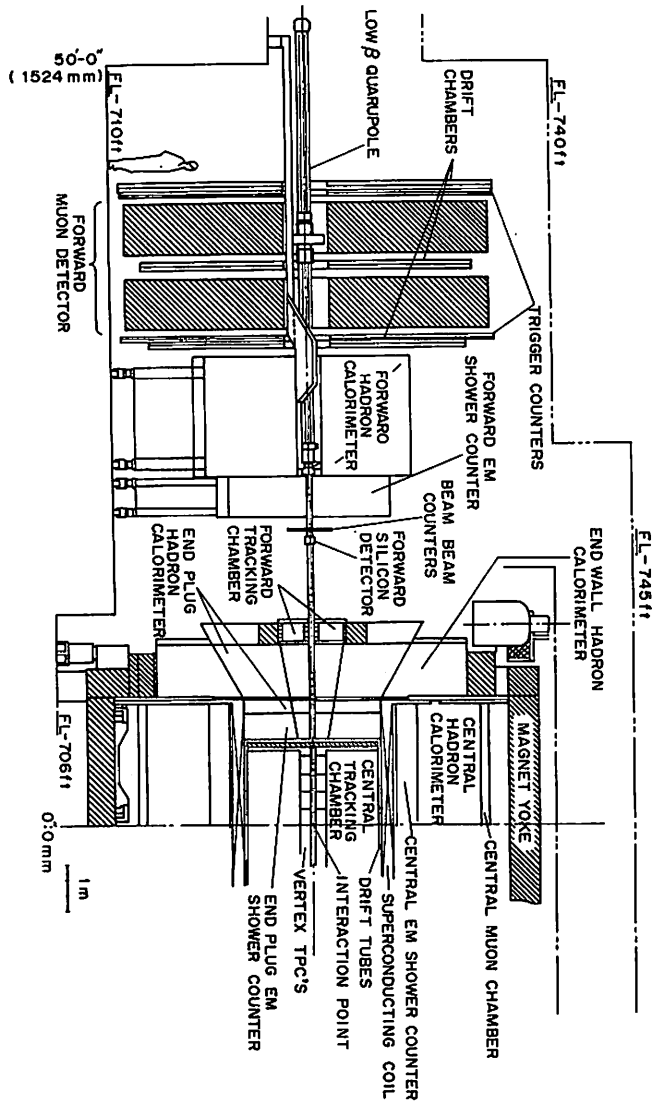
50'-0"
(1524 mm)
FL-710ft
FORWARD MUON DETECTOR
LOW β QUADRUPOLE
DRIFT CHAMBERS
FL-740ft
TRIGGER COUNTERS
FORWARD HADRON CALORIMETER
FORWARD EM SHOWER COUNTER
BEAM BEAM COUNTERS
FORWARD SILICON DETECTOR
FORWARD TRACKING CHAMBER
END PLUG HADRON CALORIMETER
FL-745ft
END WALL HADRON CALORIMETER
FL-706ft
0'0mm
1m
CENTRAL HADRON CALORIMETER
MAGNET YOKE
CENTRAL MUON CHAMBER
CENTRAL TRACKING CHAMBER
CENTRAL EM SHOWER COUNTER
SUPERCONDUCTING COIL
DRIFT TUBES
INTERACTION POINT
VERTEX TPC'S
END PLUG EM SHOWER COUNTER

Fig.[2. 2]

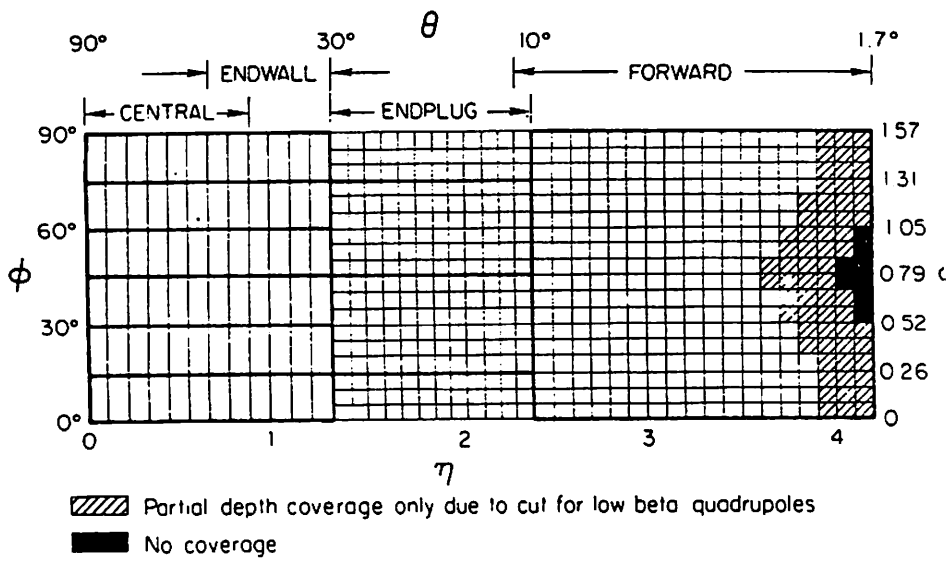
θ
90°
30°
10°
1.7°
ENDWALL
FORWARD
CENTRAL
ENDPLUG
90°
60°
30°
0°
φ
0
1
2
3
4
η
1 57
1 31
1 05
0 79
0 52
0 26
0
Partial depth coverage only due to cut for low beta quadrupoles
No coverage

Fig.[2. 3]

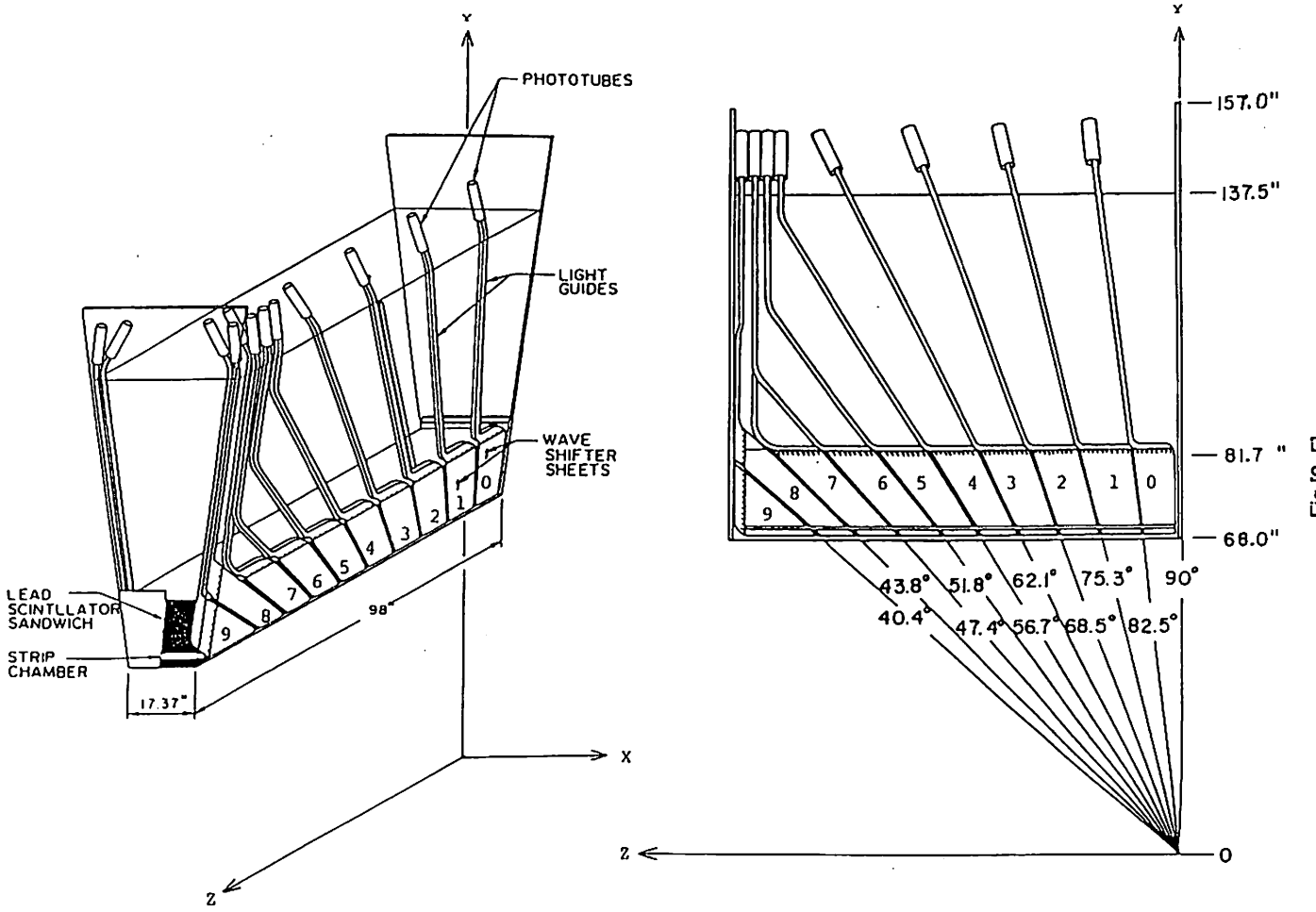
Y
PHOTOTUBES
LIGHT GUIDES
WAVE SHIFTER SHEETS
LEAD SCINTLLATOR SANDWICH
STRIP CHAMBER
17.37"
98"
X
Z
157.0"
137.5"
81.7 "
68.0"
43.8°
51.8°
62.1°
75.3°
90°
40.4°
47.4°
56.7°
68.5°
82.5°
0

Fig.[2. 5]

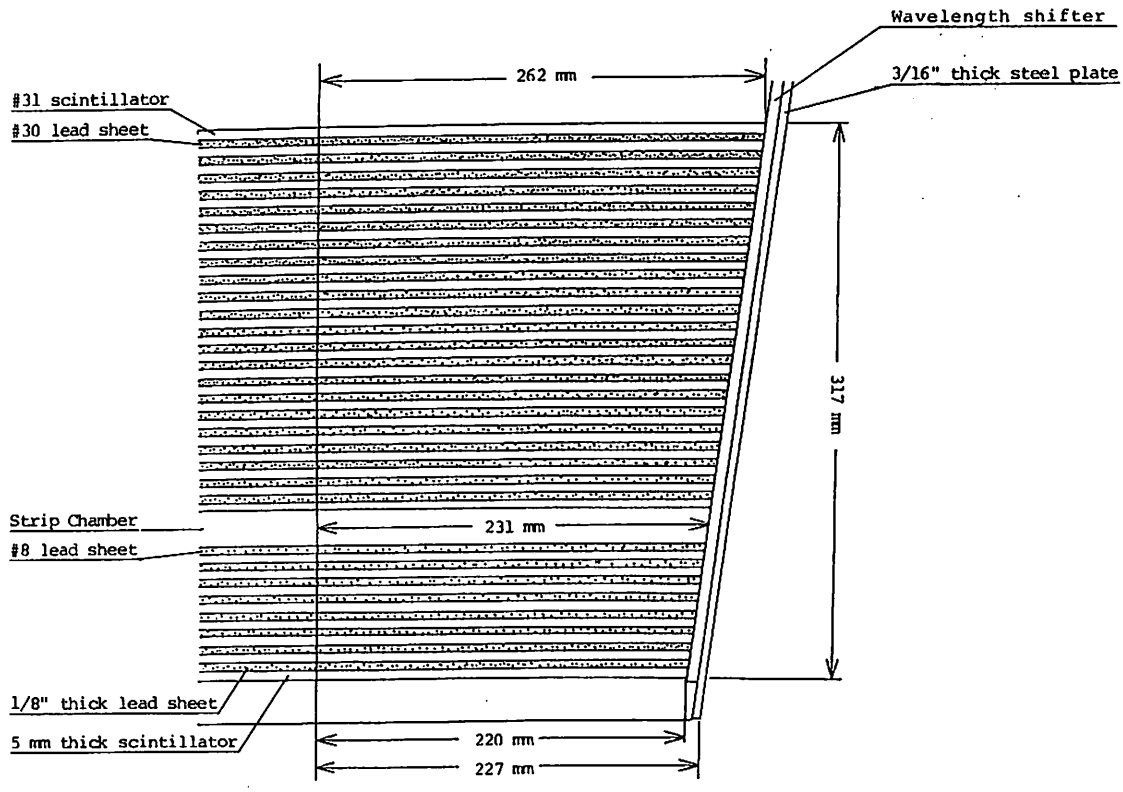
Wavelength shifter
3/16" thick steel plate
262 mm
#31 scintillator
#30 lead sheet
317 mm
Strip Chamber
231 mm
#8 lead sheet
1/8" thick lead sheet
5 mm thick scintillator
220 mm
227 mm

Fig.[2. 4]

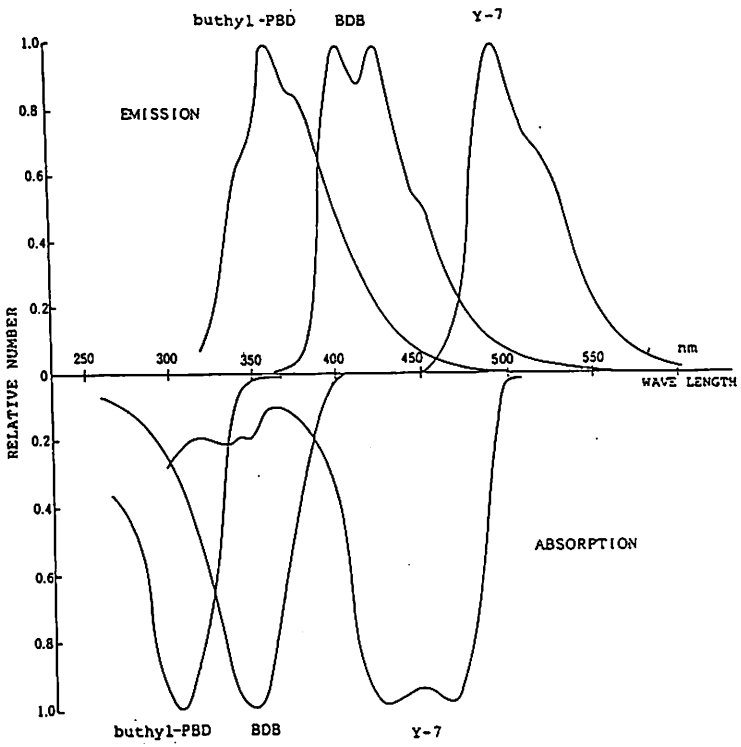
buthyl-PBD
BDB
Y-7
EMISSION
RELATIVE NUMBER
1.0
0.8
0.6
0.4
0.2
0
250
300
350
400
450
500
550
nm
WAVE LENGTH
ABSORPTION
buthyl-PBD
BDB
Y-7

Fig.[2. 6]

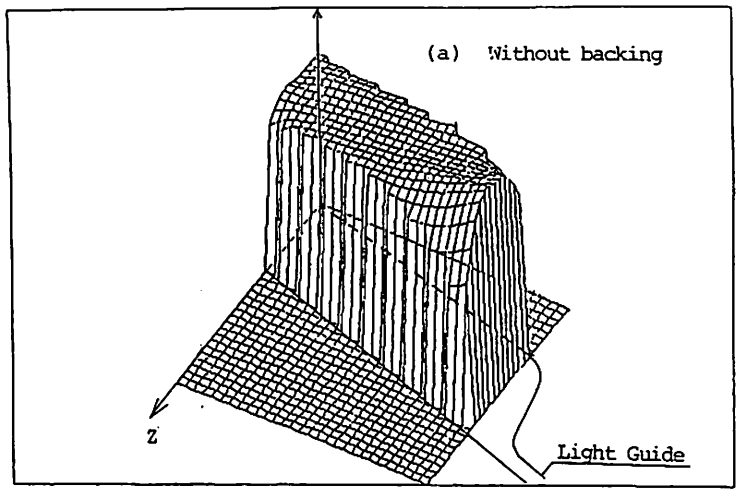
(a) Without backing
Z
Light Guide

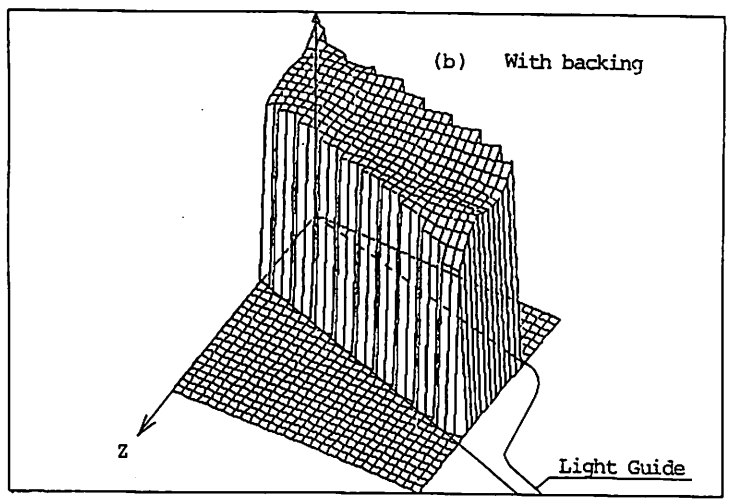
(b) With backing
Z
Light Guide

Fig.[2. 7]

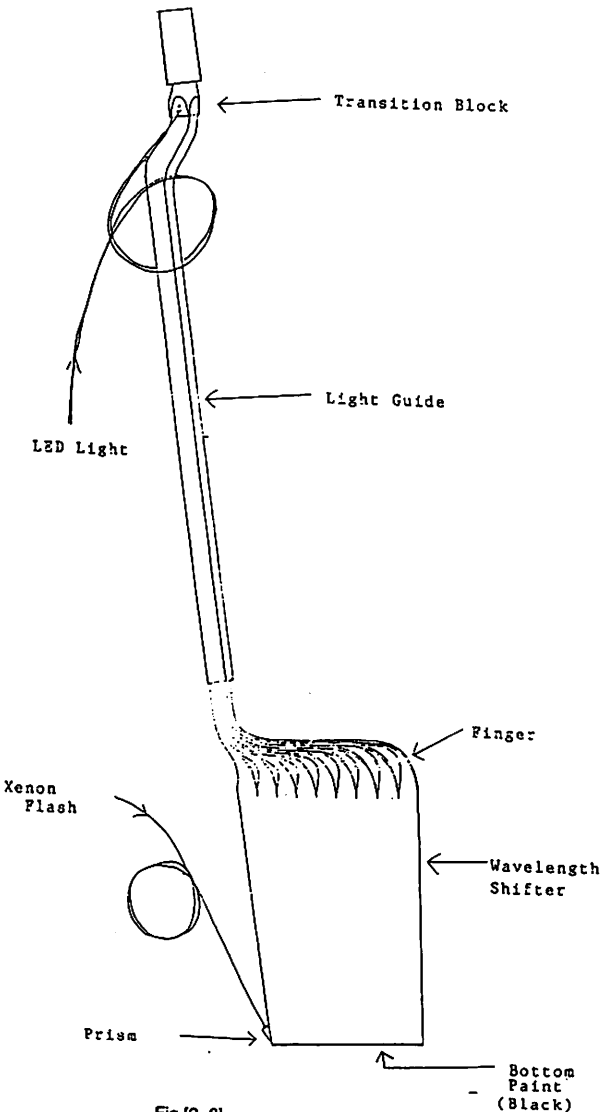
Transition Block
Light Guide
LED Light
Finger
Xenon Flash
Wavelength Shifter
Prism
Bottom Paint (Black)

Fig.[2. 8]

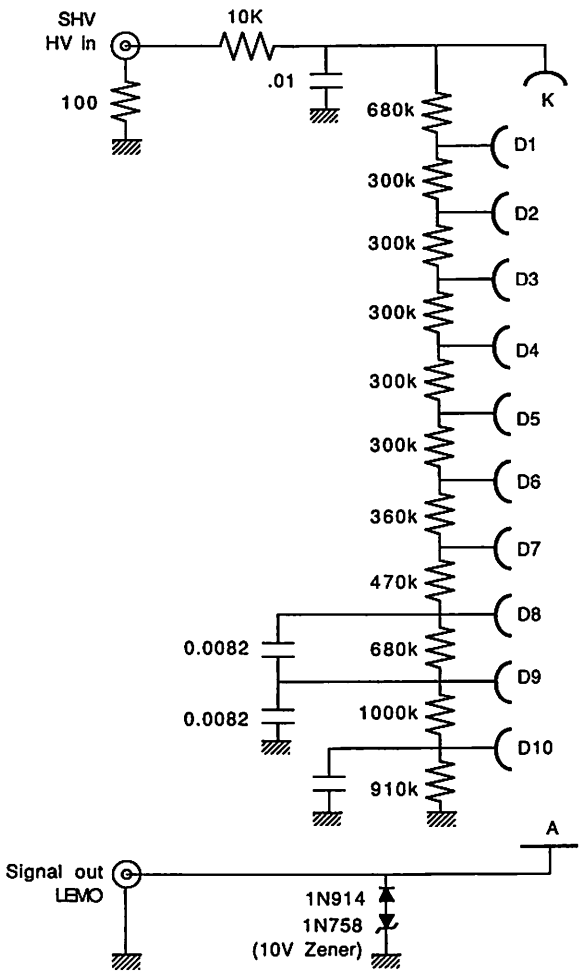
SHV
HV In
10K
.01
100
680k
K
D1
300k
D2
300k
D3
300k
D4
300k
D5
300k
D6
360k
D7
470k
D8
0.0082
680k
D9
0.0082
1000k
D10
910k
A
Signal out
LEMO
1N914
1N758
(10V Zener)

Fig.[2. 9]

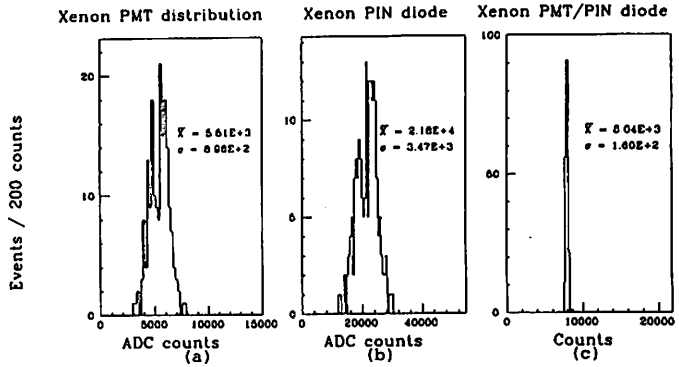

Fig.[2.10]

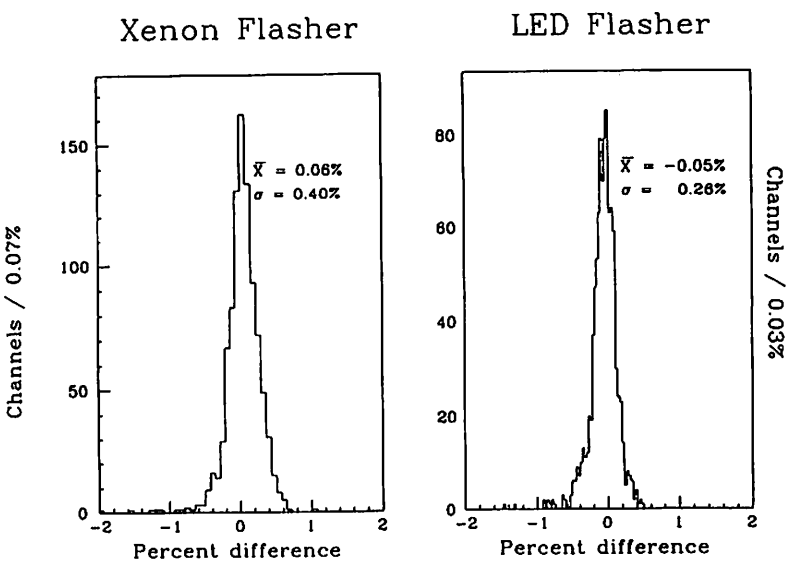

Fig.[2.11]

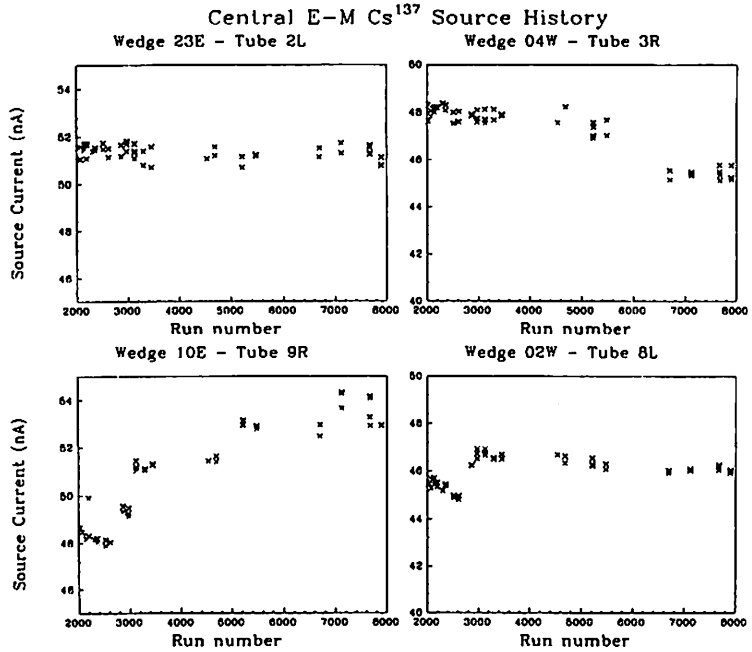

Fig.[2.12]

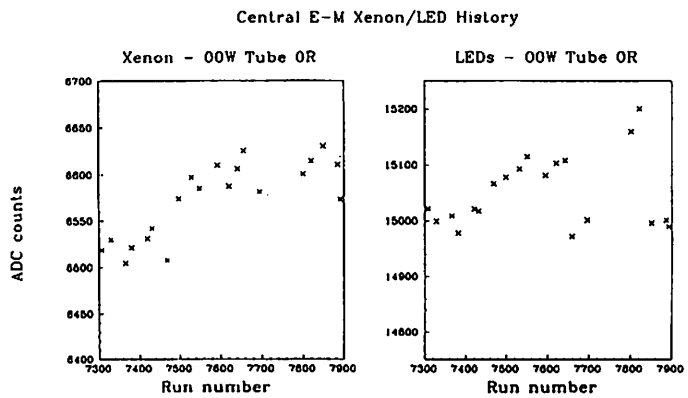

Fig.[2.13]

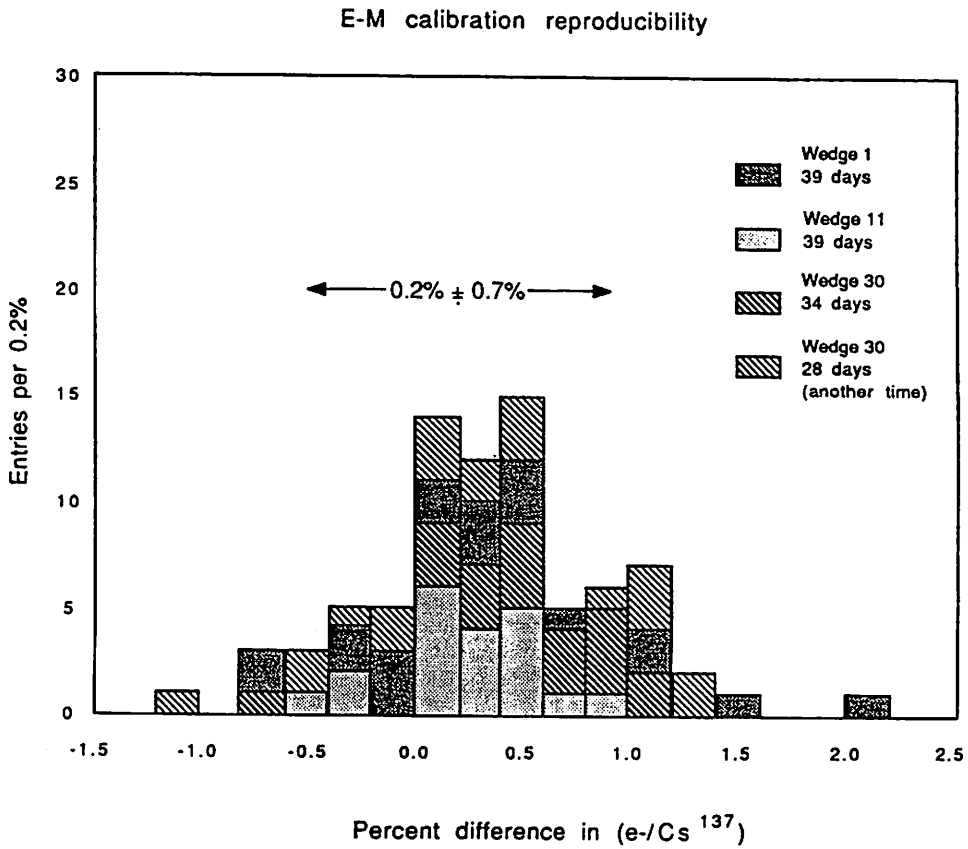

Fig.[2.14]

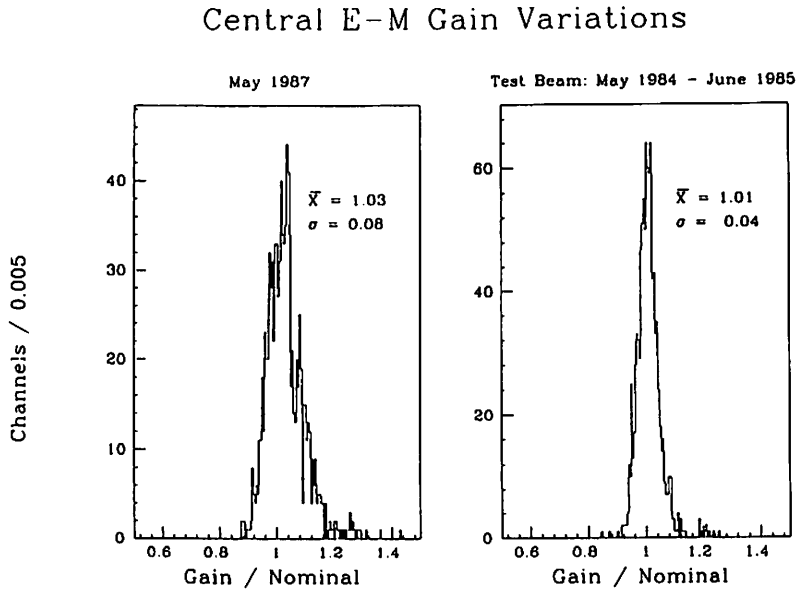

Fig.[2.15]

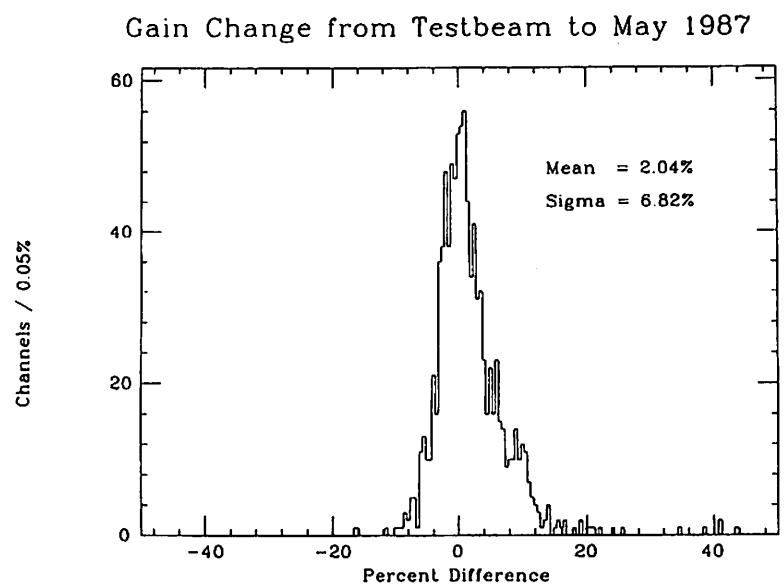

Fig.[2.16]

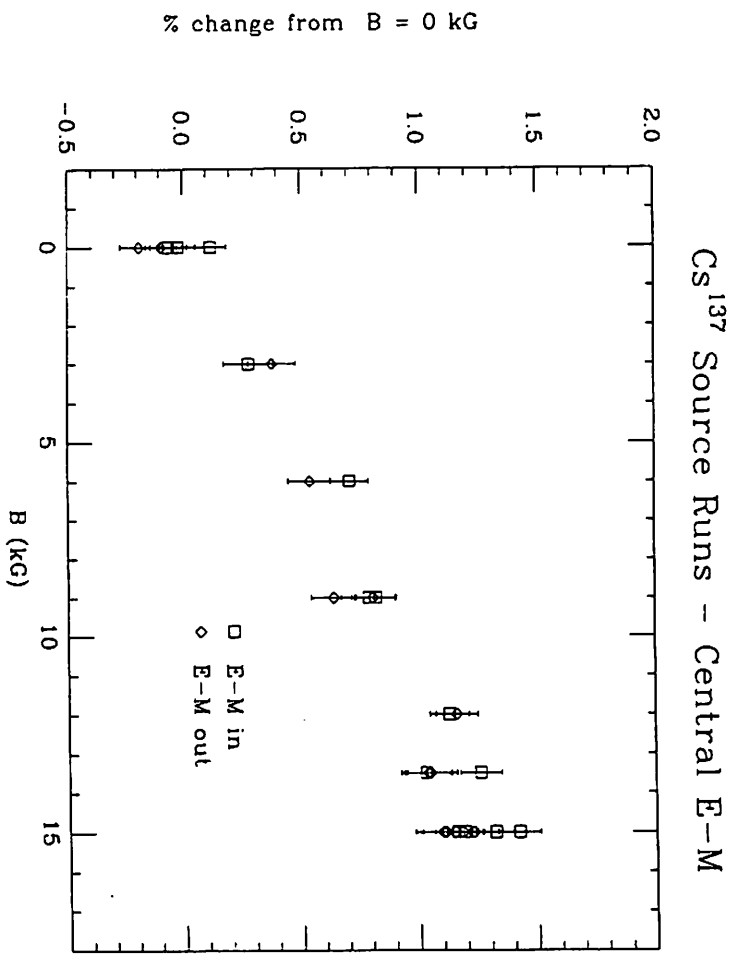

Fig.[2.17]

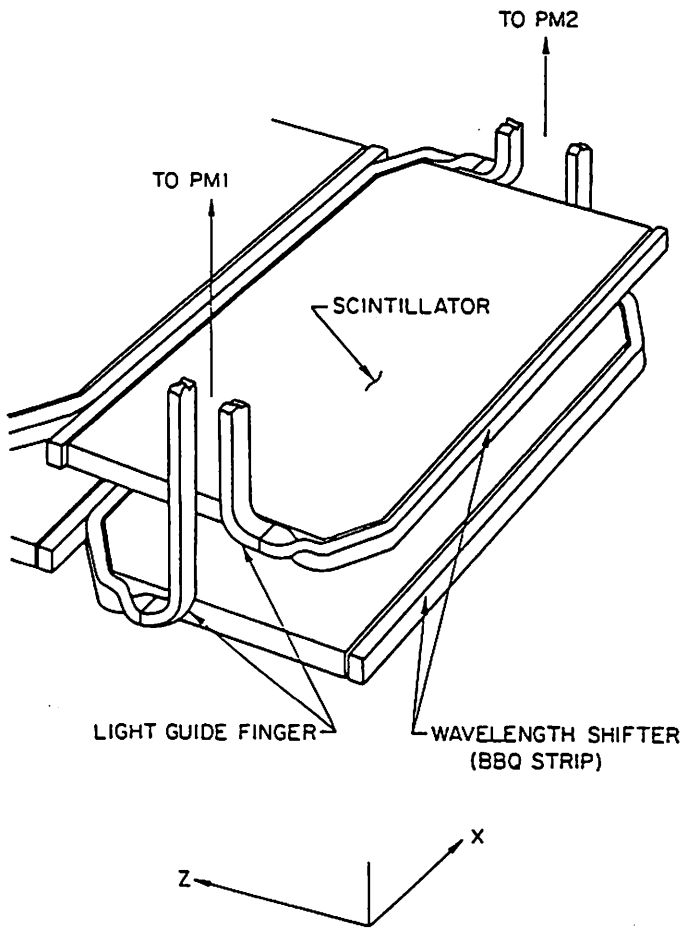

Fig.[2.18]

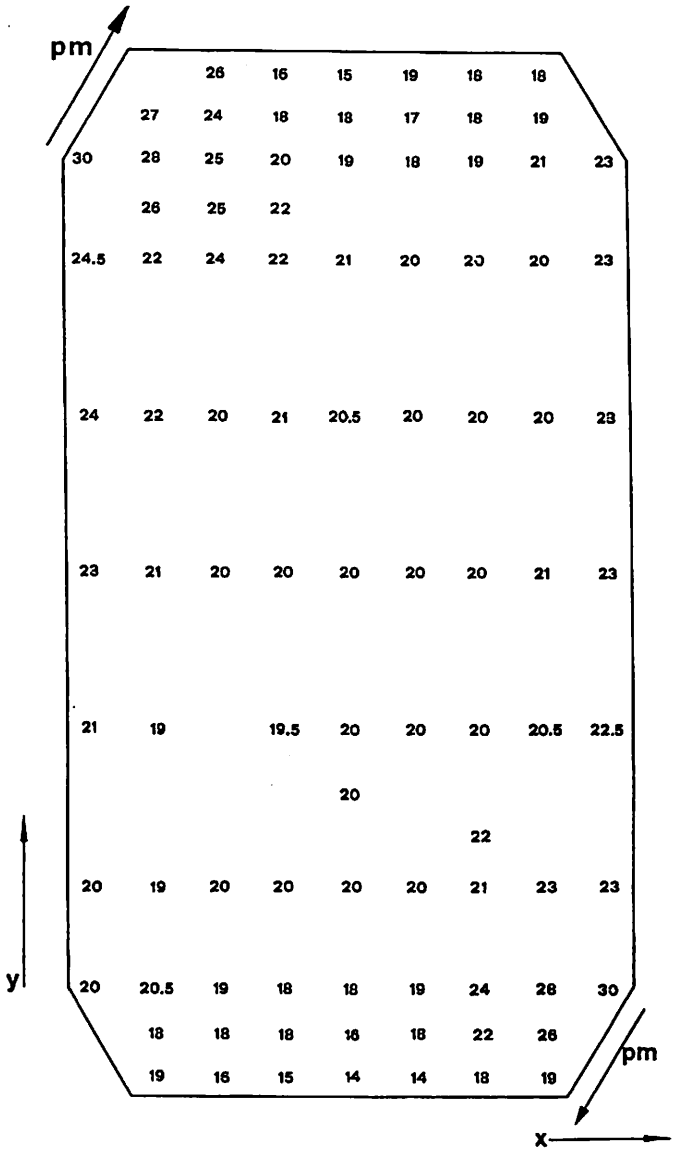

Fig.[2.19]

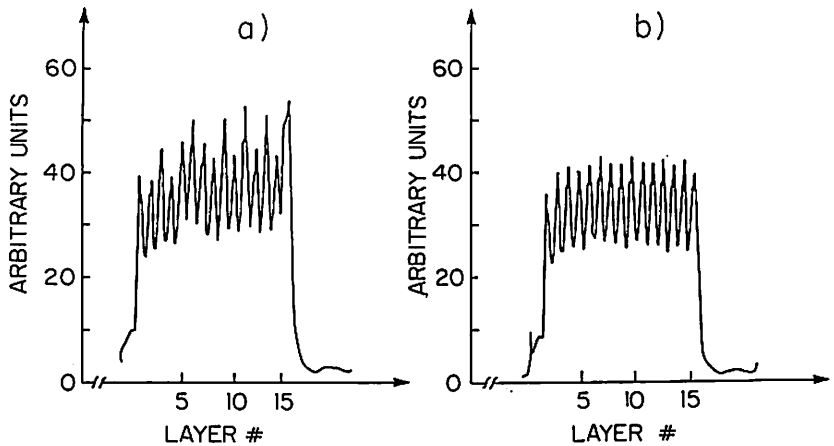

Fig.[2.20]

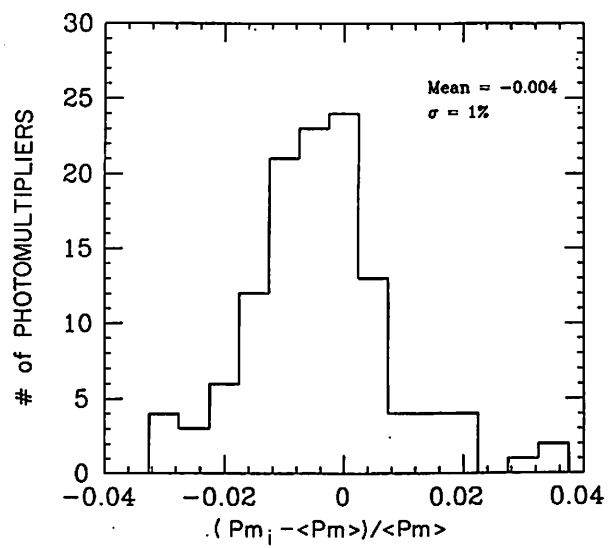

Fig.[2.21]

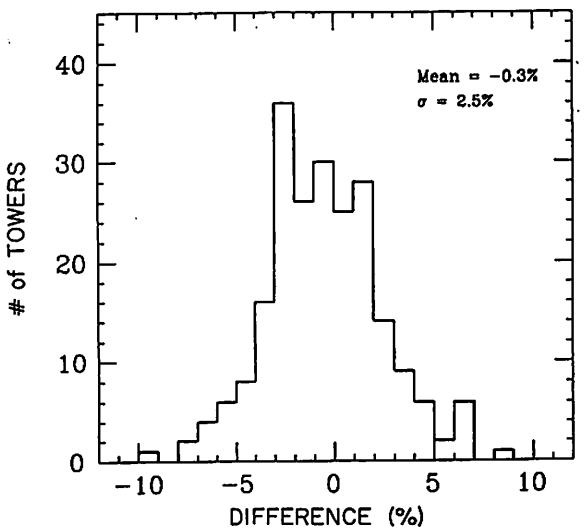

Fig.[2.22]

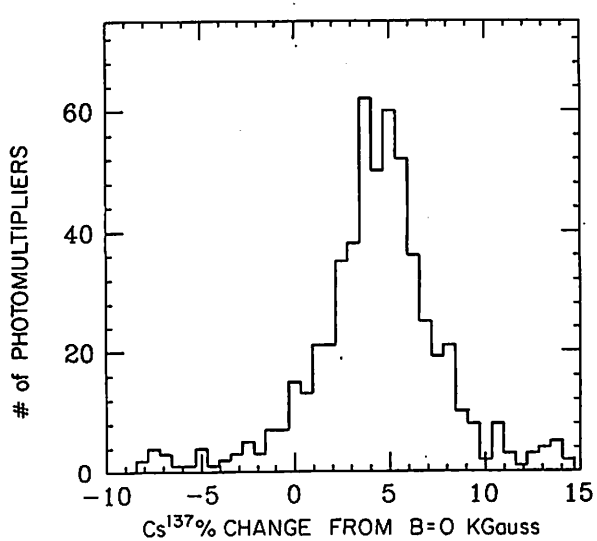

Fig.[2.23]

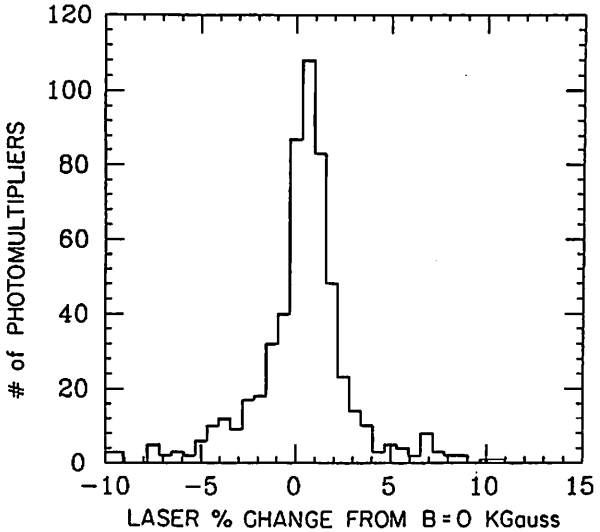

Fig.[2.24]

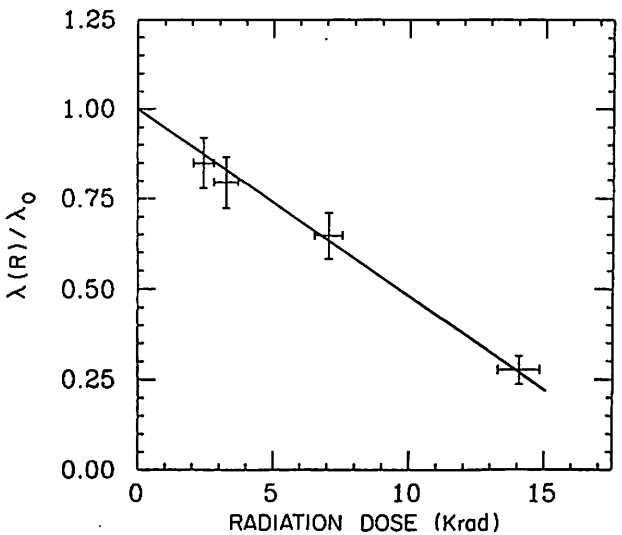

Fig.[2.25]

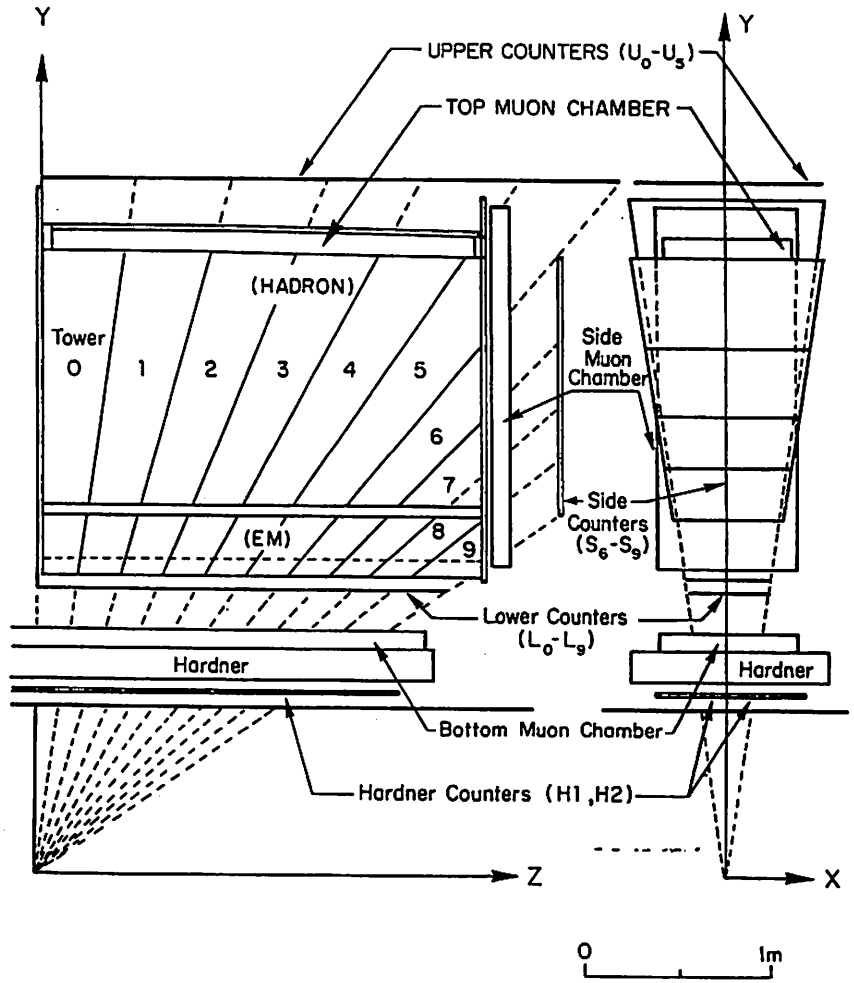

Fig.[2.26]

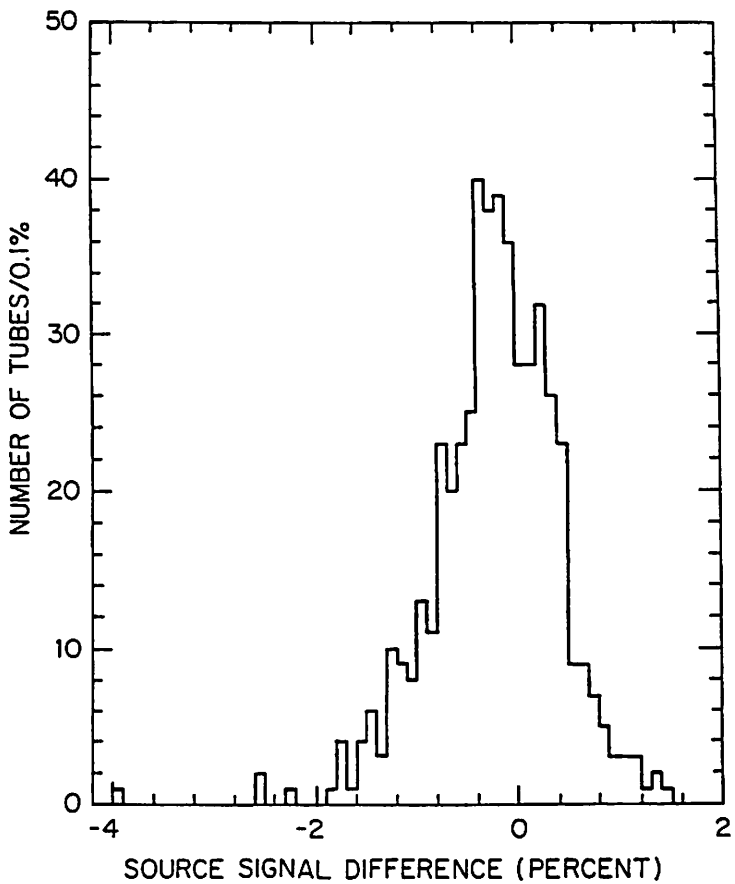

Fig.[2.27]

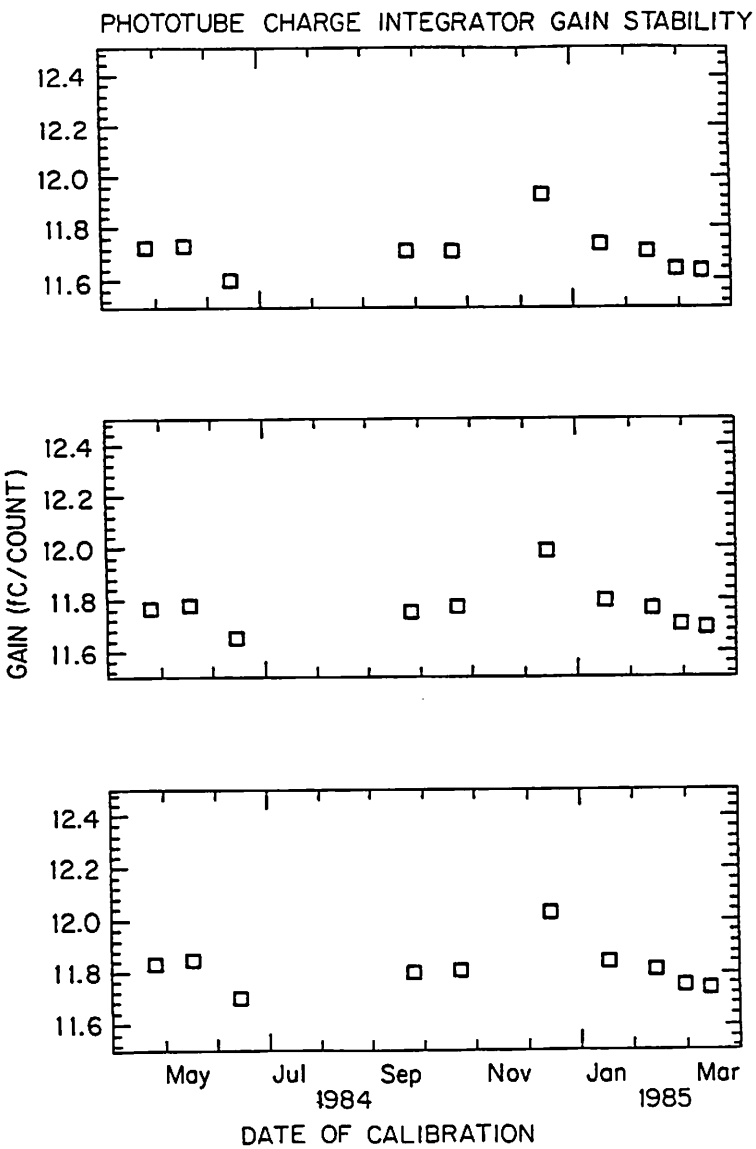

Fig.[2.28a]

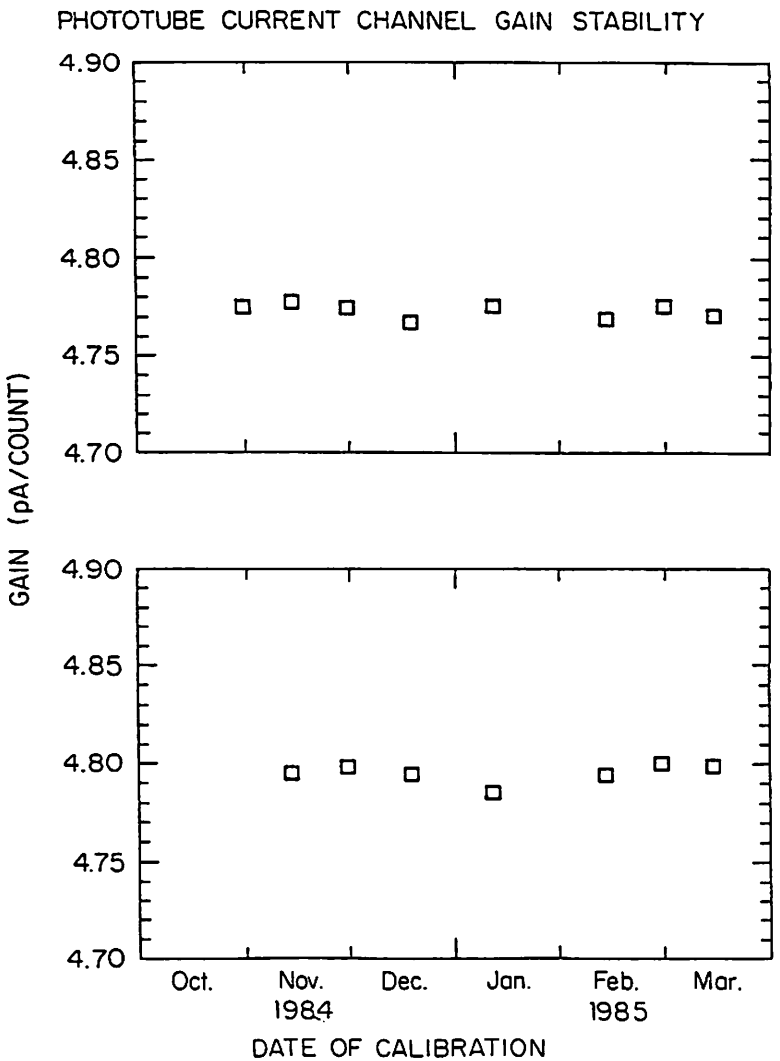

Fig.[2.28b]

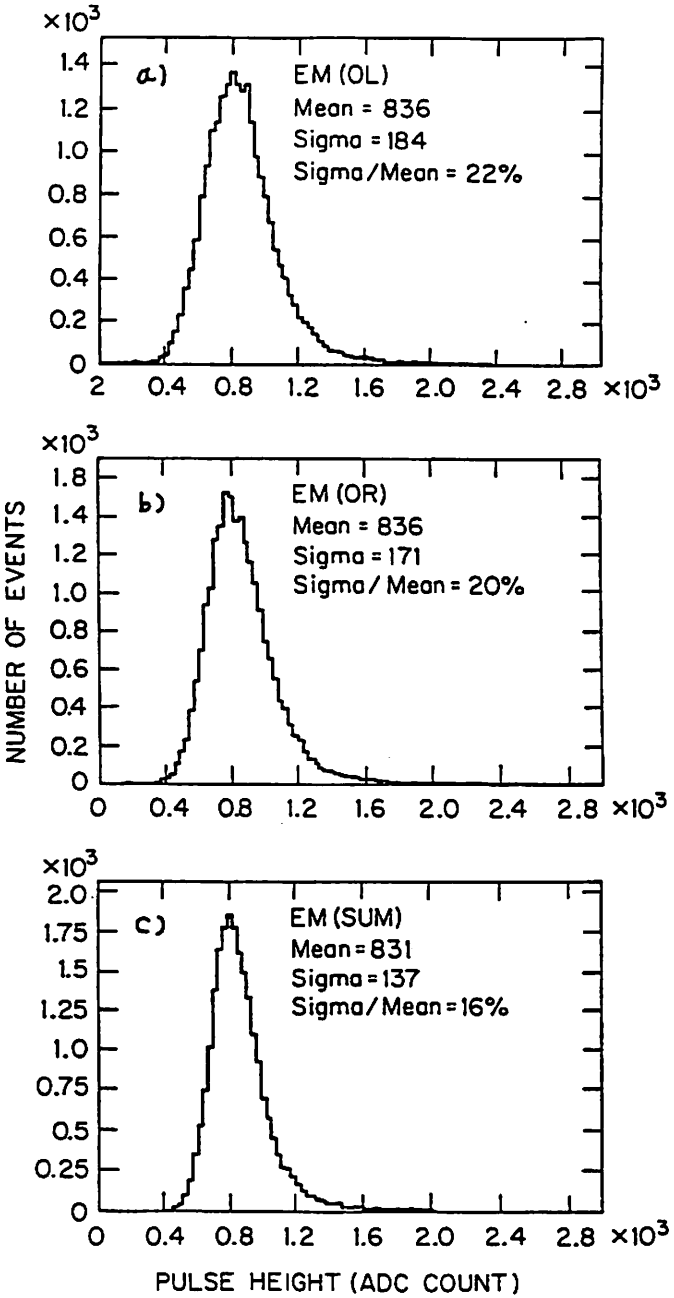

Fig.[2.29]

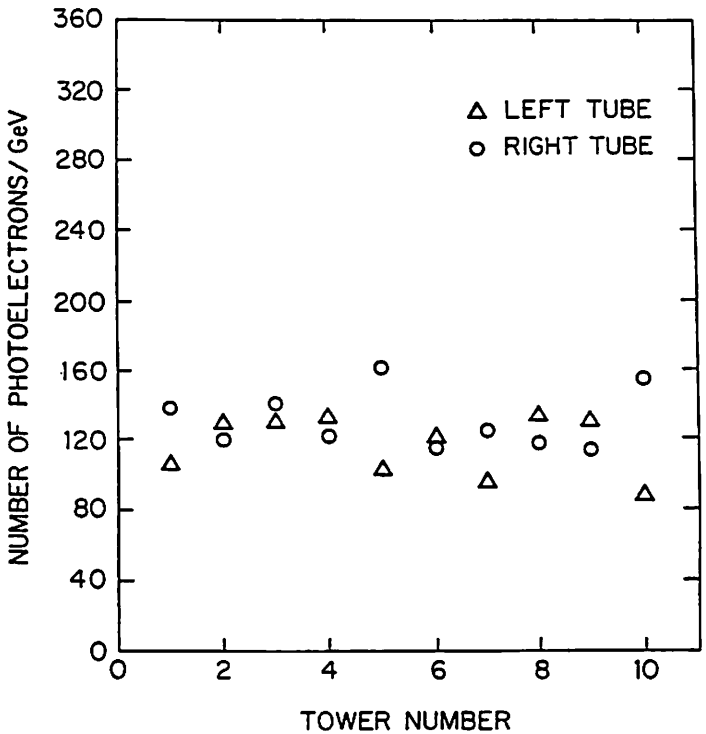

Fig.[2.30]

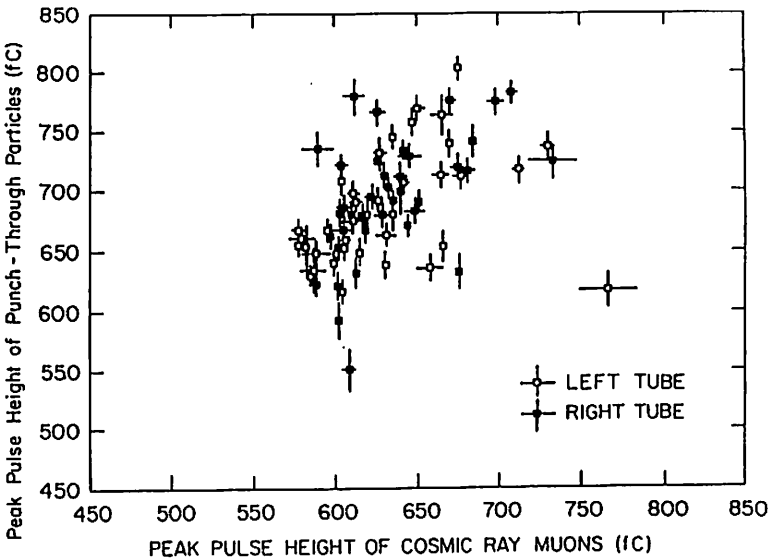

Fig.[2.31]

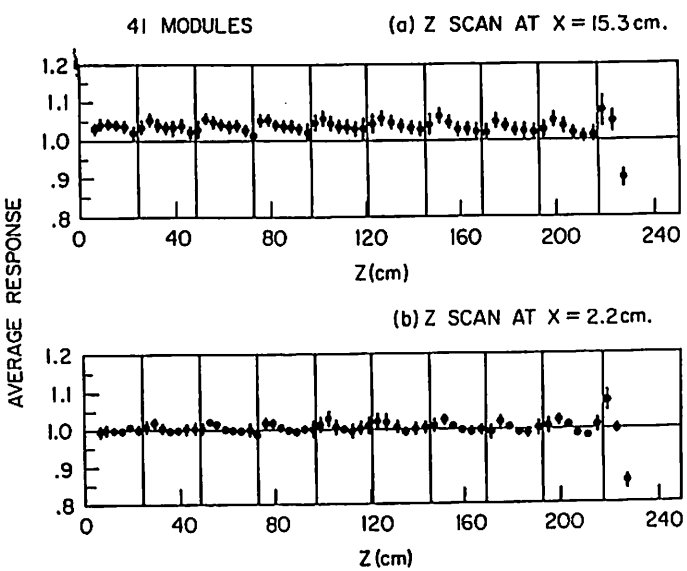

Fig.[2.32]

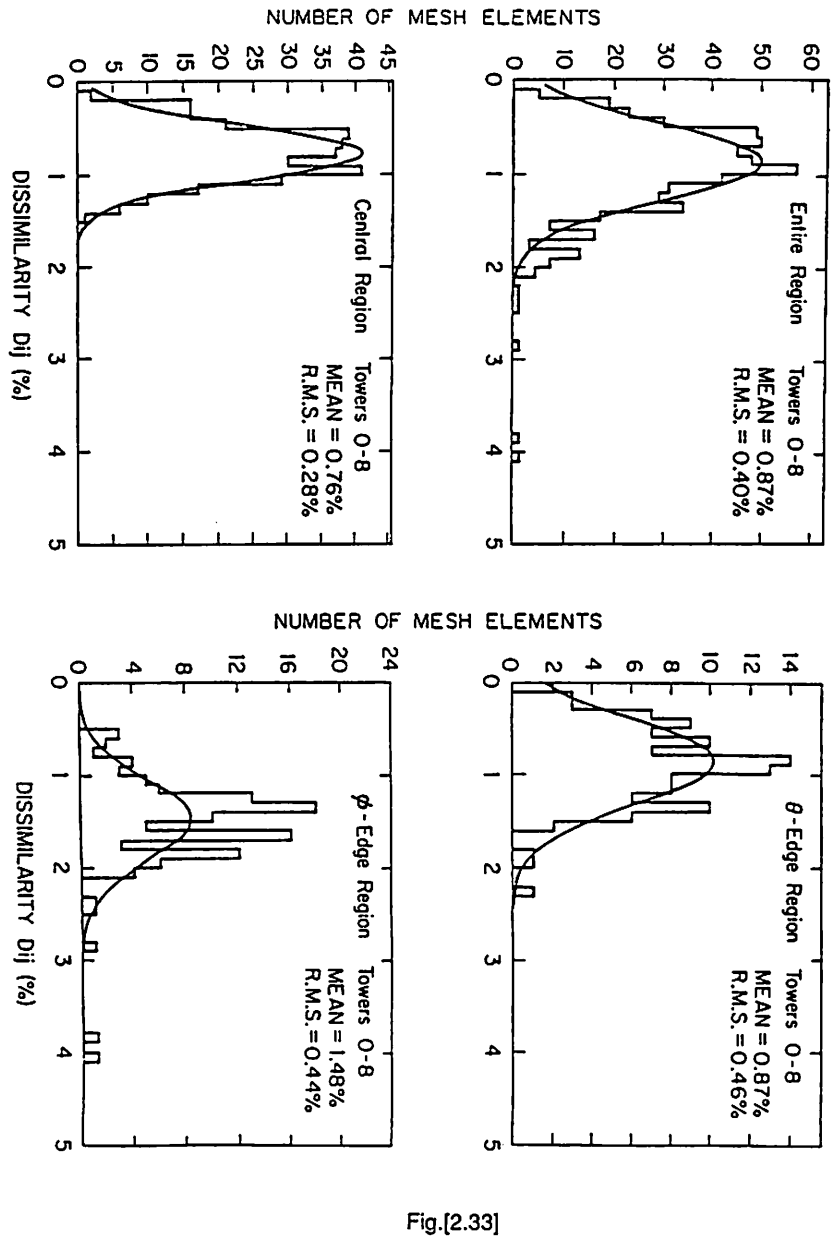

Fig.[2.33]

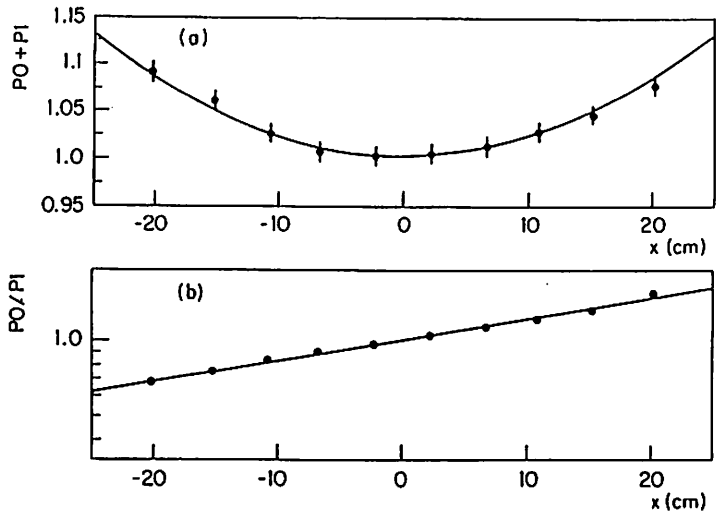

Fig.[2.34]

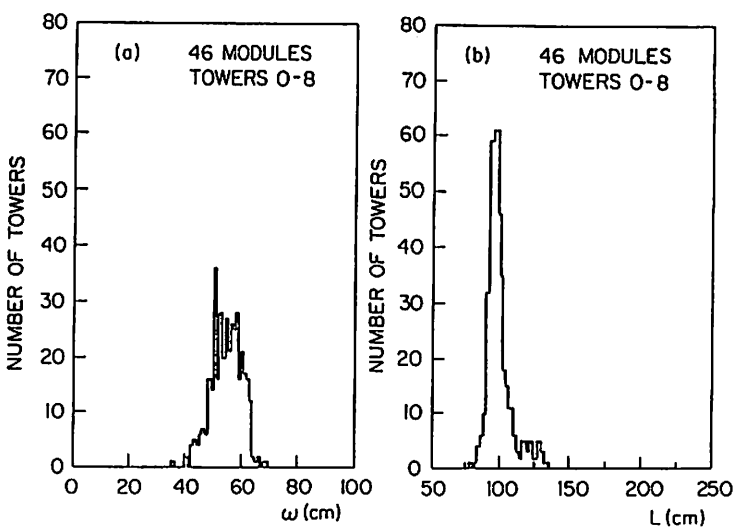

Fig.[2.35]

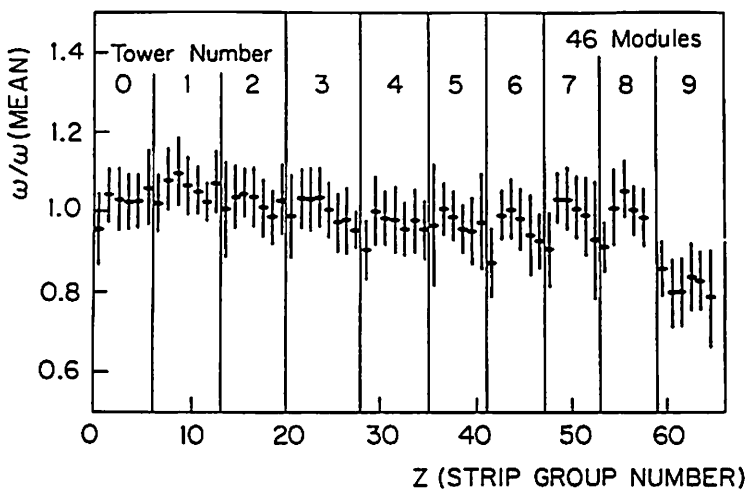

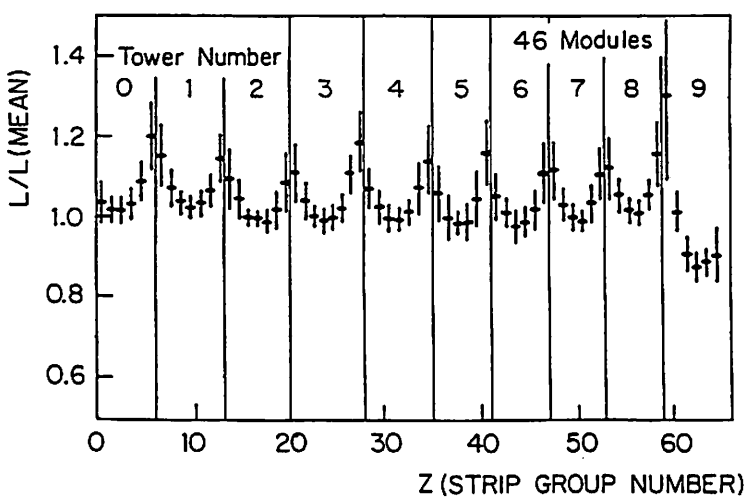

Fig.[2.36]

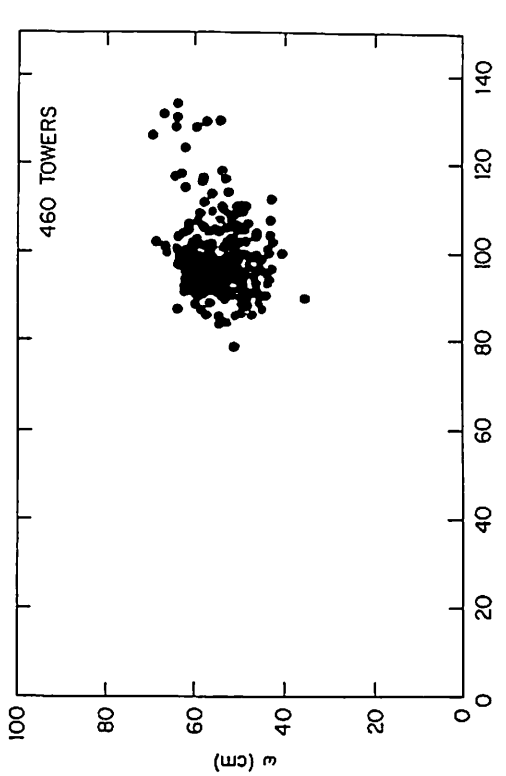

Fig.[2.38]

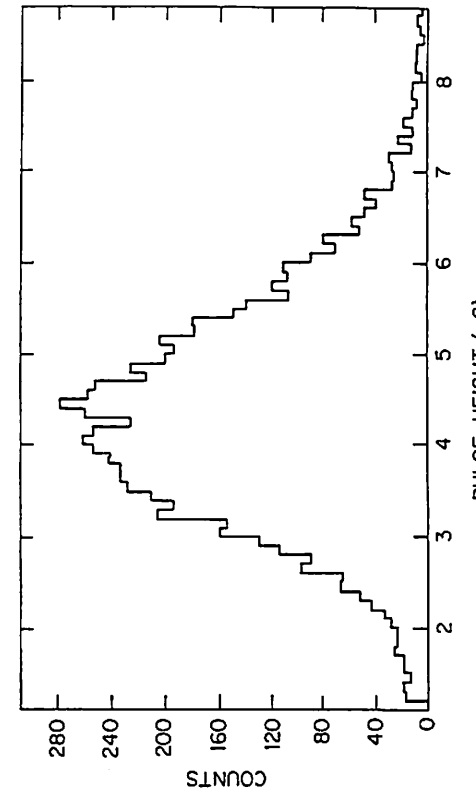

Fig.[2.39]

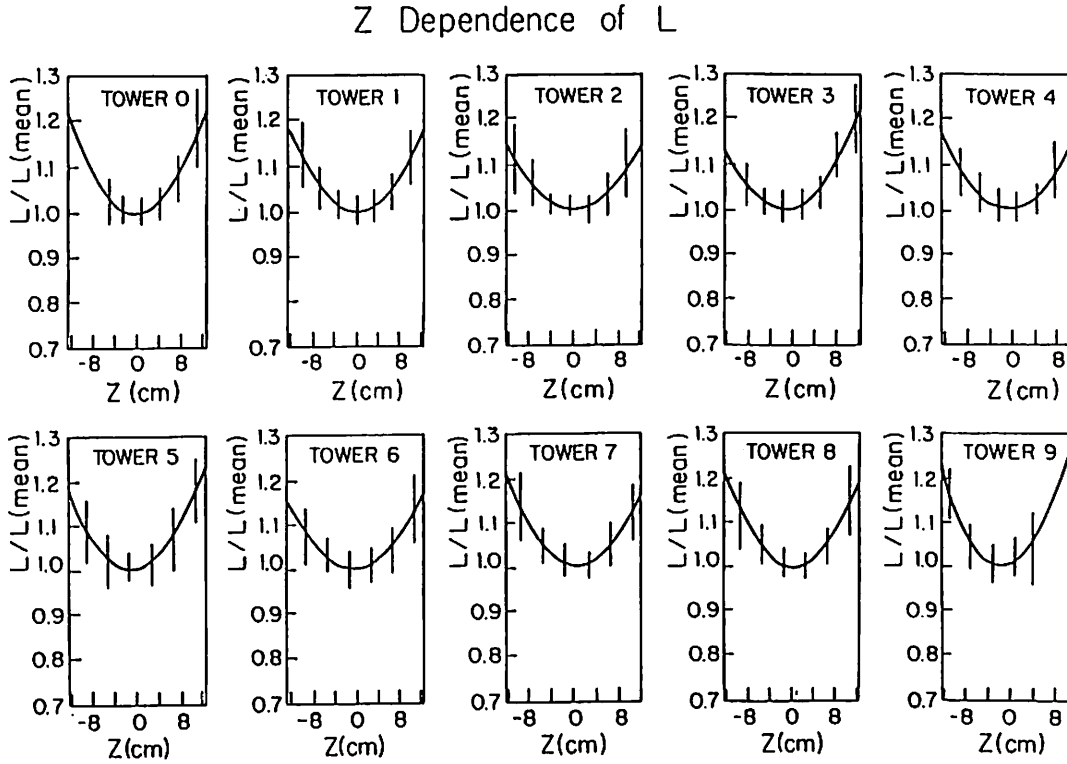

Fig.[2.37]

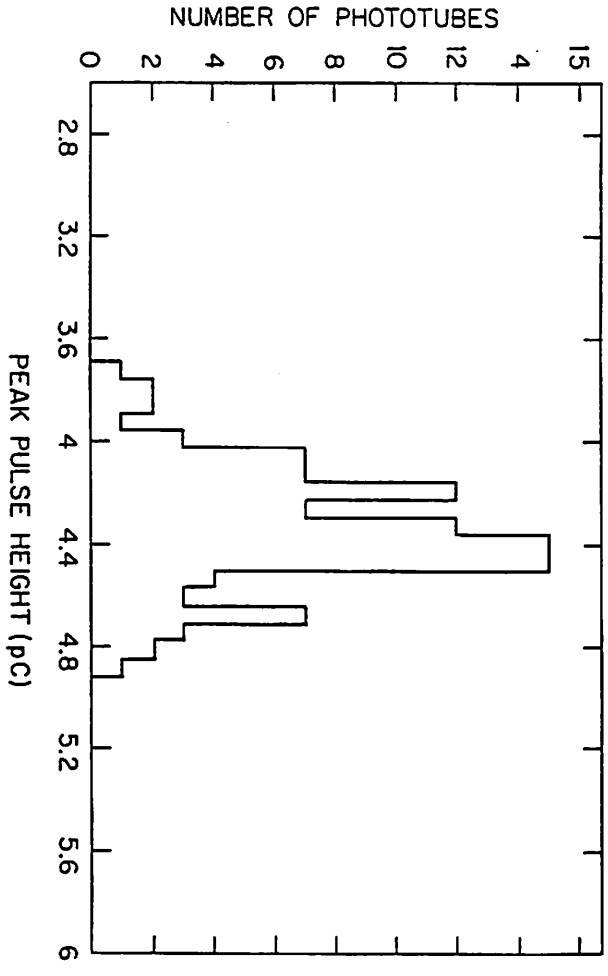

Fig.[2.40]

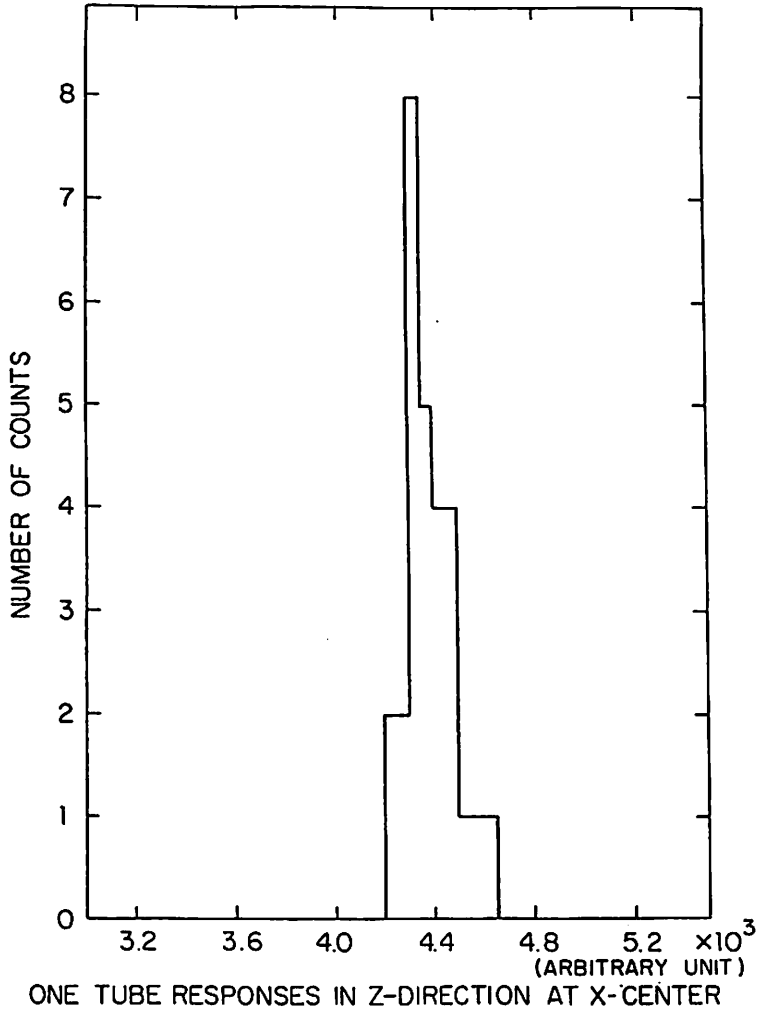

Fig.[2.41]

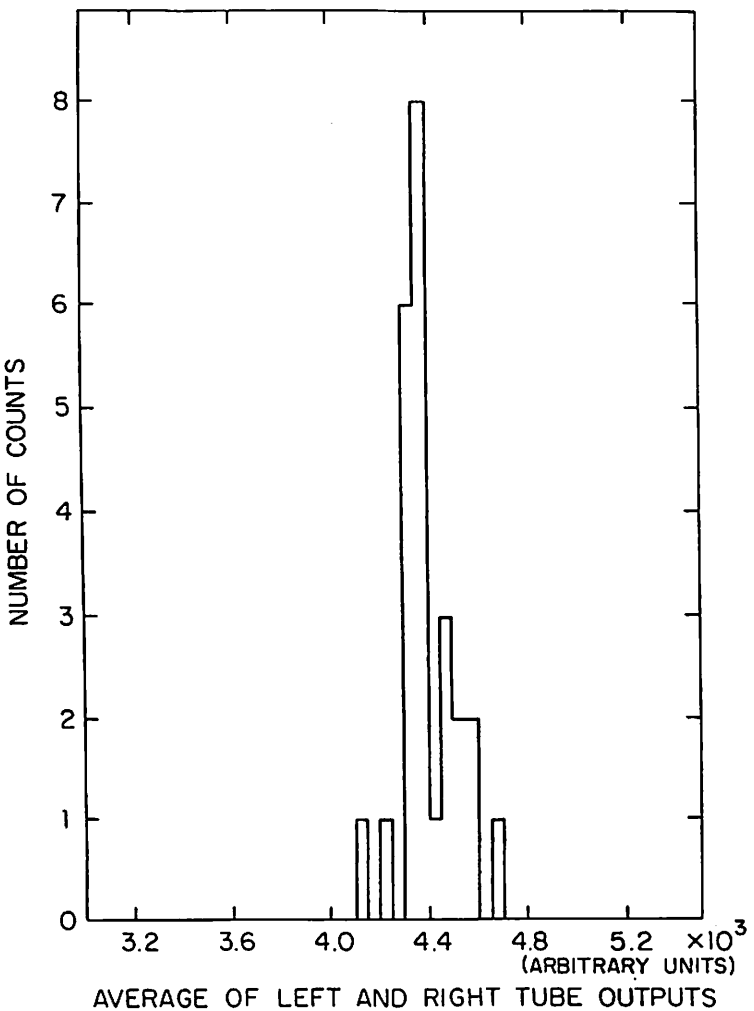

Fig.[2.42]

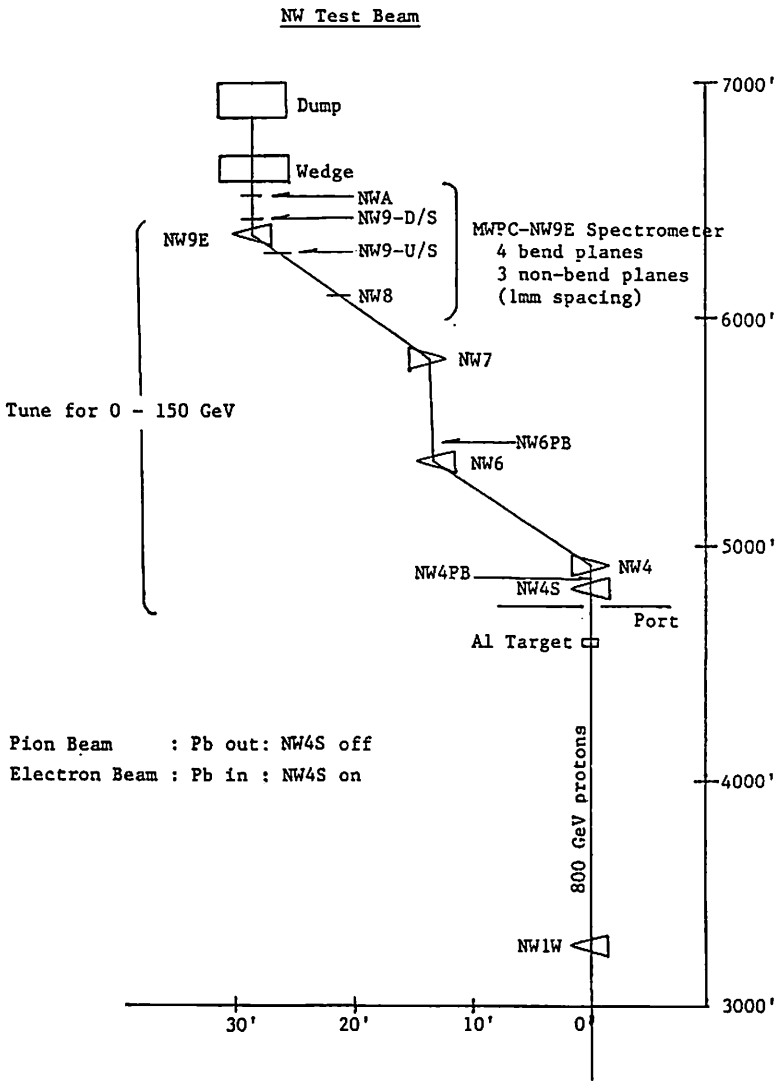

Fig.[2.43]

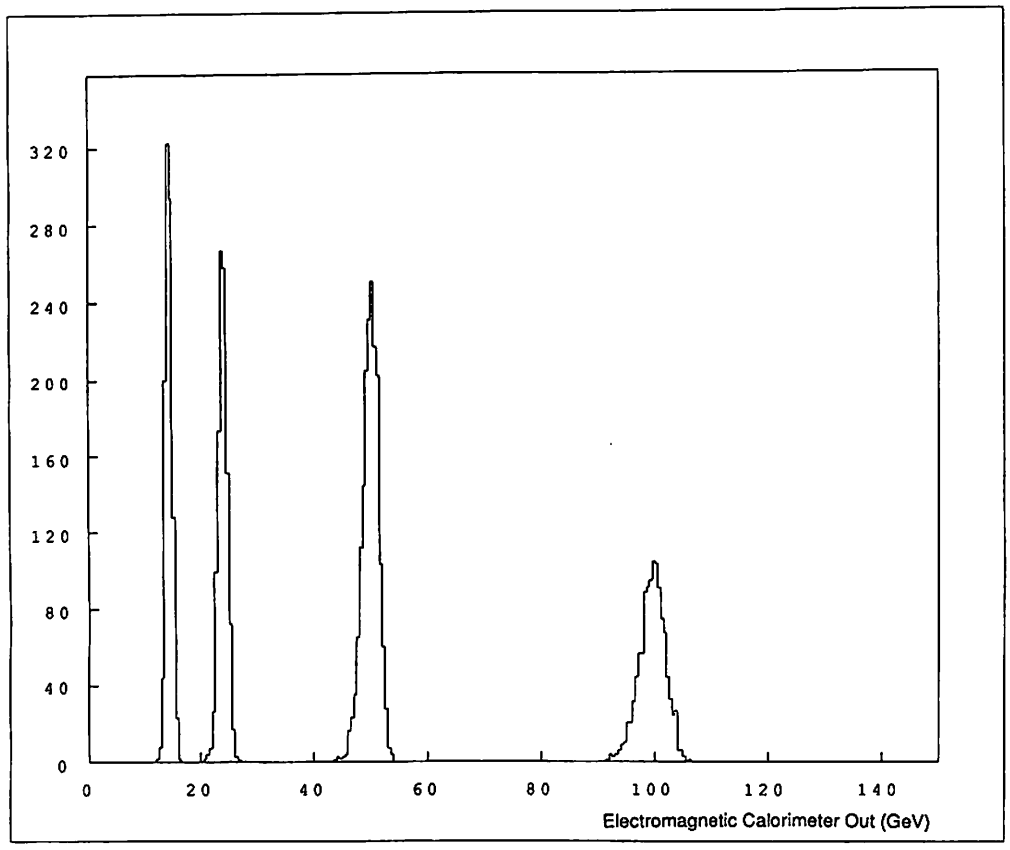

Fig.[2.45]

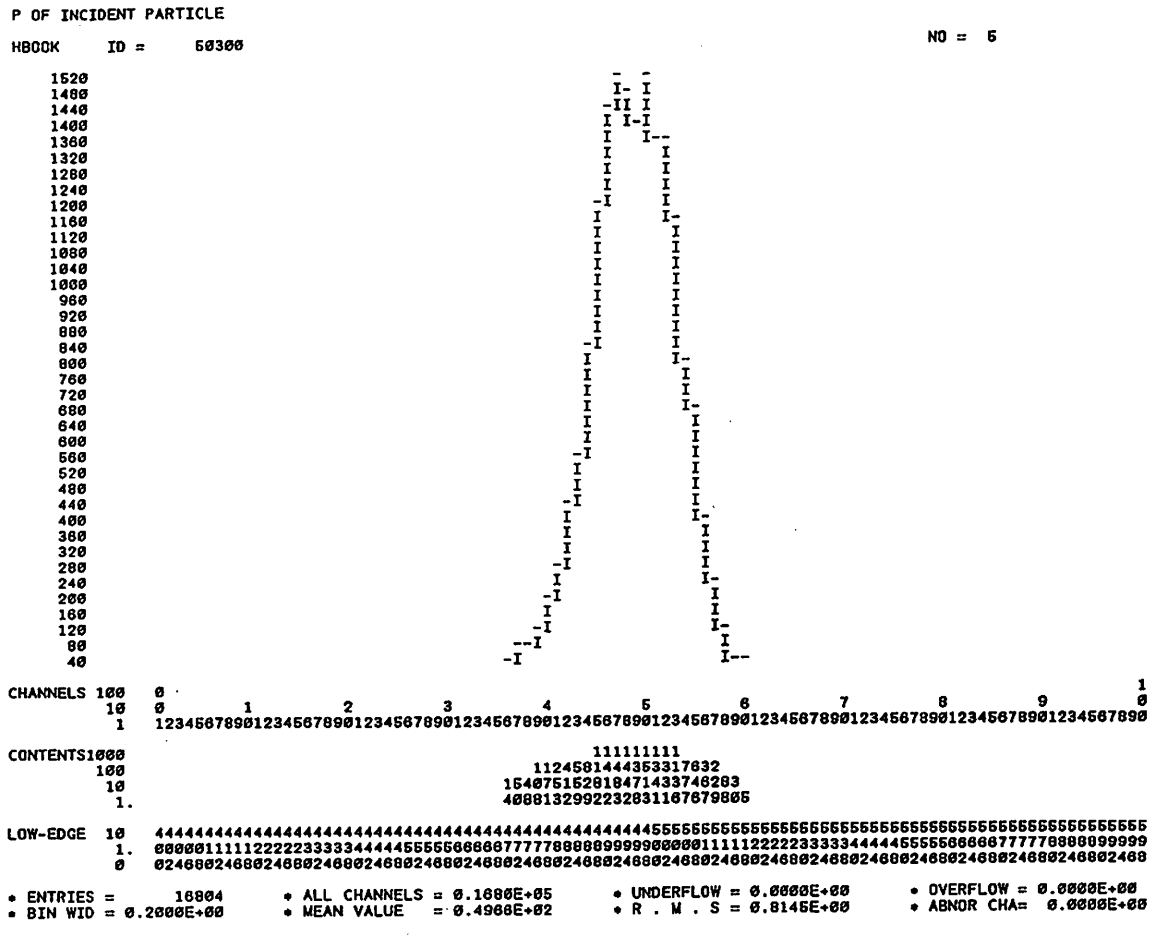

Fig.[2.44]

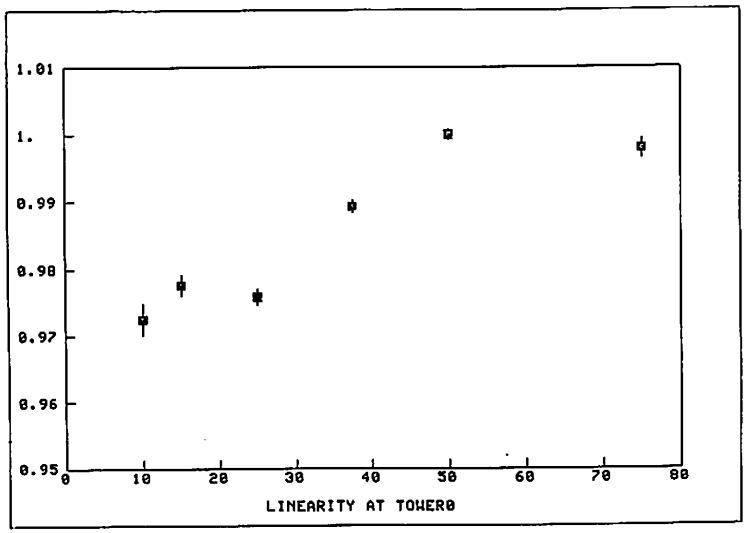

Fig.[2.46a]

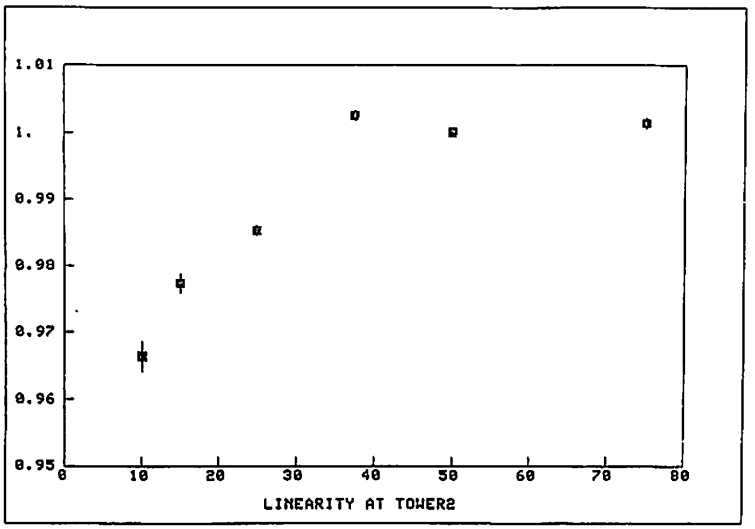

Fig.[2.46c]

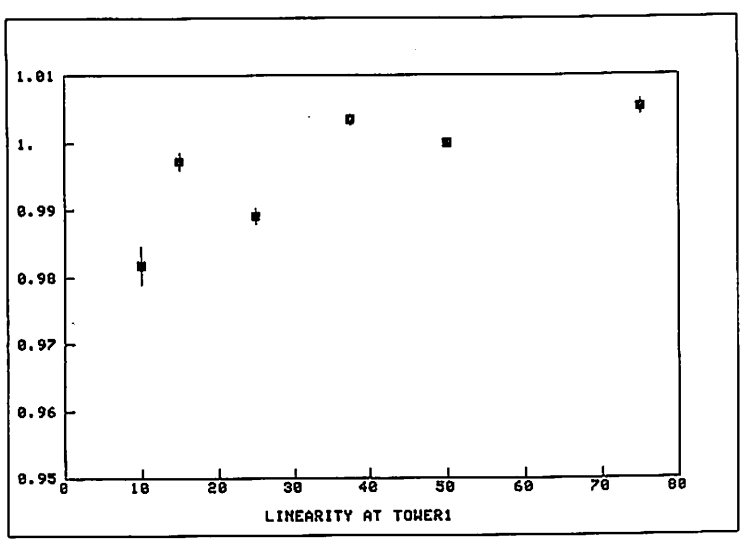

Fig.[2.46b]

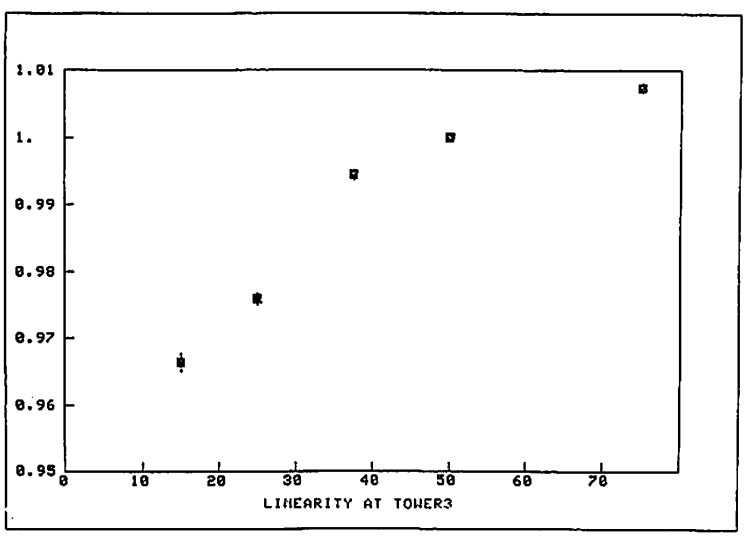

Fig.[2.46d]

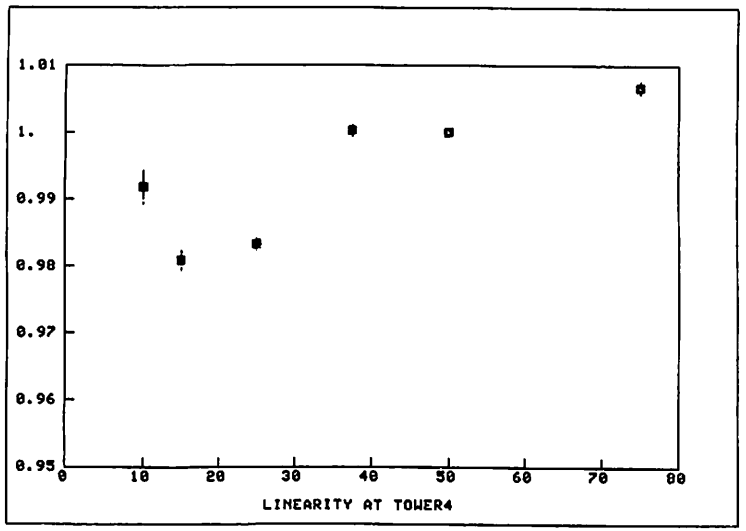

Fig.[2.46e]

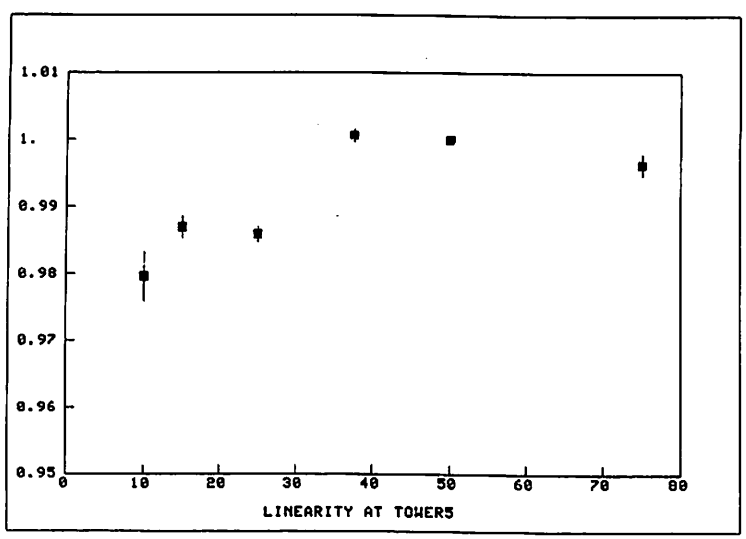

Fig.[2.46 f]

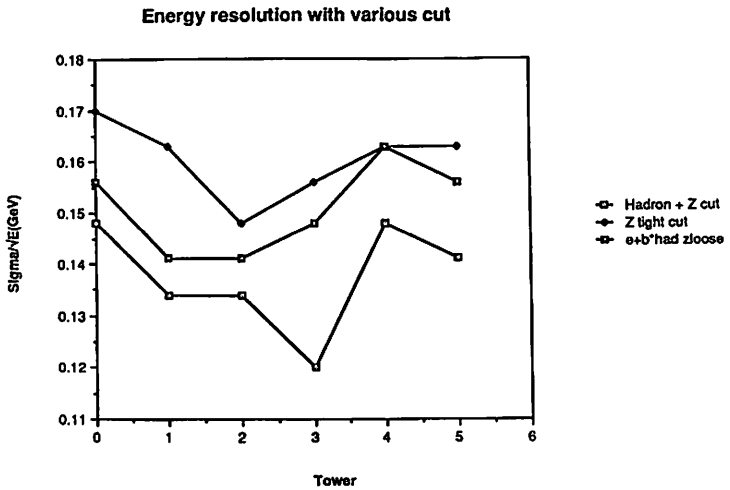

Fig.[2.47]

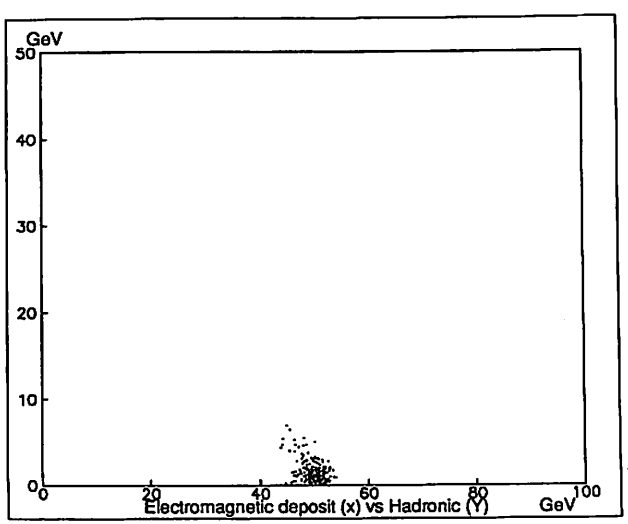

Fig.[2.48]

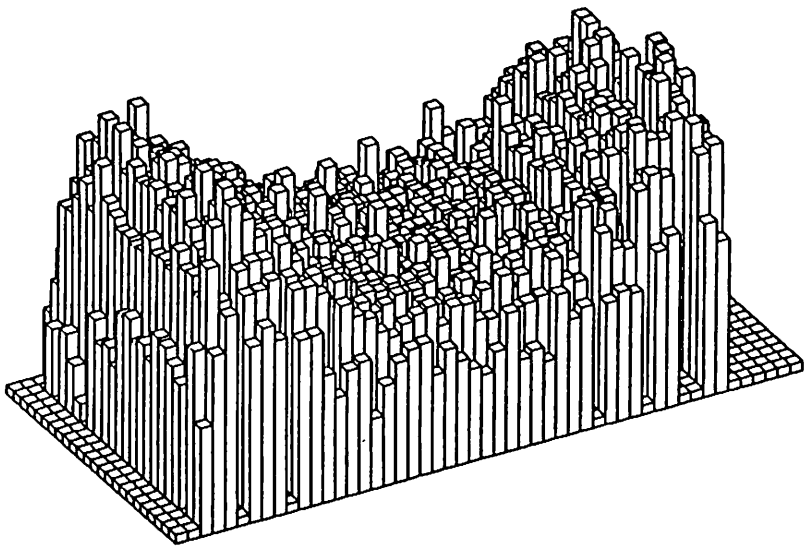

Fig.[2.49]

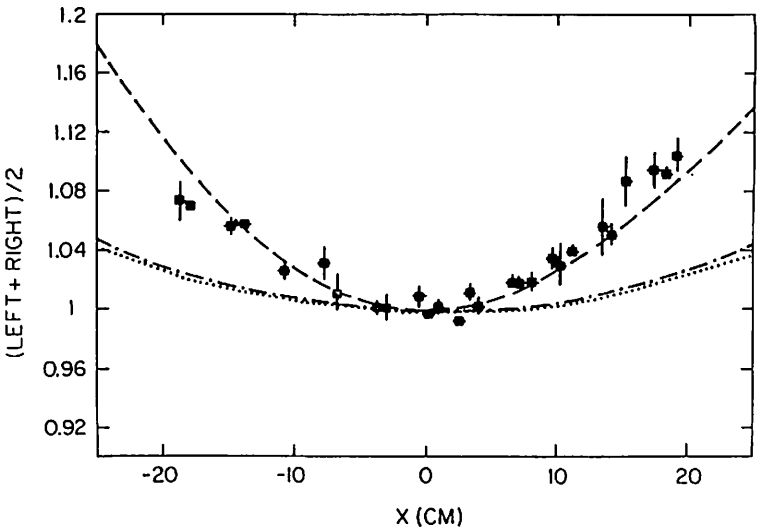

Fig.[2.50]

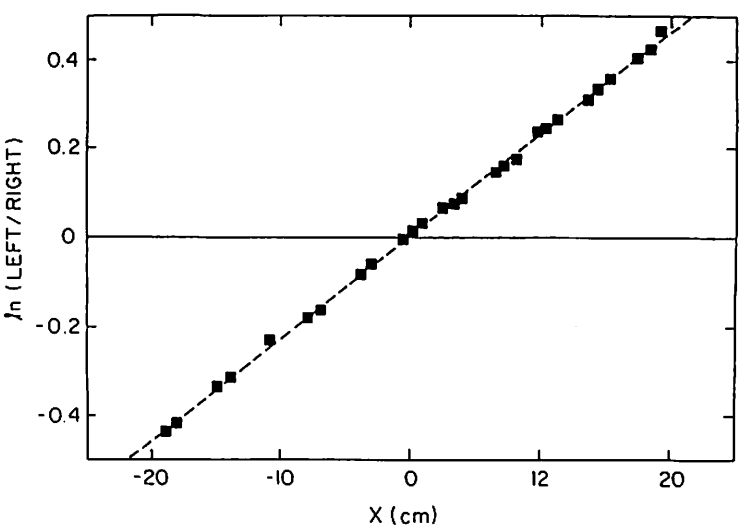

Fig.[2.51]

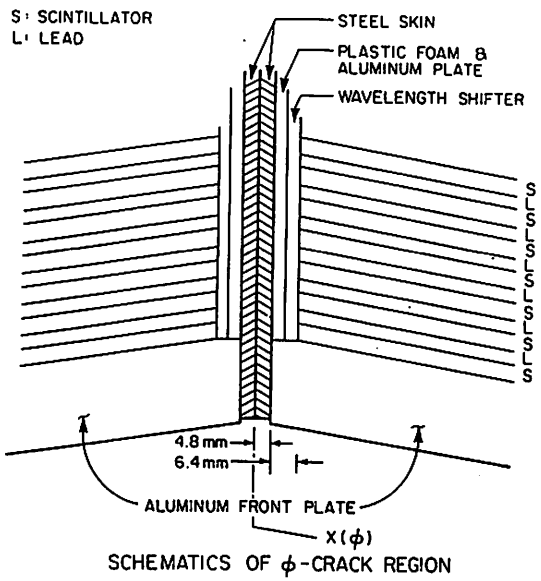

Fig.[2.52]

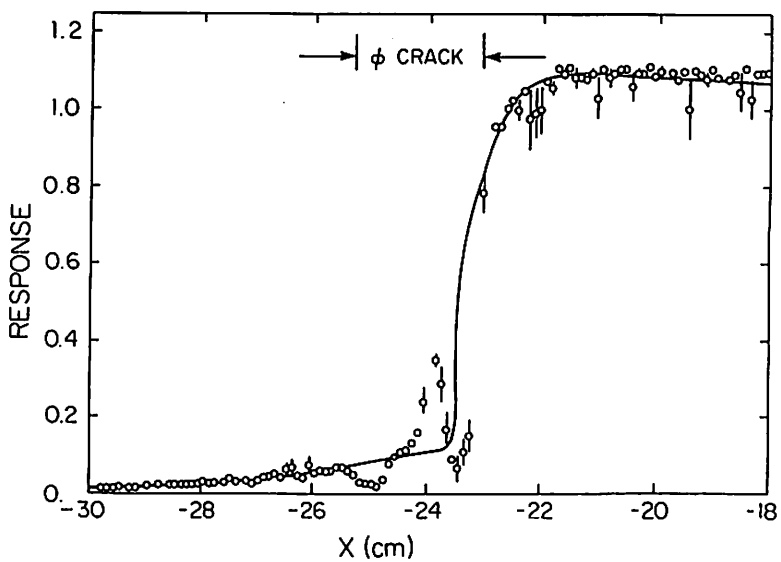

Fig.[2.53]

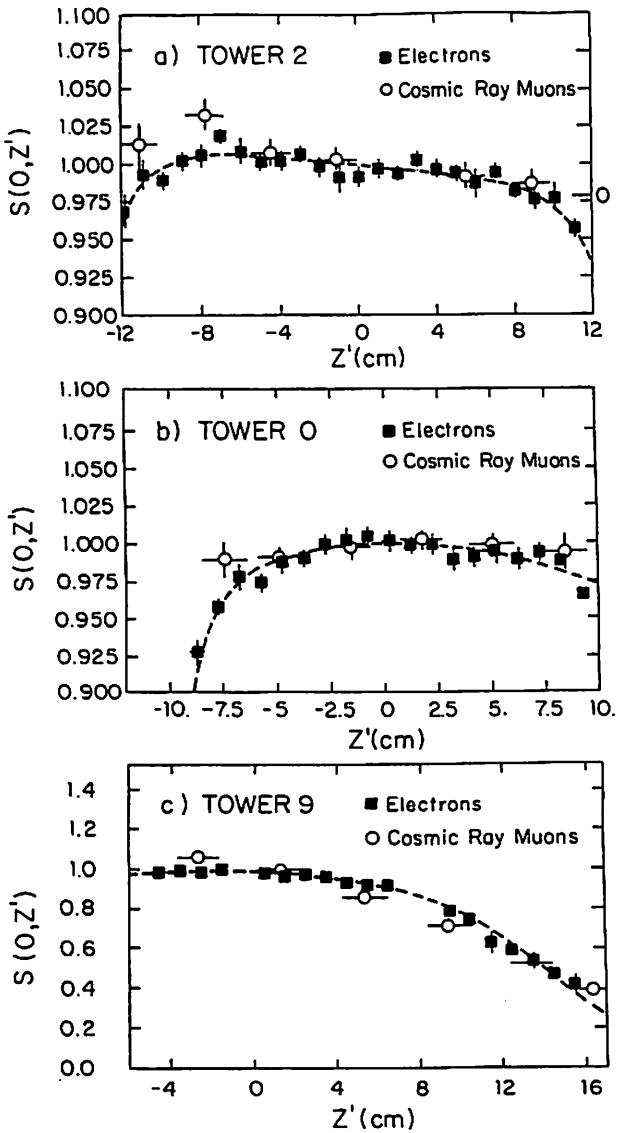

Fig.[2.54]

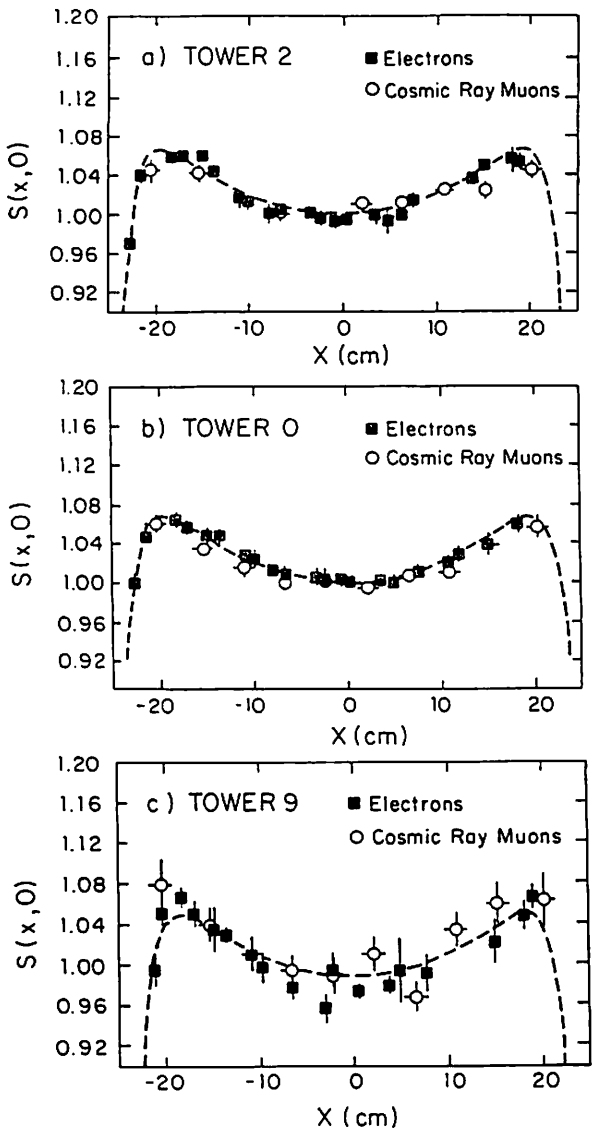

Fig.[2.55]

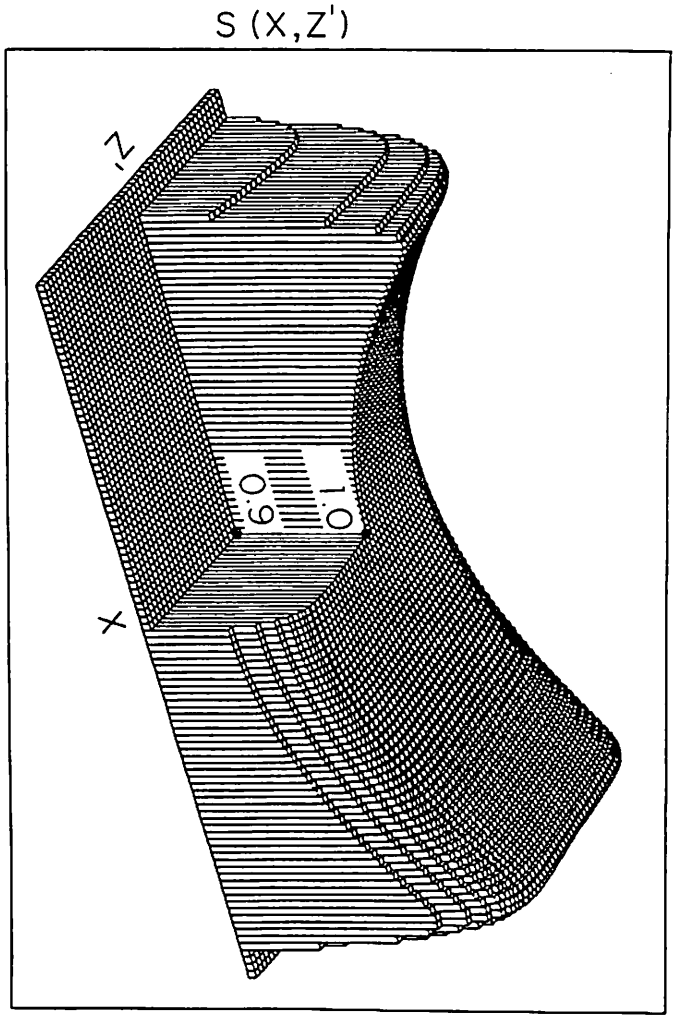

Fig.[2.56]

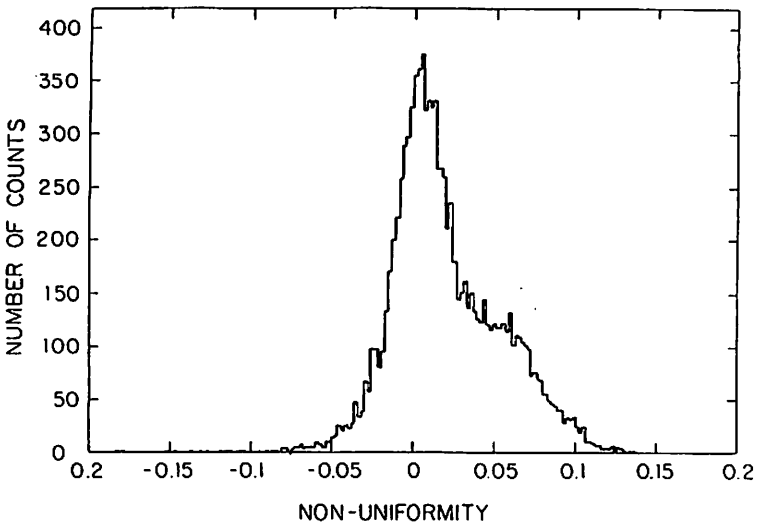

Fig.[2.57]

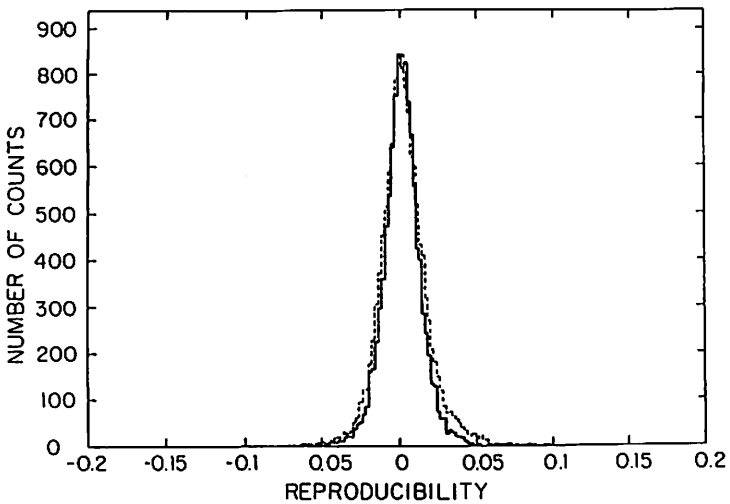

Fig.[2.59]

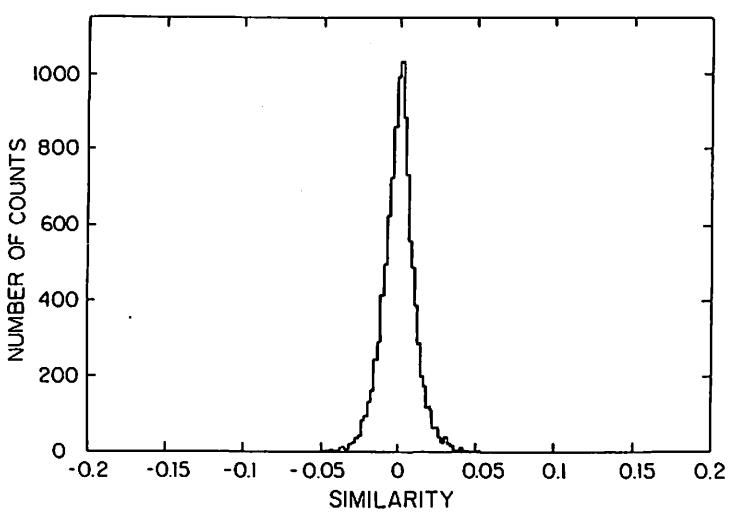

Fig.[2.58]

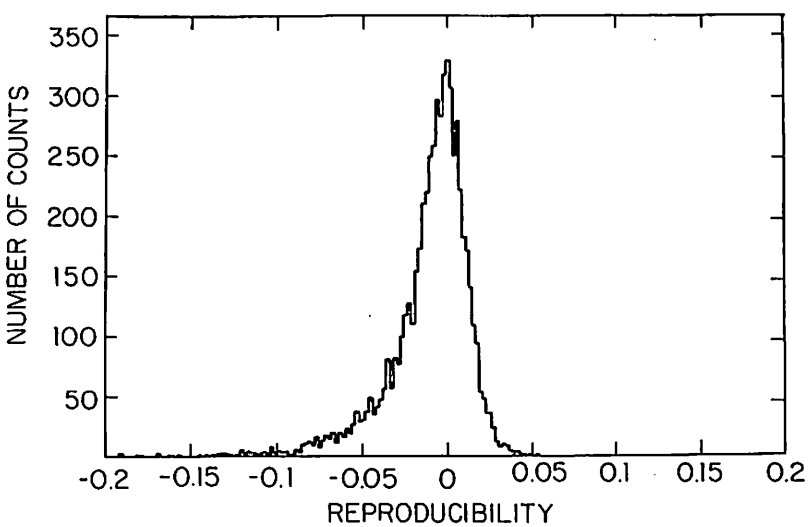

Fig.[2.60]

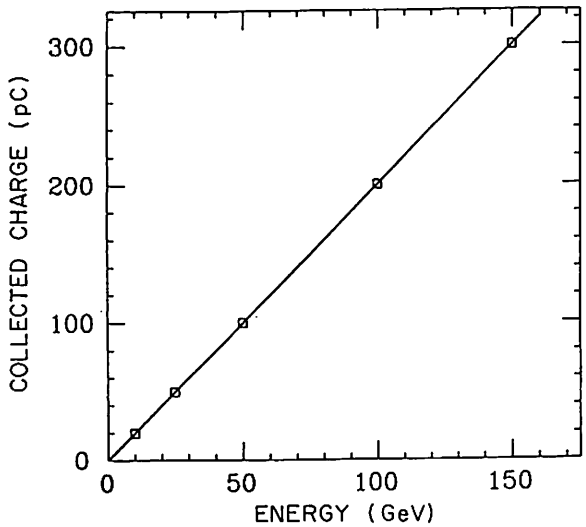

Fig.[2.61]

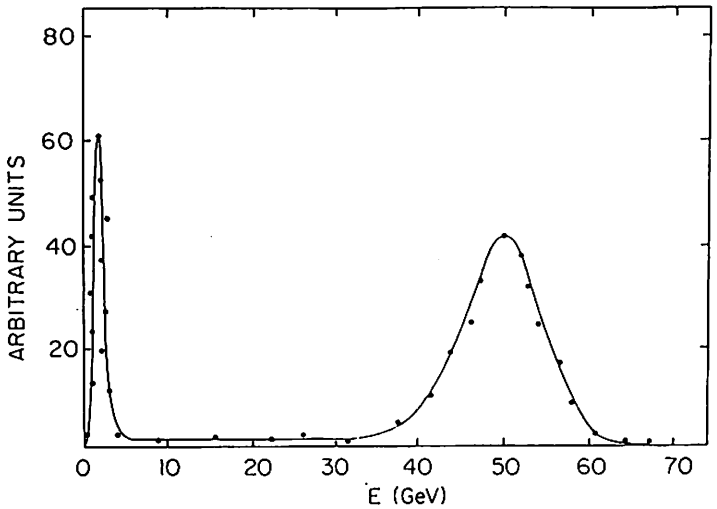

Fig.[2.63]

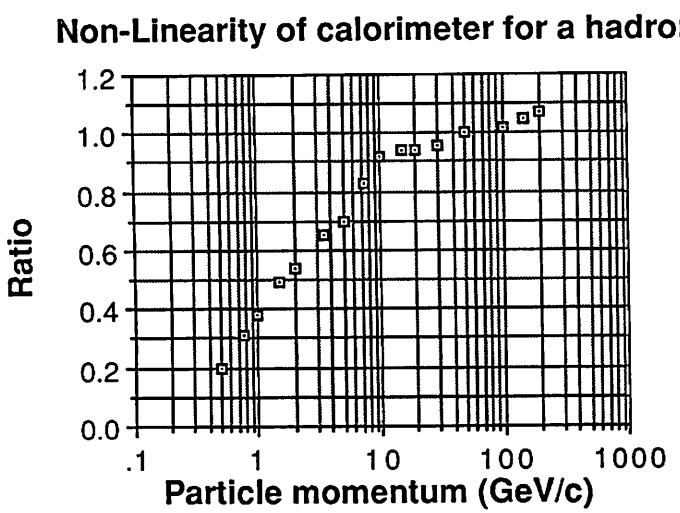

Fig.[2.62]

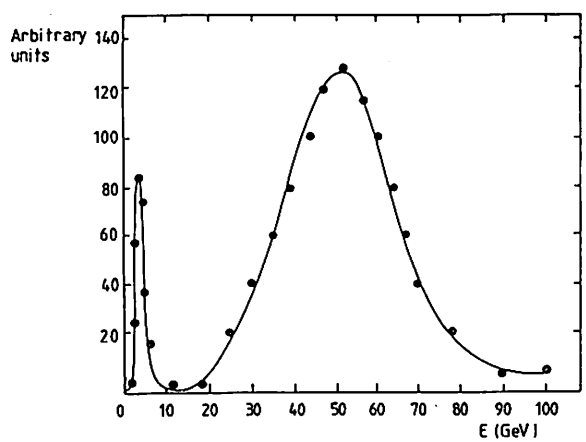

Fig.[2.64]

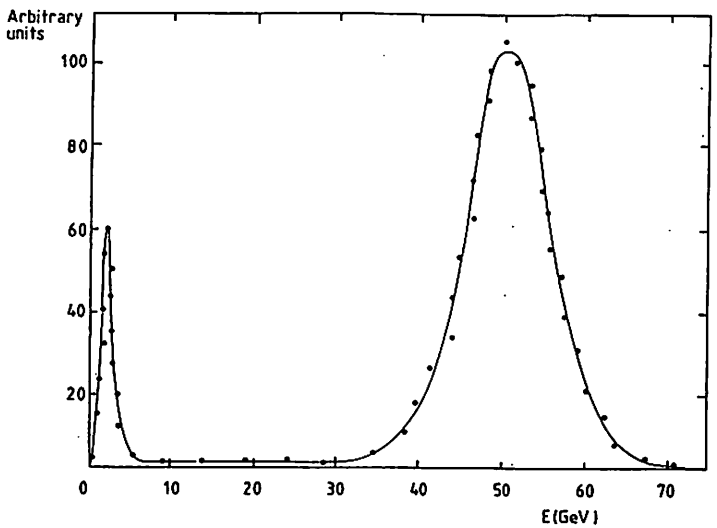

Fig.[2.65]

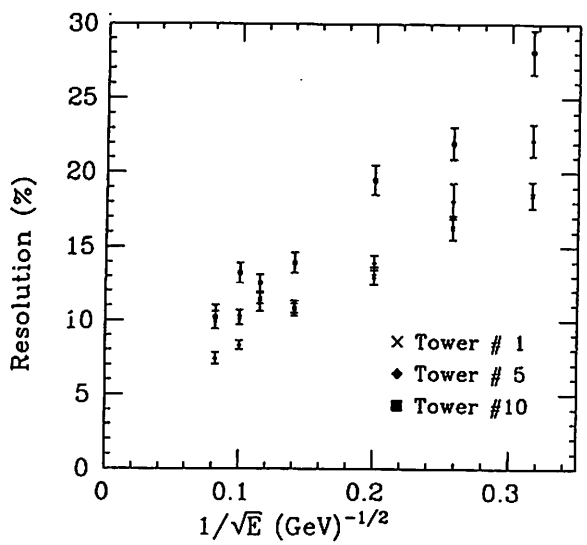

Fig.[2.66]

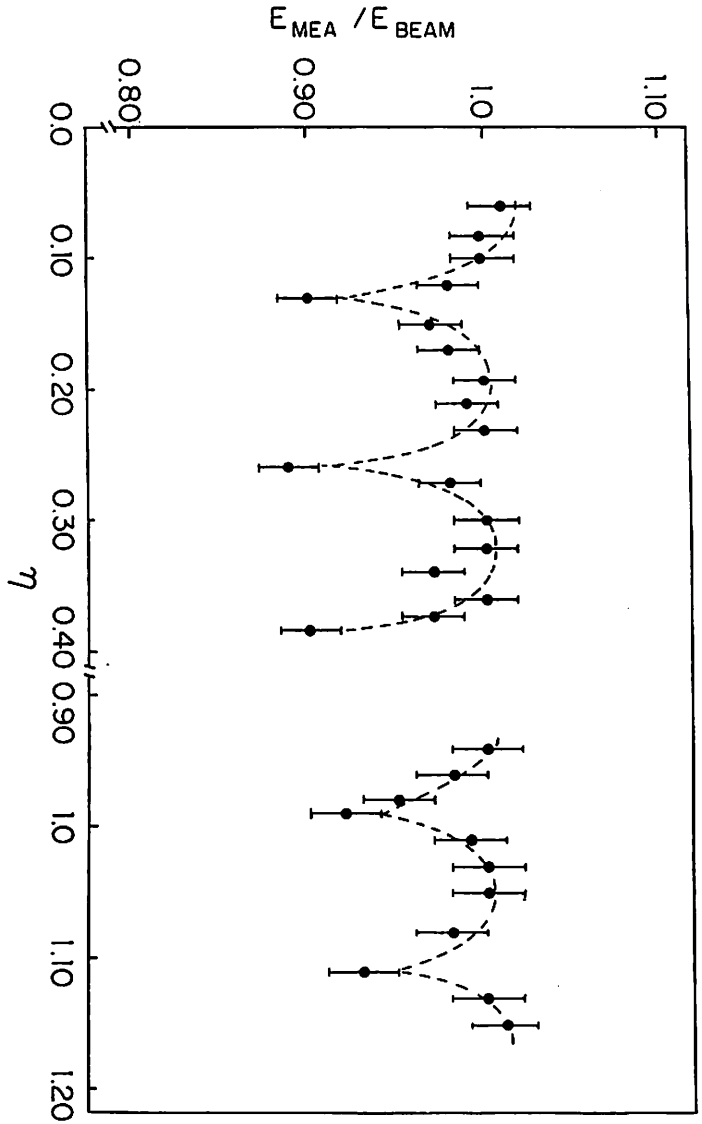

Fig.[2.67]

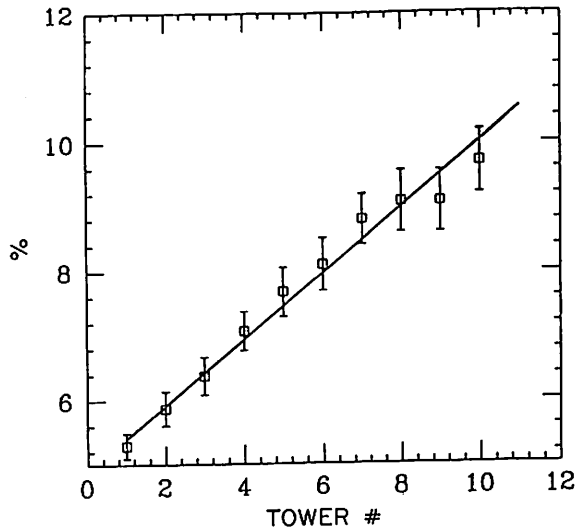

Fig.[2.68]

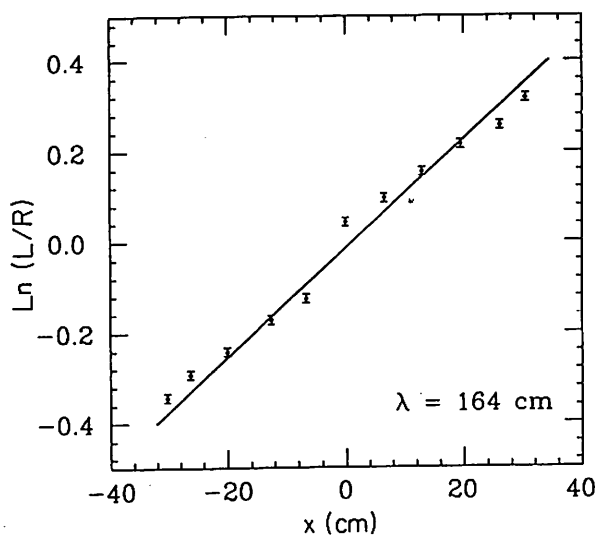

Fig.[2.69]

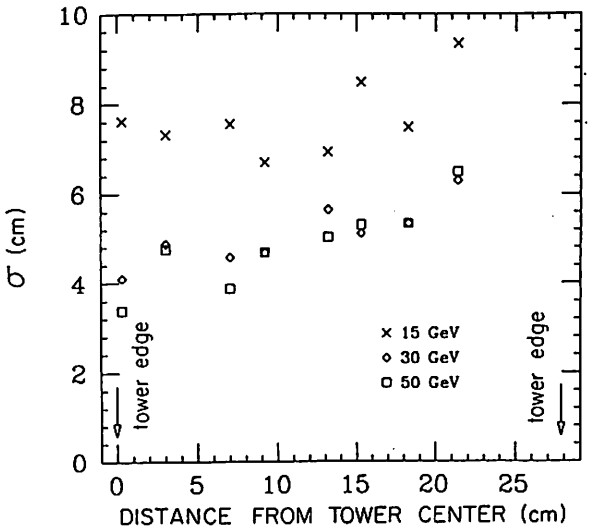

Fig.[2.70]

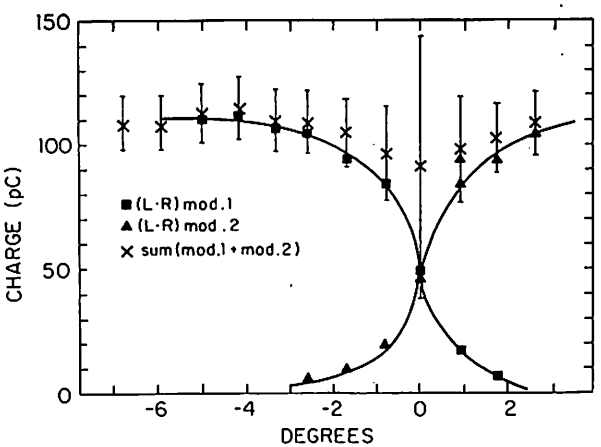

Fig.[2.71]

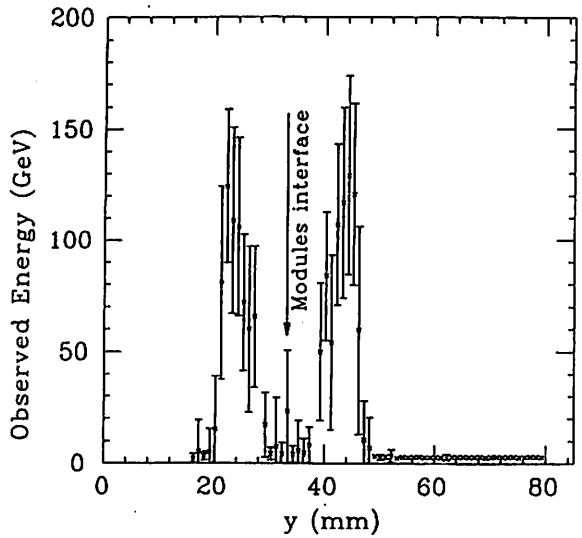

Fig.[2.72]

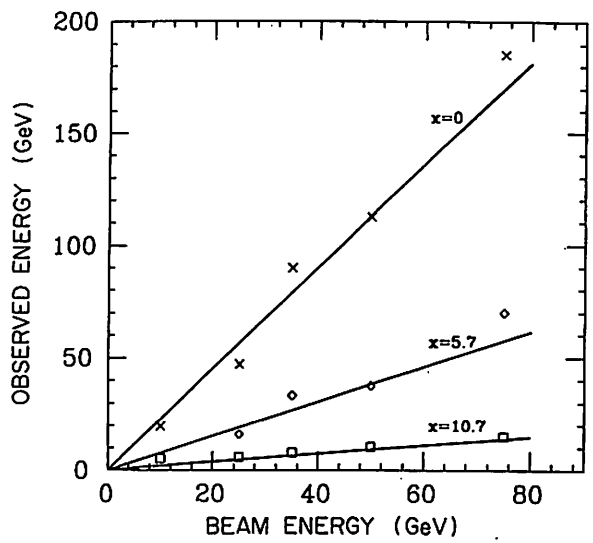

Fig.[2.73]

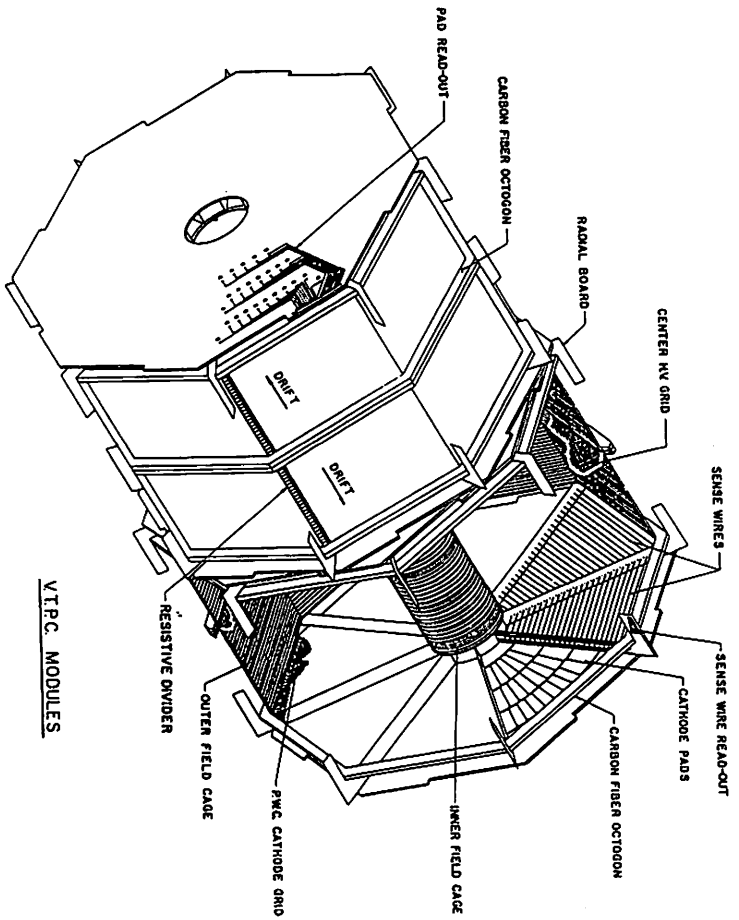

Fig.[2.74]

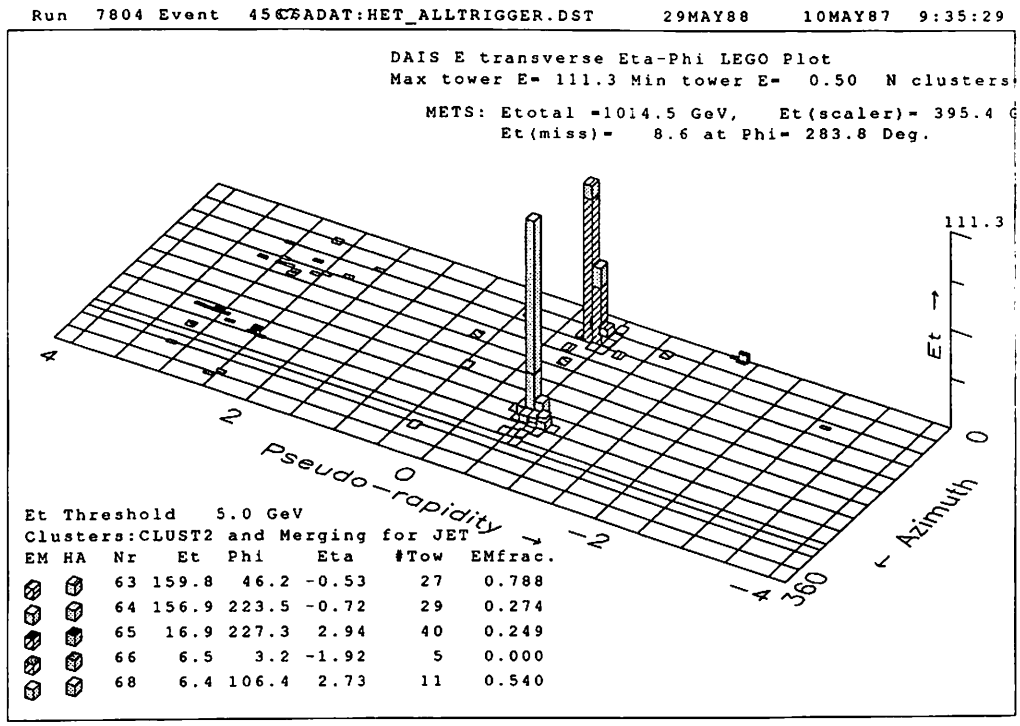

Fig.[3. 1]

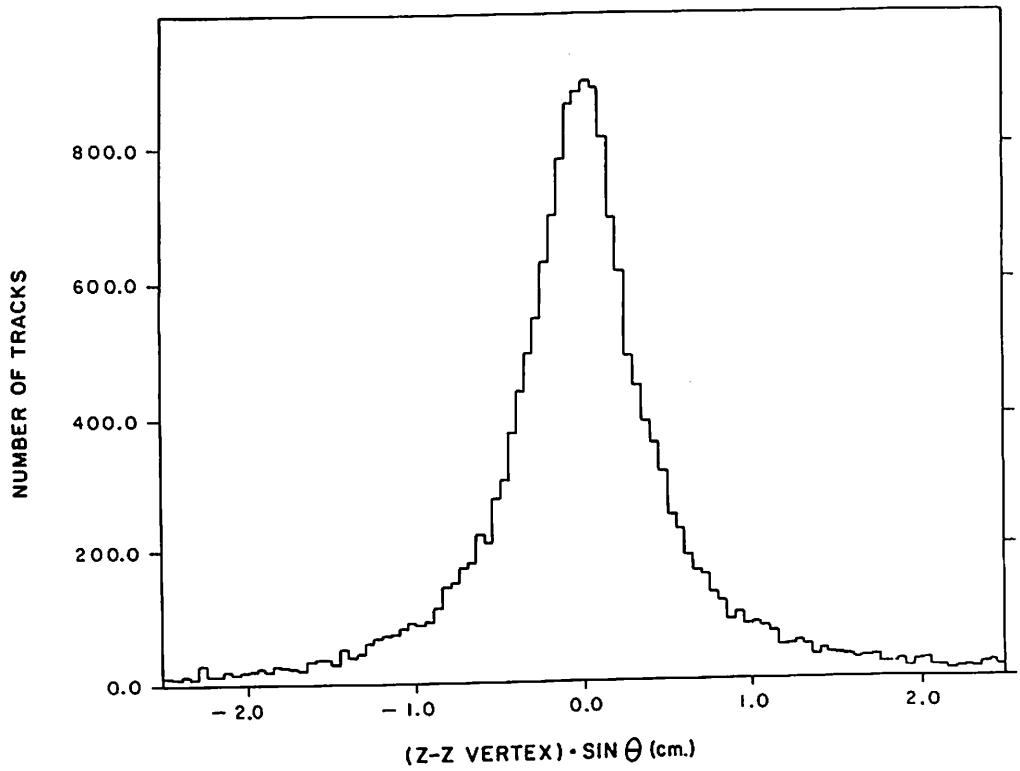

Fig.[2.75]

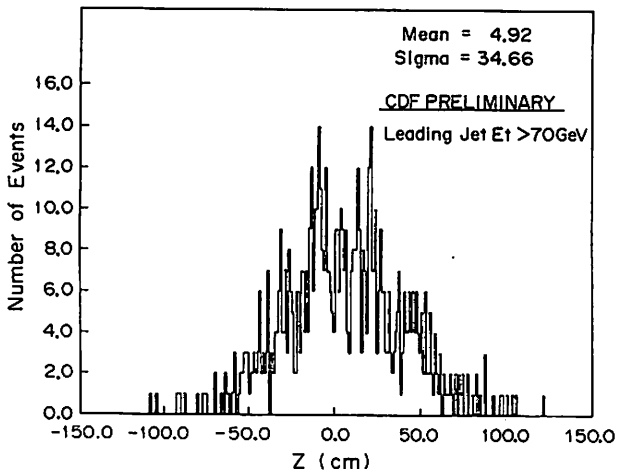

Fig.[3. 2]

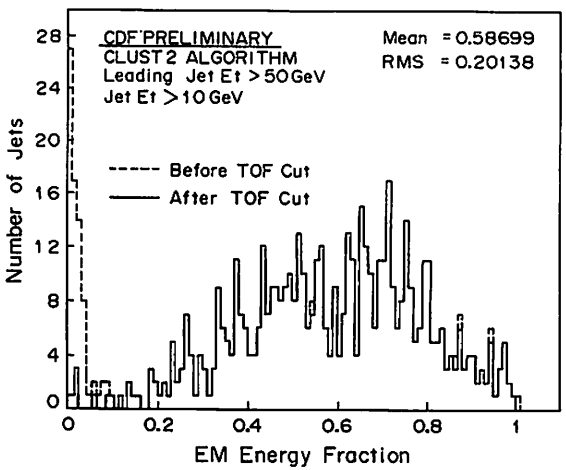

Fig.[3. 3]

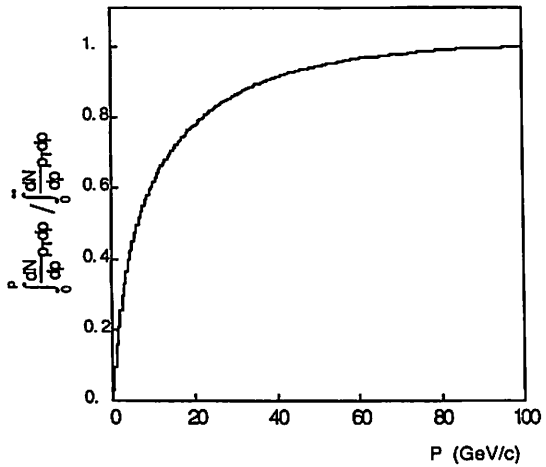

Fig.[3. 4]

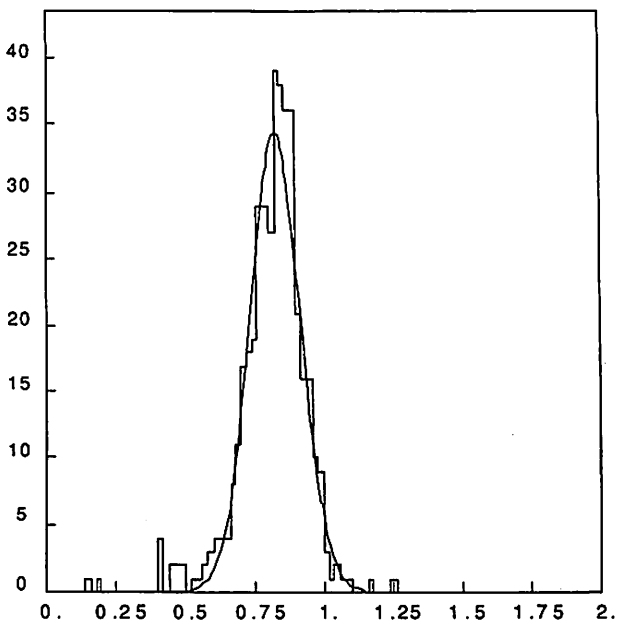

Pt(Cluster)/Pt(Parton)

Fig. [3.5]

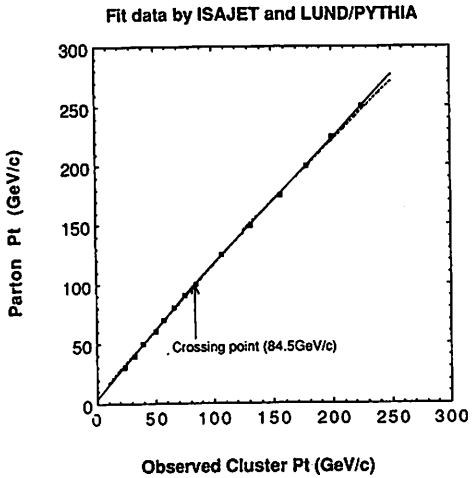

Fig. [3.6]

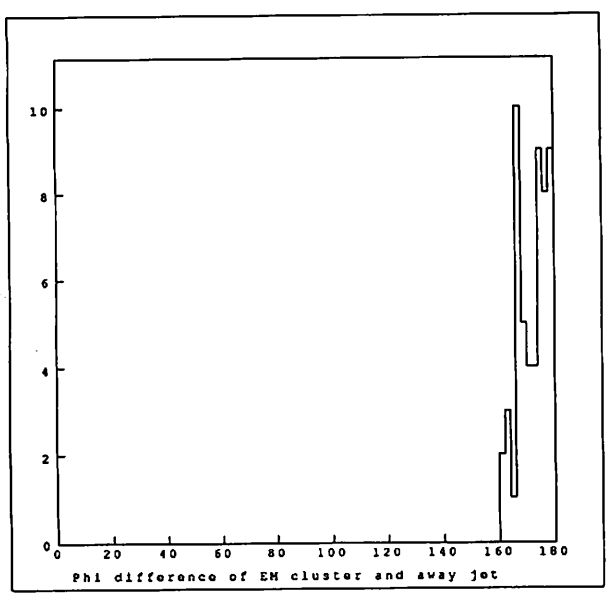

Fig. [3.7]

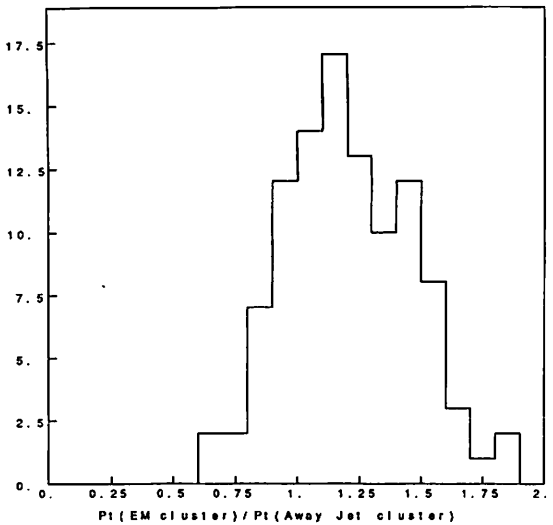

Fig. [3.8]

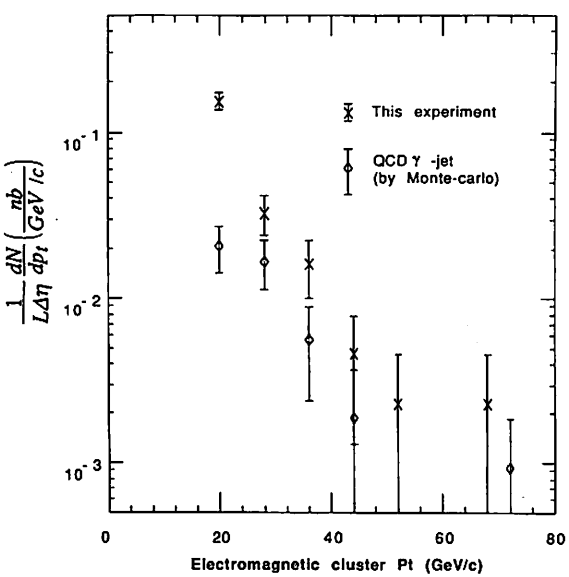

Fig. [3.9]

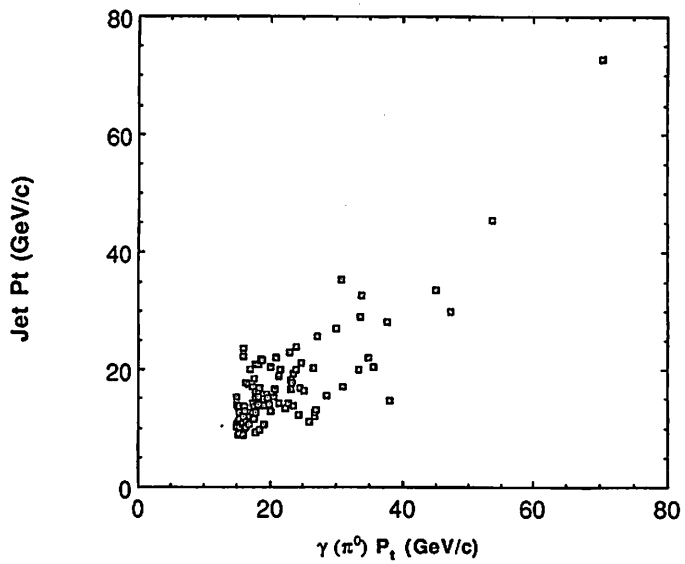

Fig. [3.10a]

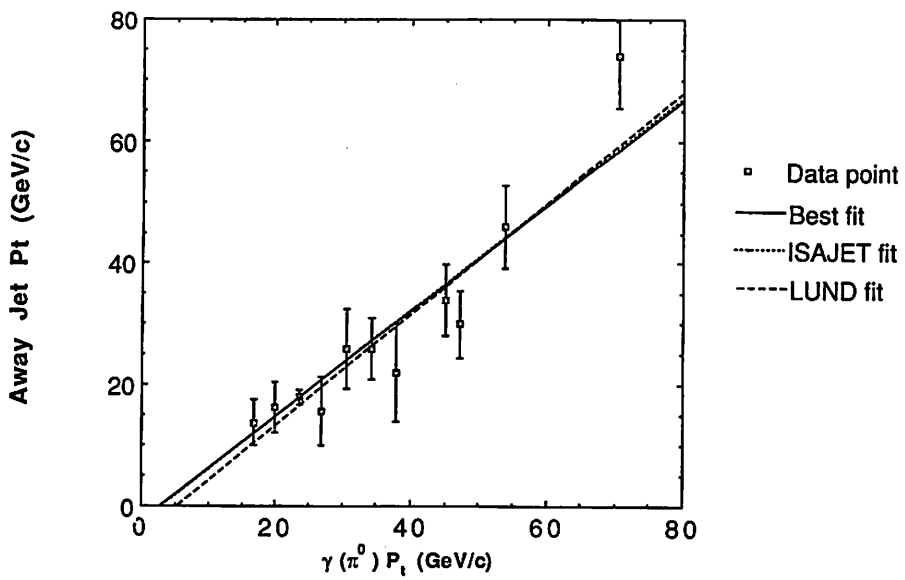

Fig. [3.10b]

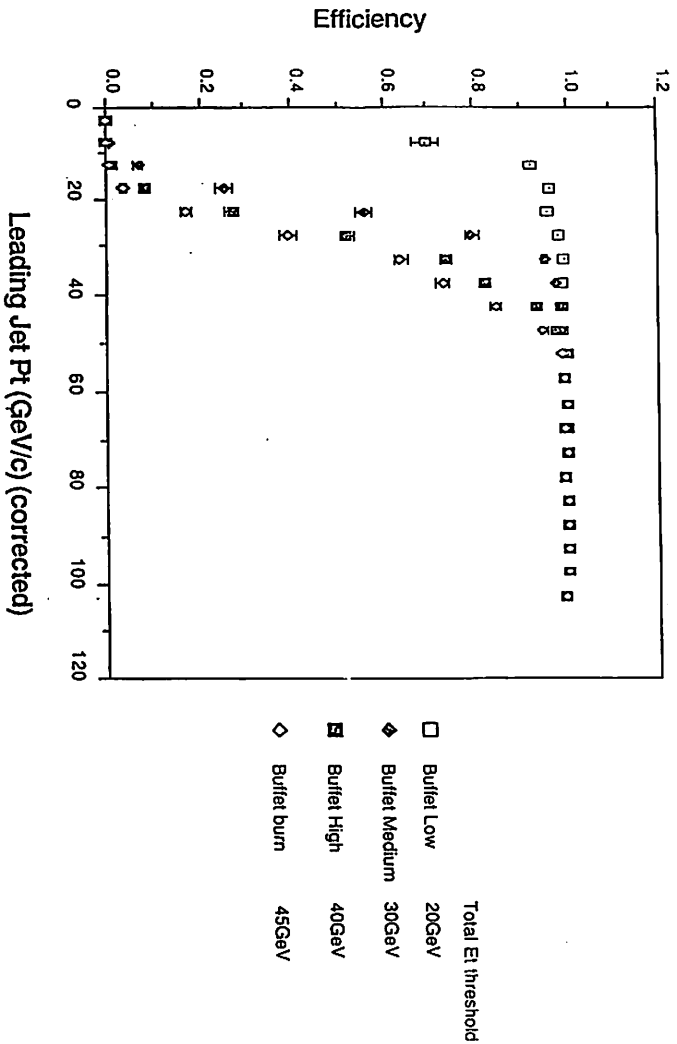

Fig. [3.11]

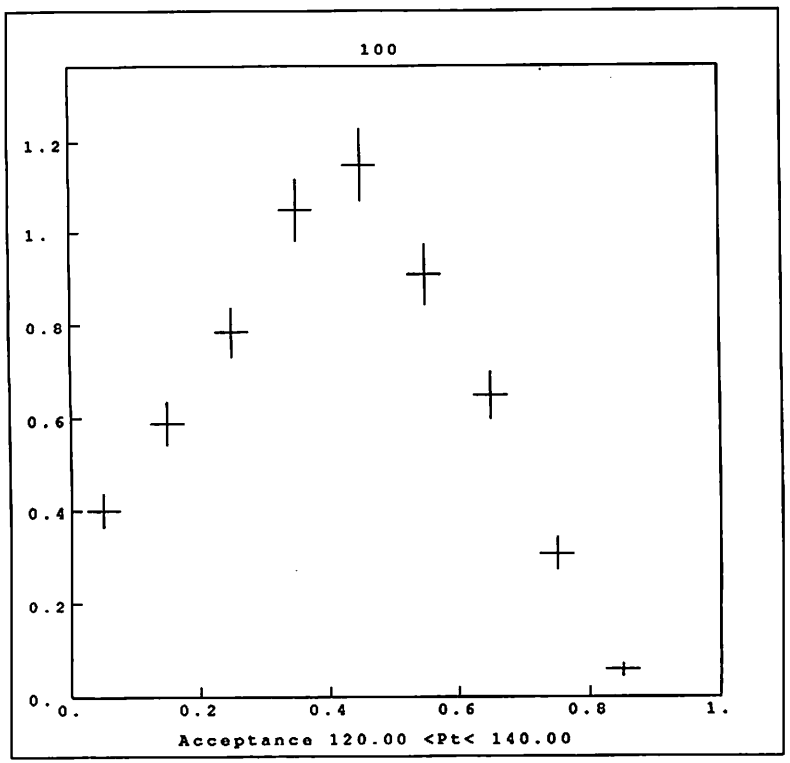

Fig. [3.12]

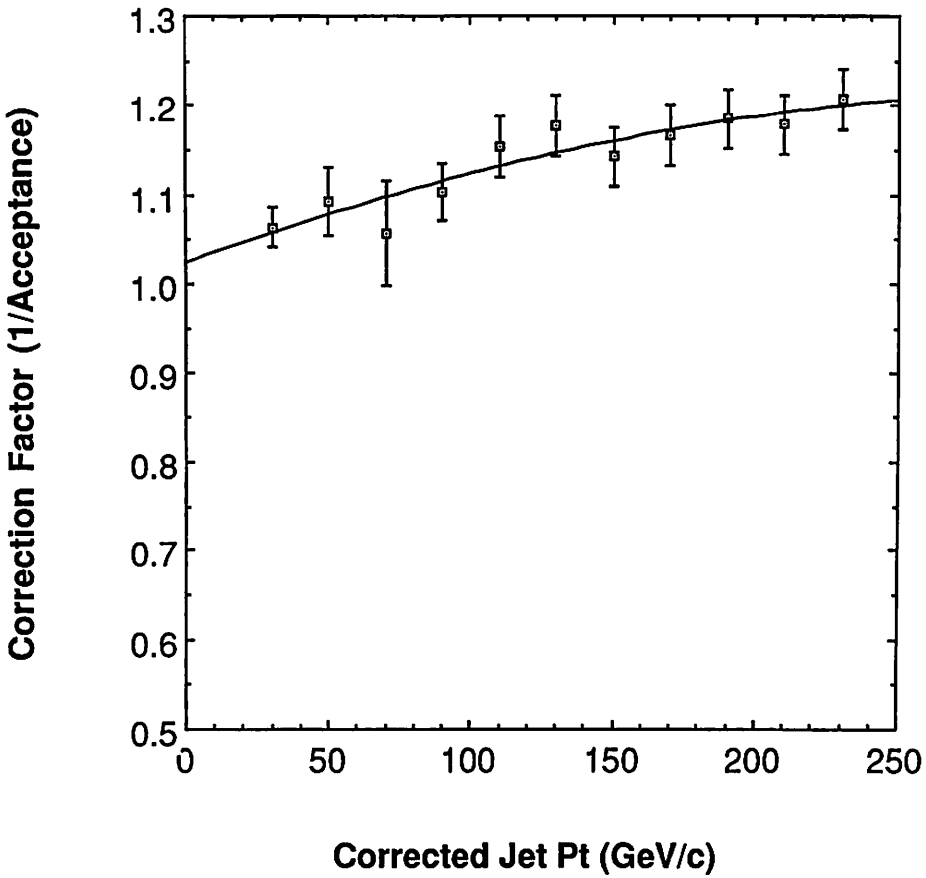

Fig. [3.13]

Observed jet cross section under various trigger conditions.

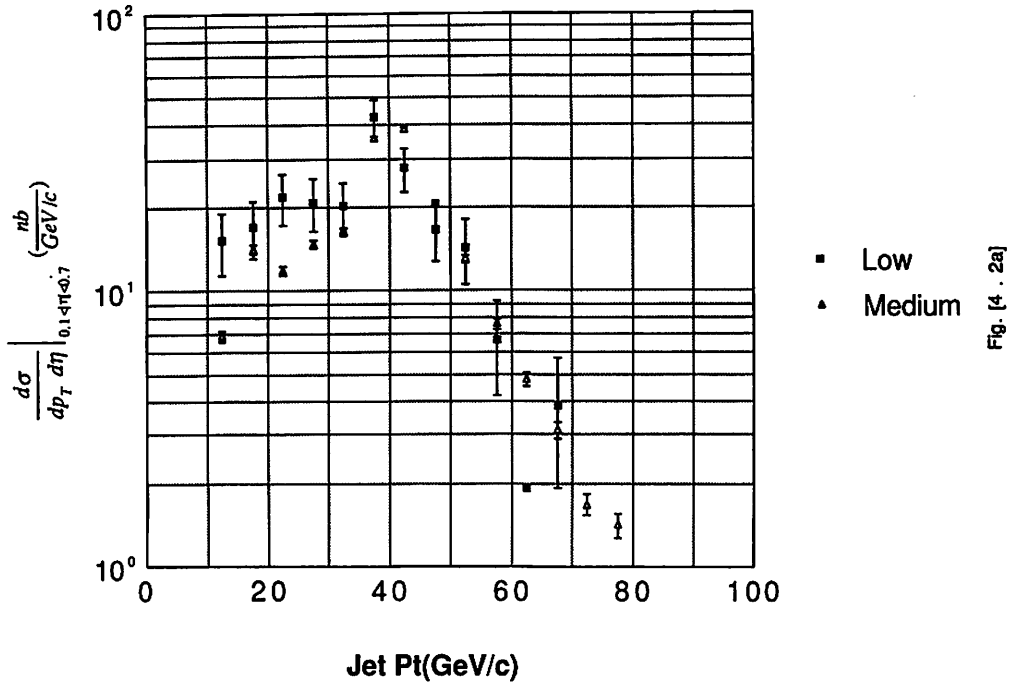

Fig. [4 . 2a]

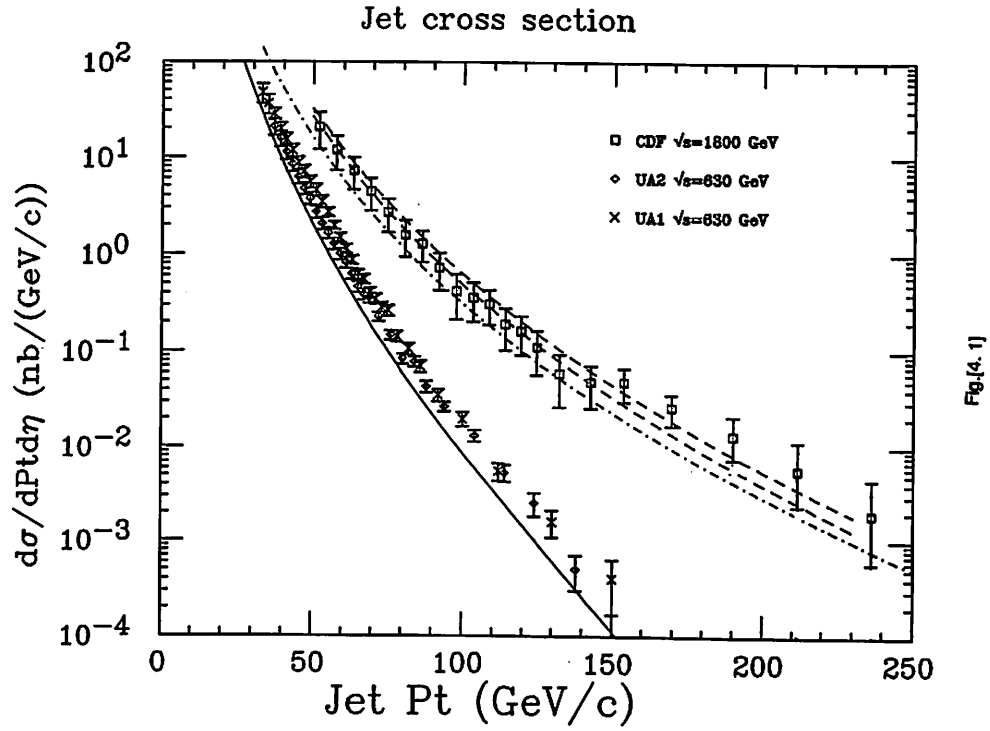

Fig.[4. 1]

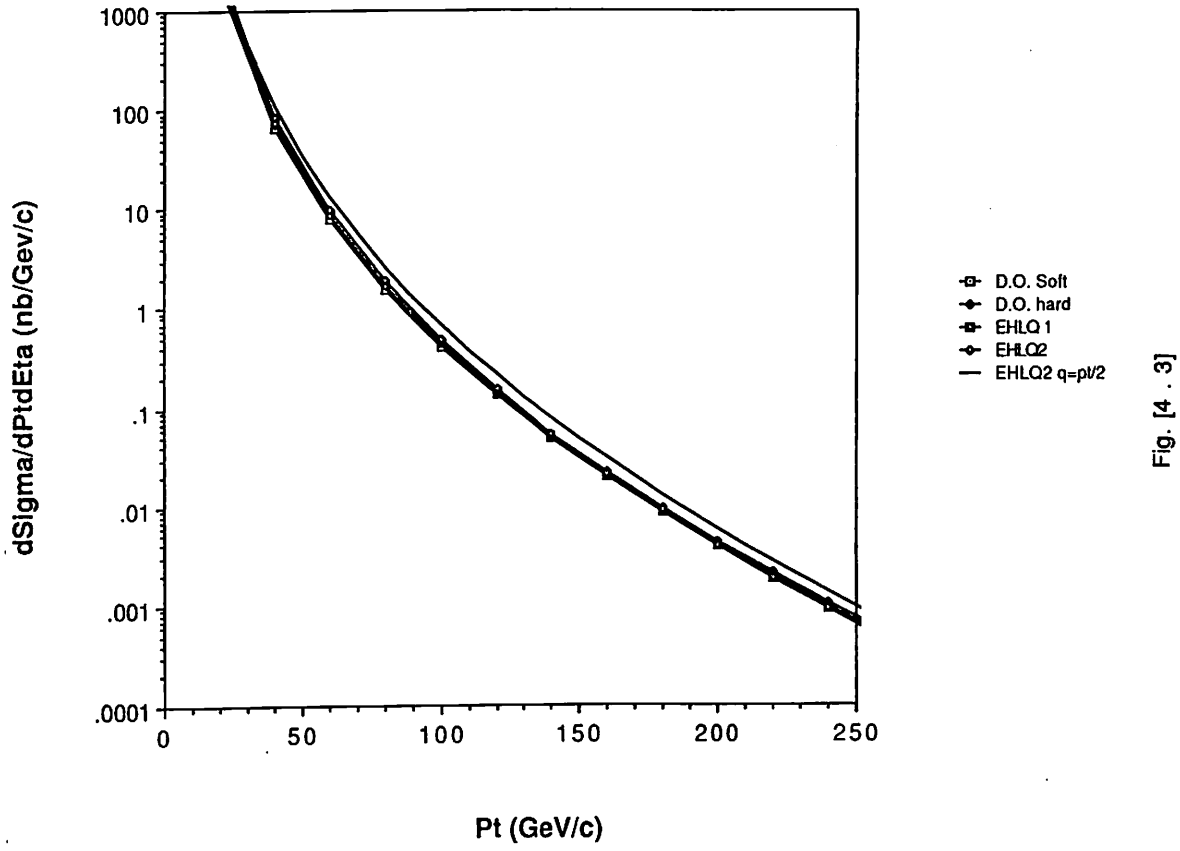

Fig. [4 . 3]

Observed jet cross section under various trigger conditions.

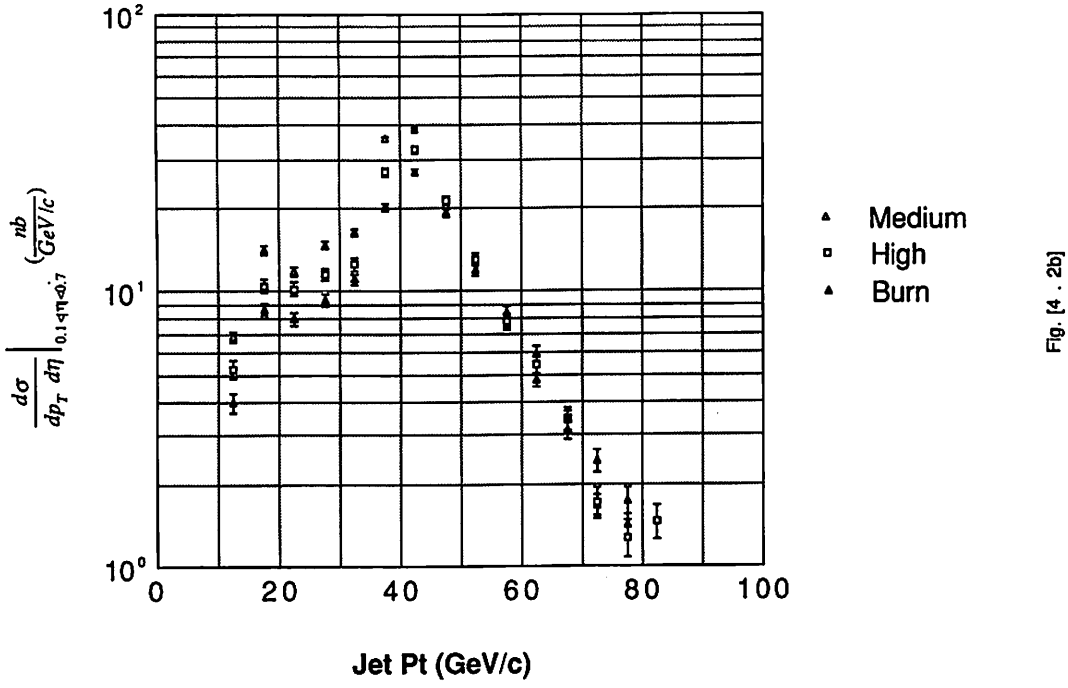

Fig. [4 . 2b]

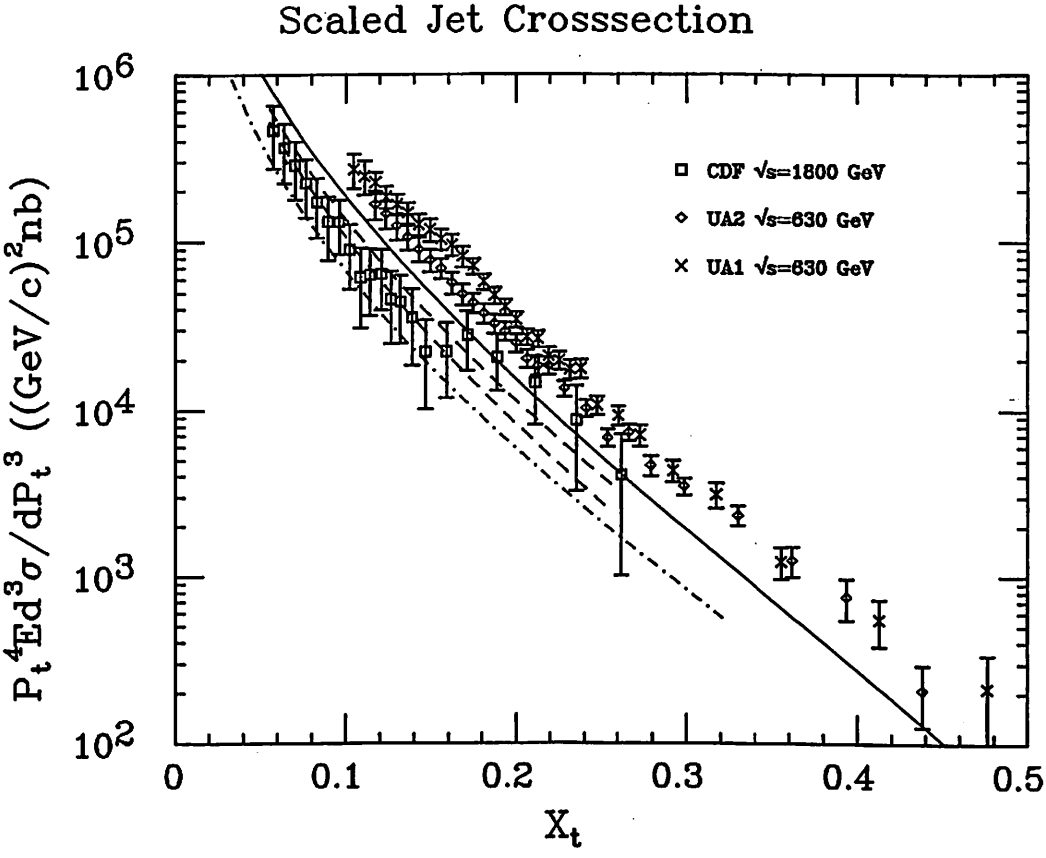
Scaled Jet Crosssection
CDF √s=1800 GeV
UA2 √s=630 GeV
UA1 √s=630 GeV
$P_t^4 E d^3\sigma/dP_t^3$ ((GeV/c)^{2}nb)
X_t
10^6
10^5
10^4
10^3
10^2
0
0.1
0.2
0.3
0.4
0.5

Fig. [4.4]